



저작자표시-비영리-변경금지 2.0 대한민국

이용자는 아래의 조건을 따르는 경우에 한하여 자유롭게

- 이 저작물을 복제, 배포, 전송, 전시, 공연 및 방송할 수 있습니다.

다음과 같은 조건을 따라야 합니다:



저작자표시. 귀하는 원저작자를 표시하여야 합니다.



비영리. 귀하는 이 저작물을 영리 목적으로 이용할 수 없습니다.



변경금지. 귀하는 이 저작물을 개작, 변형 또는 가공할 수 없습니다.

- 귀하는, 이 저작물의 재이용이나 배포의 경우, 이 저작물에 적용된 이용허락조건을 명확하게 나타내어야 합니다.
- 저작권자로부터 별도의 허가를 받으면 이러한 조건들은 적용되지 않습니다.

저작권법에 따른 이용자의 권리는 위의 내용에 의하여 영향을 받지 않습니다.

이것은 [이용허락규약\(Legal Code\)](#)을 이해하기 쉽게 요약한 것입니다.

[Disclaimer](#)

공학박사 학위논문

**An Autonomous Power Management
Strategy for Inverter-Based Islanded
Microgrids Considering Load-Voltage
Dependence**

부하-전압 의존성을 고려한 인버터 기반 독립형
마이크로그리드의 자율적 전력 관리에 관한 연구

2019년 8월

서울대학교 대학원

전기·컴퓨터공학부

문 현 진

An Autonomous Power Management Strategy in Inverter-Based Islanded Microgrids Considering Load-Voltage Dependence

지도교수 문 승 일

이 논문을 공학박사 학위논문으로 제출함
2019년 08월

서울대학교 대학원
전기·컴퓨터공학부
문 현 진

문현진의 공학박사 학위논문을 인준함
2019년 06월

위 원 장 _____ (인)

부위원장 _____ (인)

위 원 _____ (인)

위 원 _____ (인)

위 원 _____ (인)

Abstract

An Autonomous Power Management Strategy in Inverter-Based Islanded Microgrids Considering Load-Voltage Dependence

Hyeon-Jin Moon

School of Electrical Engineering and Computer Science

The Graduate School

Seoul National University

Islanded microgrids (MGs) can improve the system reliability and stability by utilizing various controllable resources such as distributed energy resources (DERs), controllable loads, and other units in the MG system. These effects can be achieved by supplementing intermittent power output of renewable energy sources (RESs) and helping power supply from the DERs in the system. MGs are a self-contained integrated platform and have been introduced for power supply not only to conventional distribution system, but also small power systems including electric shipboards, aircrafts, and remote areas such as the oceanic islands, rural areas, and military bases.

In addition, inverter-interfaced DERs (IDERs), such as energy storage systems (ESSs), which are capable of output control freely and rapidly, have received considerable attention recently because they can respond quickly to dynamic changes in the system. In particular, many researches and demonstration projects for inverter-based islanded MGs, in which a IDER functions as a master and operates to determine voltage and frequency, have been actively under way in around the world: USA; Europe; Asia; and other continents. The operation strategies for IDERs in MGs can be divided into two types: single-master operation (SMO) and multi-master

operation (MMO). In a SMO scheme, one master IDER acts as a voltage source inverter (VSI) and regulates the voltage and frequency. In a MMO scheme, multiple IDERs act as master units. Locally available information such as frequency and bus voltage is used for both SMO and MMO, minimizing the communication problem of centralized control scheme. This approach enables inverter-based islanded MGs can operate autonomously, and help to improve reliability and reduce construction cost of an independent MG.

This dissertation presents a new autonomous power management strategy for inverter-based islanded MGs using the load-voltage dependence. The system frequency set by the master IDER is also used as a global signal. the frequency can be measured by other DERs and controllable equipment without communication links. The proposed methods aim to improve the system stability and reliability by securing primary reserve additionally for the MGs under both SMO and MMO structures. To this end, the autonomous power management strategy is proposed. The proposed strategy can be easily compatible with existing control methods by introducing a controller with simple structure.

For the SMO scheme, a single master IDER is controlled to take charge of both the frequency and voltage generation of the power system and the real-time power supply and demand balance through constant-voltage constant-frequency (CVCF) operation. This control scheme can be suitable when the dynamic response of IDER is fast and the capacity occupies a large part of the entire system. However, if the power supply and/or demand of the MG varies greatly due to serious event such as the generator trip, it can be difficult to cope with the only one master unit.

To solve this problem, this dissertation proposes a voltage-frequency proportional controller (VFPC). Proposed control scheme keeps the frequency and voltage of the system constant under normal conditions by CVCF. On contrast, it detects the voltage drop at the output bus and lowers the system frequency by VFPC. Other DERs then can be induced by $\omega-P$ droop control to provide additional primary reserve, which can alleviate the power shortage and the operational burden of the

single-master unit.

In the MMO architecture, $P-\omega$ and $Q-V$ droop control methods have been widely used to coordinate multiple master IDERs and other controllable resources. In recent years, conservation voltage reduction (CVR), a well-known concept and mature technique that has been used for a long time in power systems, is applied to MGs in order to improve the reliability of the system with a virtual reserve from loads.

In this dissertation, a new strategy for Autonomous CVR (ACVR), incorporated in the current-based droop control of IDER is proposed to improve the operational reliability and stability of an inverter-based islanded MG. For the proposed ACVR, an I_{dq} controller is developed as an outer feedback controller of each IDER, consisting of I_d-V controllers for the ACVR and $I_d-\omega$ and I_q-V controllers for the power sharing.

The proposed two strategies for active power management in SMO and MMO architecture, respectively, are verified by simulations in a MATLAB/SIMULINK environment for different test systems. In the case of the proposed strategy in the SMO structure, a comprehensive MG test model based on the actual grid information provided by KEPCO was used for case studies and demonstrated the effectiveness of the proposed method in improving primary active power control of the MG. On the other hand, in the MMO structure, a three-bus system with three IDERs was used for small-signal analysis and case studies. Small-signal analysis is conducted to verify the performance of the proposed ACVR for variations in the $I_d-\omega$ and I_q-V droop gains. Case studies are also carried out to demonstrate that the ACVR effectively mitigates an increase in the load demand, improving the operational reliability, under various load conditions determined by power factors and load compositions.

Keywords : Autonomous power management, Conservation voltage reduction, Distributed energy resources, Droop control, Energy storage system, Frequency control, Islanded microgrids, Power system reliability, Small-signal analysis

Student Number : 2012-20766

Contents

Abstract	i
Contents	iv
List of Tables	vi
List of Figures	vii
Chapter 1. Introduction	1
1.1 Motivations and purposes	1
1.2 Highlights and contributions.....	5
1.3 Dissertation organization	8
Chapter 2. Inverter-based MG and Load-Voltage Dependence	10
2.1 Architectures and control of inverter-based microgrids	10
2.1.1 MG concepts and structures.....	10
2.1.2 MG control and architectures	13
2.1.3 Control of distributed energy resources.....	17
2.3 Load-voltage dependence in power systems	29
2.2.1 Basic load modeling	29
2.2.2 Conservation voltage reduction	35
Chapter 3. Autonomous Power Management Strategy for Single-Master Operation	41
3.1 System description	44
3.1.1 Grid-forming BESS as a single master unit.....	44
3.1.2 Diesel generator as a slave unit	45
3.1.3 Active power balance equation in an isolated MG with CVCF control	47
3.2 Proposed VFPC for Autonomous power management	49
3.2.1 Frequency control of BESS with VFPC	50
3.2.2 Proposed autonomous power management.....	51

Chapter 4. Autonomous Power Management Strategy for Multi-Master Operation	54
4.1 Description of MG test bed system with multi-master approach	56
4.1.1 MG forming of IDERs by multi master units	56
4.2 Proposed frequency-based ACVR with current-based droop controller.....	59
4.2.1 Proposed I_{dq} controller.....	59
4.2.2 ΔV_{ACVR} with respect to k_{ACVR} coefficients and n_{Id}	62
4.3 Comparative small-signal stability analysis for proposed I_{dq} controller.....	59
4.3.1 Root loci of eigenvalues	68
4.3.2 Eigenvalue sensitivity.....	69
Chapter 5. Case Studies and Simulation Results.....	73
5.1 Case studies for single-master operation	74
5.1.1 Simulation model of case studies for single master operation	75
5.1.2 Simulation results for single-master operation	78
5.2 Case studies for multi-master operation	90
5.2.1 Performance validation of the proposed ACVR strategy.....	91
5.2.2 Effects of load power factors on the proposed ACVR.....	95
5.2.3 Effects of load compositions on the proposed ACVR	97
5.2.4 Performance validation of the proposed ACVR strategy for different n_{Id}	97
Chapter 6. Conclusions and Future Extensions.....	102
6.1 Conclusions	102
6.2 Future extensions.....	105
Bibliographies	106
Appendix A. Small-Signal State-Space Model of Inverter-Based Islanded Micrgrid.....	106

초록 135

List of Tables

Table 2.1. ZIP Model parameters of electrical appliances [56].	31
Table 2.2. Comparisons of two approaches for load modeling [54].	34
Table 2.3. National steady state voltage regulation standards	37
Table 2.4. Summary of CVR effect	39
Table 4.1. Study system parameter for MG test bed.	67
Table 5.1. Parameters used for the simulation model of the isolated MG on Geocha Island.	76
Table 5.2. Parameters of controller for diesel generator in Geocha Island.	76
Table 5.3. Parameters diesel generator in Geocha Island.	77
Table 5.4. Comparisons between the simulation results acquired for different load demand and compositions at $t = 12$ s.	85
Table 5.5. Load impedances and line parameters in the MG test bed.	91
Table 5.6. Performance comparisons between the proposed ACVR and conventional droop control strategies.	94
Table 5.7. Performance comparisons for different power factors of the variable load.	97
Table 5.8. Performance comparisons for different voltage exponents of the variable load.	99

List of Figures

Figure 2.1	Microgrid system configuration.....	10
Figure 2.2	Inverter-based MG configuration.	12
Figure 2.3	General MG control architecture; hierarchical scheme [45].....	13
Figure 2.4	Centralized control architecture for MG operation [15]....	15
Figure 2.5	$P-\omega$ and $Q-V$ droop characteristics for autonomous control [15].....	16
Figure 2.6	Classification of DERs [46].....	17
Figure 2.7	Grid-forming converter type with VSI and DER.	19
Figure 2.8	Basic control structure in a three-phase grid-forming voltage source inverter generating a sinusoidal voltage with ω^* and V^*	20
Figure 2.9	Grid-support grid-forming inverter type with VSI and DER.	21
Figure 2.10	Basic control structure in a three-phase grid-support grid- forming voltage source inverter generating a sinusoidal voltage with ω^* and V^* , calculated by the power controller with droop control.....	21
Figure 2.11	Control block diagram of voltage controller in grid- forming unit.	22
Figure 2.12	Control block diagram of current controller.	23
Figure 2.13	Grid-feeding converter type with VSI and DER.....	24
Figure 2.14	Grid-support grid-feeding inverter type with VSI and DER.	25

Figure 2.15	Basic control structure in a three-phase grid-support grid-feeding current source inverter.	25
Figure 2.16	General control scheme for SMO.	26
Figure 2.17	General control scheme for MMO.	28
Figure 2.18	Component-based modeling approach [54].	33
Figure 2.19	Measurement-based modeling approach.....	34
Figure 2.20	Two ways to perform CVR: (left) Peak demand reduction and (right) 24-hr energy reduction [58]	36
Figure 2.21	ANSI standard C84.1 (a): Not available at light loads, (b): Not available at 120-600 V systems [61].....	37
Figure 3.1	A schematic diagram of the grid-forming BESS and its device-level controllers.....	44
Figure 3.2	A schematic diagram for the active power controller and system dynamics of the diesel generator.....	45
Figure 3.3	A schematic diagram for the reactive power controller and exciter block of the diesel generator.	46
Figure 3.4	Flow chart of the proposed VFPC for the autonomous power management at a primary control level.....	49
Figure 3.5	A schematic diagram of the V - f proportional controller for the grid-forming BESS acting as single master unit.....	50
Figure 3.6	Comparison between (a) the proposed control strategy (i.e., VFPC) of the grid-forming BESS) and (b) the conventional control strategy (i.e., droop controller) of the diesel generators.....	51
Figure 3.7	Sequential operations of the VFPC.	53
Figure. 4.1	A schematic diagram of a VSI-interfaced DER and its local controller including the outer and inner feedback loops.	

	The RLC filter and grid coupling impedance are also presented	57
Figure 4.2	A block diagram of the proposed I_{dq} controller for the frequency-based ACVR incorporated in the current-based droop control.....	59
Figure 4.3	Three eigenvalue clusters for the proposed ACVR, current-based droop control, and conventional droop control strategies	61
Figure 4.4	Mechanism of the proposed I_{dq} controller	61
Figure 4.5	Comparison of system voltage profiles for original and ACVR	64
Figure 4.6	Schematic diagram for voltage reduction at n-th bus.....	65
Figure 4.7	Three eigenvalue clusters for the proposed ACVR, current-based droop control, and conventional droop control strategies	68
Figure 4.8	Close-up plots in Fig. 4.7 for the critical eigenvalues in the rightmost cluster.....	68
Figure 4.9	Locus of eigenvalues as a function of m_{Id} and m_P for 0.2 % to 1 % droop ($2.39 \times 10^{-2} \leq m_{Id} \leq 1.20 \times 10^{-1}$ and $6.28 \times 10^{-5} \leq m_P \leq 3.14 \times 10^{-4}$)	70
Figure 4.10	Locus of eigenvalues as a function of n_{Iq} and n_Q for 1 % to 11 % droop ($2.42 \times 10^{-1} \leq n_{Iq} \leq 2.66$ and $6.35 \times 10^{-1} \leq n_Q \leq 7 \times 10^{-3}$).....	71
Figure 4.11	Locus of eigenvalues as a function of ω_c (90%, 36%, and 16% increases from the original value, respectively. About 1.25 rad/s per step.).....	72

Figure 5.1	Schematic diagram of Geocha Island MG.	74
Figure 5.2	Simulation model of Geocha Island MG using MATLAB/Simulink software environment.	75
Figure 5.3	Profiles of the active power outputs of the BESS, WT, PV, and diesel generator.	78
Figure 5.4	The reactive power profiles of the BESS, WT, PV, and diesel generator.	78
Figure 5.5	Profiles of the input voltages of the BESS, WT, PV, and diesel generator.	79
Figure 5.6	Comparison of the grid frequency profiles in the Geocha	79
Figure 5.7	Comparison of the reference frequency profiles of the BESS in the Geocha MG.	79
Figure 5.8	Comparison of the total load demand profiles in the Geocha MG.	80
Figure 5.9	Active power profiles of the BESS and diesel generator in Cases 2 and 3.	84
Figure 5.10	Profiles of the input voltages of the BESS and diesel generator in Cases 2 and 3.	84
Figure 5.11	Comparisons of the frequency profiles at the main transformer and BESS in Cases 2 and 3.	84
Figure 5.12	Comparisons of the total load demand profiles in the Geocha MG.	85
Figure 5.13	Profiles of the active power outputs of the BESS and diesel generator in Cases 2* and 4.	86
Figure 5.14	Profiles of the input voltages of the BESS and diesel generator in Cases 2* and 4.	87
Figure 5.15	Comparisons of the frequency profiles at the main	

	transformer and BESS in Cases 2* and 4.	87
Figure 5.16	Comparisons of the total load demand profiles in Cases 2* and 4.....	87
Figure 5.17	Comparison of simulation results for Cases 1 (Navy) and 2 (Red) at $t = 12$ s.....	88
Figure 5.18	An islanded MG including IDERs and voltage-dependent loads.	90
Figure 5.19	(a) Active and (b) reactive power outputs of the IDERs for $n_{ld} = 5\%$	92
Figure 5.20	(a) Frequency and (b) voltage profiles at the output nodes of the IDER.....	92
Figure 5.21	Comparison of load reduction between conventional and proposed methods.	94
Figure 5.22	Comparison of control performance between the conventional and proposed methods.....	95
Figure 5.23	Total (a) active and (b) reactive load demands for different pfs	96
Figure 5.24	Bus voltage profiles for different pfs	96
Figure 5.25	Total (a) active and (b) reactive load demands for different n_p in (4.1).	98
Figure 5.26	Bus voltage profiles for different values of n_p in (4.1) ...	99
Figure 5.27	(a) Active and (b) reactive power outputs of the IDERs for different m_{ld} and n_{ld}	100
Figure 5.28	(a) Frequency and (b) voltage profiles at the output nodes of the IDERs for different m_{ld} and n_{ld}	100

Chapter 1. Introduction

1.1 Motivations and purposes

Motivation for studying inverter-based islanded microgrids

The penetration of renewable energy sources (RESs) such as photovoltaics (PVs) and wind turbines (WTs) is steadily increasing due to enhanced price competitiveness and the requirement of sustainable energy mix. However, intermittent power outputs of RESs are detrimental to frequency and voltage stability particularly in a small power system: e.g., a microgrid (MG) possessing a low moment and/or lack of inertia [1]–[3].

MGs, as building blocks of smart grid and self-contained local entities, are an overarching paradigm of integrating distributed energy resources (DERs) such as distributed generators (DGs), energy storage systems (ESSs), and demand response (DR) resources. This integrated platform can be equipped with various functions for local power and energy management [3] under both grid-connected and islanded operating modes. It has been of special interest in developing MG-level and device-level controllers to improve system reliability, which is the ability to balance between power generation and load demand, so that frequency and voltages can be maintained within acceptable ranges when MGs operate in an islanded mode [4]. That is, the voltage and frequency should be regulated within acceptable ranges and the power supply-demand balance should be always maintained by itself using internal controllable devices.

Meanwhile, electric utilities have technical difficulties in connecting remote MGs on small oceanic islands to a bulk power grid on the mainland. It is also cost-ineffective and, therefore, electric power supply in these remote MGs relies primarily on diesel generators located in the area. Power outputs from diesel generators can be adjusted in real-time to achieve power balance and hence maintain frequency and

voltage stability [5]. However, heavy reliance on conventional diesel generators can lead to the following problems:

- Degradation of power quality and reliability due to the low-inertia moment and constant-speed control scheme of diesel engines [2], [6].
- High generation cost and volatility due to fuel import and transportation [7], [8].
- Environmental issues such as carbon emission and air/noise pollution [7]–[10].

In recent years, power converters have been widely used as the interfaces for DERs to be connected with an islanded MG. Inverter-interfaced DERs (IDERS) have faster time responses than conventional generators. Therefore, IDERS have recently received significant attention to improve, for example, the real-time frequency and voltage stability, power quality, and fault-current coordination in islanded MGs [4], [11], and [12].

Moreover, IDERS are capable of operating as grid-forming units, similar to synchronous generators, determining the frequency and bus voltages in an islanded MG. An MG with the grid-forming IDERS is referred to as an inverter-based MG [13]. Because of the various advantages of IDER, inverter-based MGs are of increasing interest in industry leader, universities and researchers, with many test beds around the world including South Korea: the consortium for electric reliability technology solutions (CERTS), national renewable energy laboratory (NREL), Hawaii natural energy institute (HNEI) in the United States; the institute for systems and computer engineering, technology and science (INESC TEC), Catalonia institute for energy research (IREC) in Europe; the new energy and industrial technology development organization (NEDO), Korea electric power research institute (KEPRI) in Asia. In addition, some demonstration projects for inverter-based MGs are also underway on other continents such as Chico Mendes, Brazil and Xcalak, Mexico.

Specific topics of this dissertation

Stable and reliable operation is more important issue than economical operation in an islanded MG where there is no connection and power supply from the main grid. Many studies have been conducted on the real-time control of DERs to improve the operational stability and reliability of islanded MGs. For example, in [14]–[17], centralized control schemes have been implemented in an MG central controller or an MG energy management system (EMS) for cooperation of a DER with other DERs, controllable loads, and voltage-regulating devices such as capacitor banks. The centralized schemes have advantages of determining global or near-global optimal operations of MGs, based on full observation of the operating conditions of DERs. This paradoxically implies the risk of the centralized strategy to require a large amount of information from the devices and consequently large computing resources, preventing the practical implementation, given the variabilities in the type and ownership of the MG components. Moreover, the strategy heavily relies on communications links to transfer signals between the central controller and the individual components. Hence, it is difficult to implement the centralized schemes in practice [12].

To overcome the difficulty, fully decentralized control, so called autonomous control schemes have been discussed in several studies where the coordination among individual DERs is achieved using the device-level controllers based on local measurements. For example, the traditional single-master slave control method, so called single-master operation (SMO), consists of one master grid-forming unit with the dispatchable DER and applied for operation of inverter-based MG in a decentralized manner. A constant-voltage constant-frequency (CVCF) control scheme has been adopted for single master unit in SMO. The BESS is mainly used for single-master unit to maintain frequency and voltages at their rated levels and consequently achieve real-time power balance in an islanded MG. In [18]–[27], the control scheme was practically applied to isolated MGs in remote islands (including several islands in South Korea) mainly due to simple implementation and low

fluctuations in grid frequency and voltages. However, the scheme requires large capacities of the master DER and inverters to achieve the real-time power balance under the condition on large variations in load demand and RES power outputs. Moreover, if a problem occurs in the master unit, it is a serious threat to the entire system, which adversely affects the reliability of the system.

To solve this problem, multi-master operation (MMO) scheme has been introduced, mainly with droop control scheme. The $P-\omega$ and $Q-V$ droop control schemes have been widely adopted [28]–[30], so that the total power generation is shared among the DERs for the real-time frequency and voltage regulations. The modifications to the droop control scheme also have been discussed in [31]–[34], for example, using the virtual impedance and $V-I$ droop controllers to improve the $P-Q$ decoupling and power sharing accuracy. However, MMO implementation can be difficult depending on system conditions such as the number of dispatchable IDER.

Therefore, it is necessary to study two operations. In this dissertation, SMO and MMO are considered for different test system. autonomous power management is focused on this dissertation.

1.2 Highlights and contributions

This dissertation proposes a new autonomous power management strategy for in inverter-based islanded MGs considering load-voltage dependence. Proposed schemes aim for stable and reliable operation in two modes, the SMO and the MMO, respectively. The highlights and main contributions of this dissertation are as follows:

Reducing Power shortage problem of conventional CVCF control for SMO

The CVCF control by single-master unit with grid-forming control is advantageous in that the frequency and voltage of the system can be kept constant under normal operating conditions, but there is a disadvantage that the burden of system dynamics and instantaneous power balance of the islanded MG is mostly concentrated on only single-master unit. On the other hand, the droop control of single-master unit enables the slave units share the operation burden of the single-master unit for SMO. However, droop control has inherent limitations that cause continuous fluctuations in system frequency and bus voltage during the process of real-time power balancing [35].

Based on these observations, this dissertation proposes a new autonomous scheme integrated with CVCF, droop control, and frequency-bus-signaling based on a SMO mainly to improve power sharing and real-time power balancing under the serious conditions where disturbances occur in an islanded MG. In coordination with the CVCF controller, the proposed scheme enables the BESS, acting as a single-master unit, to control the system frequency in response to the change in AC voltages, given that unexpected voltage changes by load voltage dependence at the grid-forming converter bus indicate the instantaneous active power imbalance in the MG [36]. The proposed decentralised scheme enables autonomous power management in the MG with SMO via the wireless coordination of the single-master BESS unit with other slave DERs (particularly for the condition of lack of power generation), minimizing the frequency and voltage deviations.

New frequency-based conservation voltage reduction strategy incorporated into the current-based droop control for MMO

The P - ω and Q - V droop control scheme is a conventional control method to coordinate multi-master units and other control units. In addition, conservation voltage reduction (CVR) has been recently revisited to reduce energy and peak demands by lowering MG voltages within acceptable ranges, mitigating the lack of power and energy supplies in islanded MGs [37]–[40].

This dissertation proposes a new CVR strategy for multi-master DERs that is incorporated in the current-based droop controller for active and reactive power sharing in the inverter-based MG. The proposed CVR strategy requires only the local measurements of the IDER current outputs, which allows autonomous operation of inverter-based islanded MGs. Specifically, for the proposed strategy, an I_{dq} controller is developed as an outer feedback controller of each IDER; therefore, it can be readily integrated into an existing IDER. The I_{dq} controller consists of two modules: The I_d - V droop for CVR and the I_d - ω and I_q - V droop for power sharing.

The I_d - V controllers adjust the output voltages of the IDERs in proportion to the MG frequency variation (or, equivalently, the load demand variation), mainly determined by the I_d - ω droop coefficients. Since the frequency is a global signal throughout the MG, this enables the individual IDERs to reduce their output voltages by the same amount in an autonomous manner: i.e., without relying on communications among the IDERs. Moreover, the reductions of the bus voltages become large under heavy loading conditions. Considering the I_d - V controllers, the I_q - V controllers induce additional variations in the output voltages of the IDERs for the reactive power sharing, depending on the I_q - V droop coefficients; the resulting output voltages need to be maintained within acceptable ranges for time-varying load demand. Note that the I_d - ω and I_q - V droop controllers can replace the conventional P - ω and Q - V droop controllers, eliminating the time delays for the measurements of P and Q . Therefore, the current-based controllers enable the IDERs to respond faster than the conventional ones, improving their transient responses

Simple and easily implementable structure of proposed controllers

The proposed controllers, voltage-frequency proportional controller (VFPC) and I_{dq} controllers, for SMO and MMO, respectively, are all in a linear combination of local variable, which can be measured by local measurements. These are applied to the outer feed-back loop of the local controller of a master IDER. Hence, the structure is very simple and easily implementable to conventional controllers. Proposed VFPC for SMO can be easily applied to the existing CVCF controller of the grid-forming BESS and enables the coordinated control with other DERs that operate with conventional $f-P$ droop controllers, which ensures the normal operations of inner control loops.

The proposed I_{dq} controller for MMO is also easy to replace existing droop controllers of the master IDERs, consisting of I_d-V controllers for the ACVR to obtain system damping and $I_d-\omega$ and I_q-V controllers for the power sharing with faster dynamic responses.

Enhanced Reliability of inverter-based islanded MGs

In islanded MG, it is one of the most important goals to maintain the real-time power balance at all times by utilizing only the resources of the system itself. Centralized methods are vulnerable to a single point of failure (i.e., a part of a system that prevents the normal operation of the entire system if it fails). This degrades the reliability of islanded MGs [41], [42]. As alternative options, proposed power management schemes are controlled in an autonomous manner. The proposed autonomous power management scheme for SMO utilizes the bus voltage and system frequency for coordinated control between master BESS and slave diesel generator units, allowing the system to utilize more primary reserves. The proposed scheme for MMO can provide a virtual reserve from demand side by frequency-based CVR for inverter-based islanded MGs, improving system reliability and transient response by using current-based controller and requiring no communication infrastructures.

1.3 Dissertation organization

The rest of the dissertation is organized as follows:

Chapter 1 presents the motivations, purposes, highlights, and contributions of this dissertation. And the last part of this chapter describes the configuration of this dissertation.

Chapter 2 explains the basic concept and structure of inverter-based MGs and control architecture and DERs for the control of inverter-based MGs. The load voltage dependence in power systems is summarized with two categories; basic load modeling and CVR concept.

Chapter 3 describes the autonomous power management strategy for SMO by using CVCF of the one master unit, droop control of slave unit, and frequency-bus-signaling to communicate between master and slaves. To reduce the burden on the primary control of one single-master BESS, the VFPC is introduced in coordination with conventional CVCF controller of single master-unit and f - P droop controller of slave units.

Chapter 4 describes a new autonomous CVR strategy based on system frequency generated by multi master units to improve system stability and reliability. A virtual reserve is can be obtained from demand side by proposed frequency-based ACVR scheme. A proposed current-based controller can replace successfully conventional droop controller and allow master IDER react more fast by shortening measurement delay and decoupling bus voltage. Moreover, small-signal state-space modeling is derived and small-signal analysis is carried out to validate the enhanced stability and parameter robustness for droop gains related to power sharing.

Chapter 5 presents the simulation results for various case studies in SMO and MMO with different systems. The effectiveness of the proposed methods for both SMO and MMO schemes are verified.

Chapter 6 concludes this dissertation and discusses future extensions.

In addition, complete small-signal state-space model of general inverter-based

islanded MGs with proposed scheme is derived and described in Appendix A.

Chapter 2. Inverter-based MG and Load-Voltage Dependence

2.1 Architectures and Control of Inverter-based MGs

2.1.1 MG Concepts and structure

Concept and features of general MG

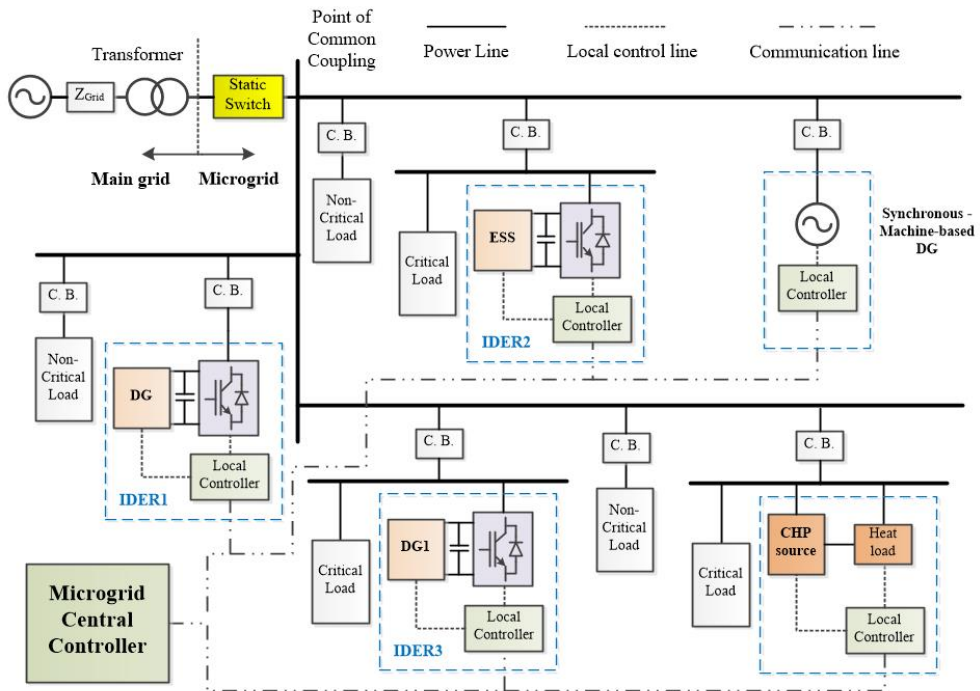


Fig. 2.1. MG system configuration.

A MG, which is first introduced concept in [43], [44], refers to a self-contained local entities including distribution systems with DG and loads [3]. Fig. 2.1 shows the general MG system configuration.

The definition of MG from the EU research projects is shown below:

MGs comprise LV distribution system with DER (micro-turbines, fuel cells, PV, etc.) together with storage devices (flywheels, energy capacitors and batteries) and flexible loads. Such systems can be operated in a non-autonomous way using a MG central controller (MGCC), if interconnected to the grid, or in an autonomous way using the local controllers, if disconnected from the main grid. The operation of micro-sources in the network can provide distinct benefits to the overall system performance if managed and coordinated efficiently [15], [16].

From the definition, microgrids have the following features [3]:

1. A MG is an integrated platform for DGs, ESSs, and demand side resources (controllable loads) located in a local distribution system.
2. A MG should be operated both grid-connected and islanded operation.
3. A MG should be capable of management and coordination of available resources.

In the MG concept, the capability of local power supply is a characteristic element distinguishing between MG and other concept such as virtual power plants. In addition, the static switch plays a role for operation mode changing of the MG and synchronization between main grid. When the switch is closed, the MG is connected with main grid. In grid-connected mode, the voltage and frequency are determined from main grid. On the other hand, in islanded mode, when the static switch is open by intentional or unintentional reason, the MG should be capable of achieving the system power balance between supply and demand. In particular, it has been of special interest in developing MG- and device-level controllers to maintain the instantaneous balance between power generation and load demand, so that the frequency and voltage can be maintained within acceptable ranges. For long-term and sustainable islanded operation, a MG has to satisfy high requirements on power supply capability from DG and flexibility by utilizing controllable devices such as ESS.

Concept of inverter-based MG

Meanwhile, power converters have been widely used as the interfaces for DERs to be connected with an islanded MG. IDERs have faster time responses than conventional synchronous generators. Therefore, IDERs have recently received significant attention to improve, for example, the real-time frequency and voltage regulations, power quality, and fault-current coordination in islanded MGs [4], [11], [12]. Moreover, IDERs are capable of operating as grid-forming units, determining the frequency and bus voltages in an islanded MG: i.e., IDERs can be used as an alternative of conventional synchronous generators. An MG with the grid-forming IDERs is often referred to as an inverter-based MG, which is shown in Fig. 2.2. The corresponding characteristics of inverter-based MGs are near instantaneous and independent control of the frequency and the magnitude of each phase. Hence, the system frequency can be controlled by the grid-forming unit regardless of the system load change.

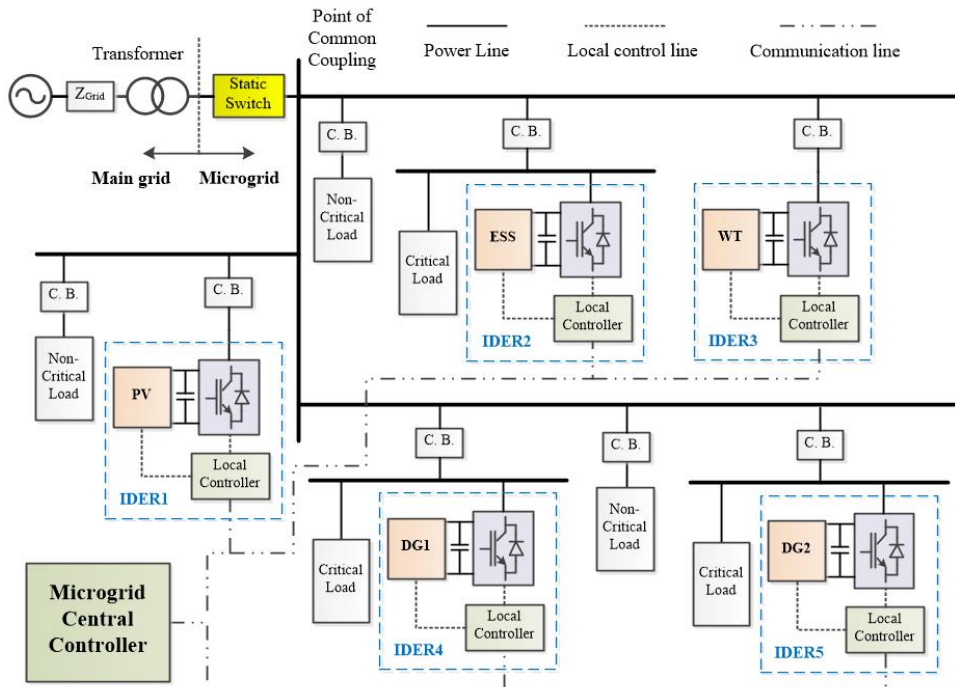


Fig. 2.2. Inverter-based MG configuration.

2.1.2 MG control and architectures

MG control architectures

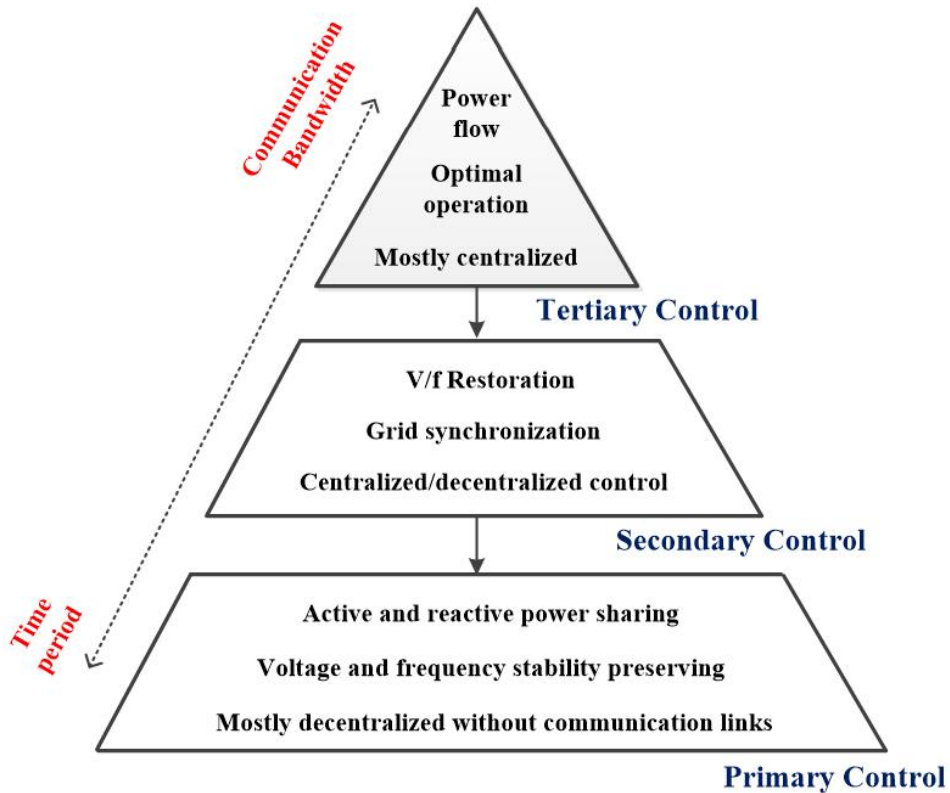


Fig. 2.3. General MG control architecture; hierarchical scheme [45].

The main purpose of the MG operation can be summarized as:

1. Voltage and frequency regulation and active and reactive power sharing
2. MG resynchronization with the main grid for mode-changing
3. Optimizing the MG operation

These roles have different significances and time scales, and information, thus requiring a hierarchical structure for MG operation as shown in Fig. 2.3. Hierarchical control can be interpreted to decompose a complex problem into smaller sub-problems and recombine the solution into a "functional" hierarchy. The higher layer

of the controller is operated with the longer time scale of execution and higher communication band-width to process the data for the calculation than its immediately lower layer. The operation of the individual layers is coordinated and planned by higher layers which do not reject their decision except for abnormal condition.

From the perspective of MG operation, the control system structure is divided into three layers; primary, secondary, and tertiary control. Primary control is the first layer of the hierarchy, and also known as internal control or local control. the main role of a primary control layer is real-time active and reactive power sharing, and consequently preserving the voltage and frequency stability of MG systems. The primary controller operates mainly by using a local controller and measurement signal which can be obtained without communication link. Therefore, primary control based on communication-less approach can offer plug-and-play characteristics to controllable unit in the MG system.

The secondary control layer, also referred to as the EMS, is responsible for the restoration of voltage and frequency. The secondary control is challenging in islanded MGs with high penetration of RESs having intermittency. Hence the secondary control often uses MGCC to perform a control task. The centralized control strategy has the advantages in finding the global or near-global optimal operating point of the MG, based on full observability of the operating states of the units in the MG.

The tertiary control is the highest control layer of MG control. the role of this layer is to set an optimal operating points depending on the gathered information from microgrid elements and system operators. It also responsible for communicating interest and coordinating operation between main grid and MGs. In this dissertation, since the secondary and tertiary control often need for communication infrastructure. the only primary control of inverter-based islanded MG is only considered to focus on autonomous operation. Secondary and tertiary controls will not be discussed further.

Centralized control

The centralized control strategy has advantages in finding the global or near-global optimal operating point of the MG, based on full observability of the operating states of the units in the MG. Fig. 2.4 shows the control architecture of centralized approach. The information with regard to operation is collected and forwarded to MGCC. The information need to be gathered for optimal point is as follow:

1. forecasting of non-dispatchable unit and electrical/thermal load
2. operation constraint with regard to operational limit, security, and reliability
3. Energy price, price forecasting and other system states

Based on the information collected from system operator, individual DER units, and local measurements is used to solve optimization problems set by the MGCC. The output variables of MGCC are mainly reference set-points of the DERs together with command signal for controllable loads and non-dispatchable units. However, this approach paradoxically implies the risk of the centralized strategy to require a large amount of information from the devices and consequently large computing resources, preventing the practical implementation, given the variabilities in the type and ownership of the MG components. Moreover, the strategy heavily relies on communication links to transfer signals between the central controller and the individual components. This adversely affects the reliability of the MG [29].

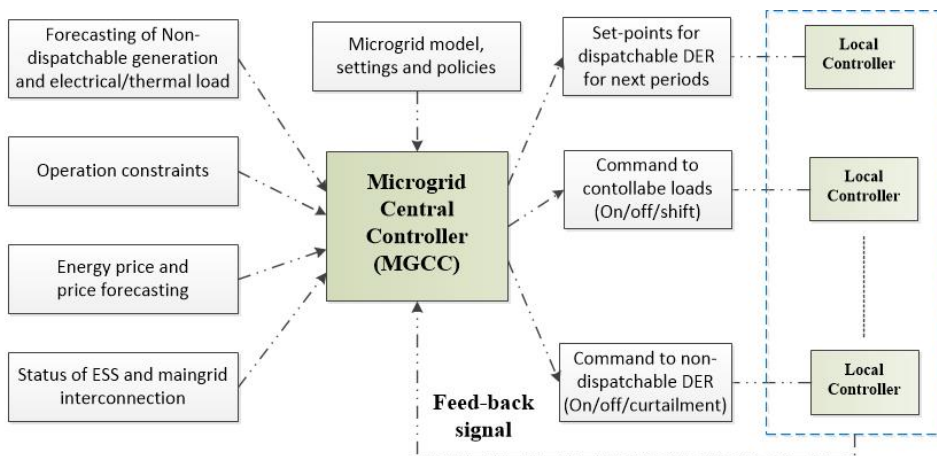


Fig. 2.4. Centralized control architecture for MG operation [15].

Autonomous control

A decentralized control is an alternative option in which the coordinated operations of individual units are achieved without centralized controller. Unlike the centralized control schemes, the fully decentralized schemes, so called autonomous control with only local measurements, allow the MG to operate continuously with the plug-and-play feature [41] (even under the condition of the single-point failure) and hence can improve the operational reliability of the MG.

In particular, the $P-\omega$ and $Q-V$ droop control schemes are commonly adopted, so that the IDERs share the total power output required to regulate the frequency and voltages, respectively, in the inverter-based MG [12]–[16], as in the case of synchronous generators. Fig. 2.5 illustrates a conventional $P-\omega$ and $Q-V$ droop control characteristics. The relationship between $P-\omega$ and $Q-V$ can be expressed as

$$\omega_o = \omega^* - m_p(P_o - P^*) \quad (2.1)$$

$$V_o = V^* - n_q(Q_o - Q^*) \quad (2.2)$$

The droop coefficients m_p and n_q are determined based on active/reactive power rating of each DER and maximum/minimum constraints of system frequency and voltage. The main advantages of droop control are as follows: i) avoid of communications; ii) great flexibility; iii) high reliability. On the other hand, this method has some drawbacks as follows: i) trade-off between voltage regulation and load sharing; ii) influence of system impedance; iii) slow dynamic response.

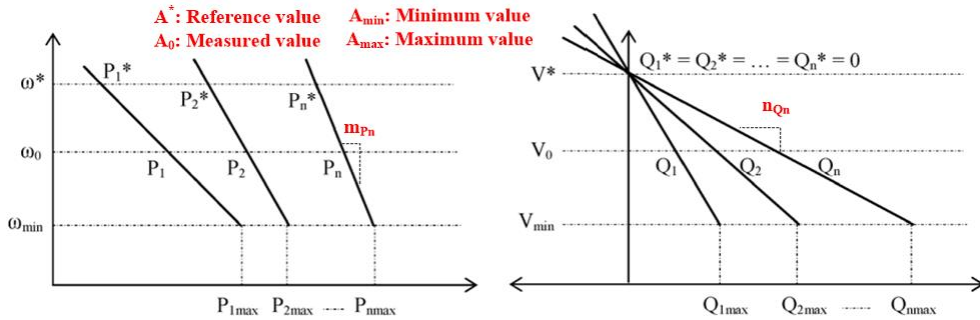


Fig. 2.5. $P-\omega$ and $Q-V$ droop characteristics for autonomous control [15].

2.1.3 Control of distributed energy resources

Concept of distributed energy resources

The concept of DER varies slightly from subject to subject. North American electric reliability corporation (NERC) defines a DER as any resources on the distribution system that produces electricity and is not otherwise included in the formal NERC definition of the bulk electric system. Traditionally, the DERs was referred to small and geographically dispersed generation resources, such as PVs, WTs, micro-turbines, and combined heat and power (CHP) generators. Types of DERs and their classification are shown in Fig. 2.6.

The DERs is installed and operated mainly in distribution systems with voltage levels below 100 kV. Thanks to technological advances and state energy policies in recent years, DER installations and penetration in distribution systems and MGs have increased significantly in some regions of US, EU, and Asia, especially isolated MGs in a remote area.

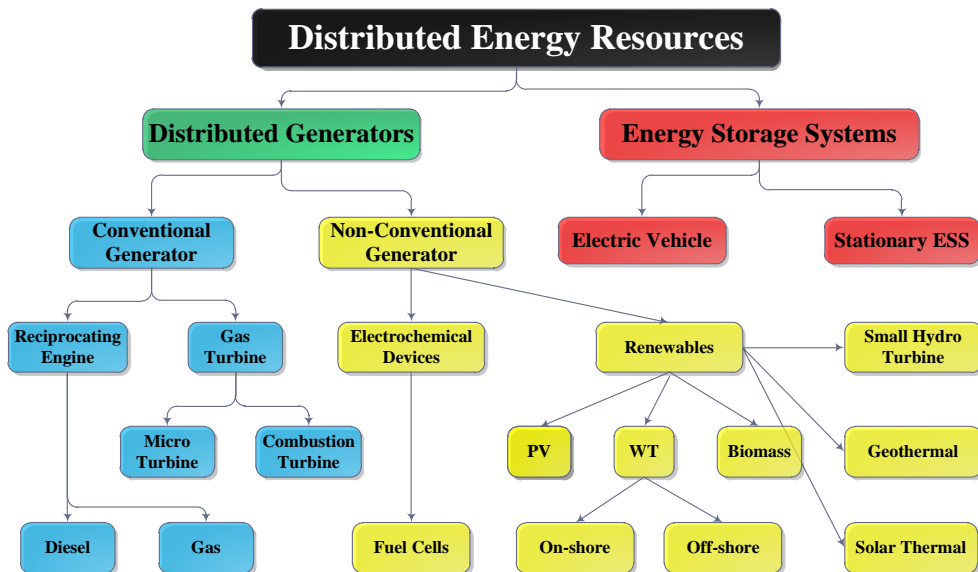


Fig. 2.6. Classification of DERs [46].

Potential of distributed energy resources

In MGs, the DERs are mainly responsible for the power supply and the stability of the MG systems [3]. Therefore, the dynamic characteristics of DERs have a great influence on the dynamic behaviors of MGs. Generally, DERs provide MG systems with greater reliability, the improved power quality, system protection and stability. DERs also have the potential to mitigate overloaded transmission lines, provide greater stability, enhance resilience in the MG. Some of the primary applications for DER include [46]:

- Premium power: improved power quality by reduced frequency variations, voltage transients, surges, dips, or other disruptions
- Back-up power: used in the event of an outage or unintentional islanding, as a back-up to the main grid
- Peak shaving: the use of DER during times when load demand is high
- Low-cost energy: the use of DER as primary power supply that is less expensive to produce locally than it is to purchase from the electric utility
- CHP (cogeneration): increases the efficiency of on-site power generation by using the waste heat for existing thermal process

According to the interface, DERs can be classified into two categories depending on how they are interfaced to the MG systems: 1) IDERs; 2) DERs directly connected to the MGs. Such as PV, wind turbines, fuel cells, batteries, flywheels, and super capacitors are connected to the MG by inverters. While a conventional generator such as double-fed induction generator, small gas combustion turbines, and internal combustion engines is mainly connected directly to the MG without inverters. Since RESs are usually applied as much as possible to build a sustainable and eco-friendly MG system, inverter-interfaced DERs are widely used for the MG. The high penetration of RESs and inverter-interfaced DERs make the operating characteristics of MGs quite different from the conventional bulk power system.

Controller type of IDERs

IDERs can be classified into grid-forming, grid-feeding, and grid-supporting units, depending on the control modes for interfacing DER into the MG. The grid-supporting units can be divided into grid-support grid-forming and grid-support grid-feeding units as a voltage source and current source, respectively. An overview about the control mode and operation feature of inverter in an IDER at converter level with dq -reference frame is described in [47]. This dissertation only considers the control structure with stable DC voltage sources and PI controllers in dq -frame, which is the most common and widely used controller in industrial application today [48].

Unlike conventional synchronous-machine-based systems where the system voltage and frequency are formed by synchronous generators with the inertia, inverter-based MGs require at least one grid-forming unit for frequency and voltage setting of the system. A grid-forming controller operates as an ideal AC voltage source having a series low-output impedance as shown in Fig. 2.7 [47]. Grid-forming unit mainly responsible for setting voltage and frequency with the angular frequency and bus voltage reference signal ω^* and V^* in the islanded MG. A standby UPS is the one of the practical example of a grid-forming power converter. The UPSs are only connected and act as a grid-forming unit when the MG is disconnected from the main grid.

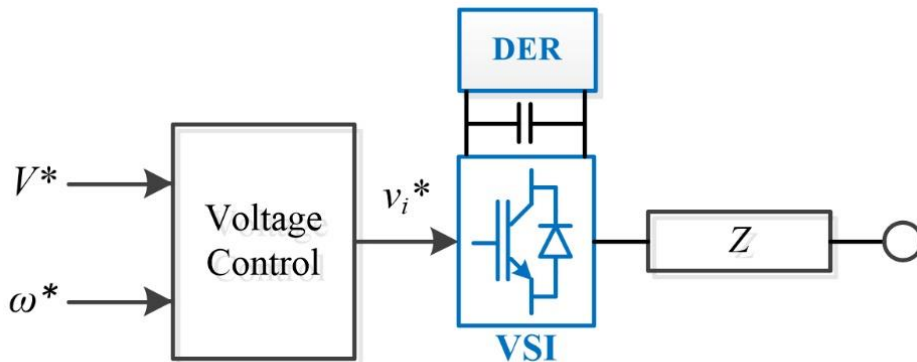


Fig. 2.7. Grid-forming converter type with VSI and DER.

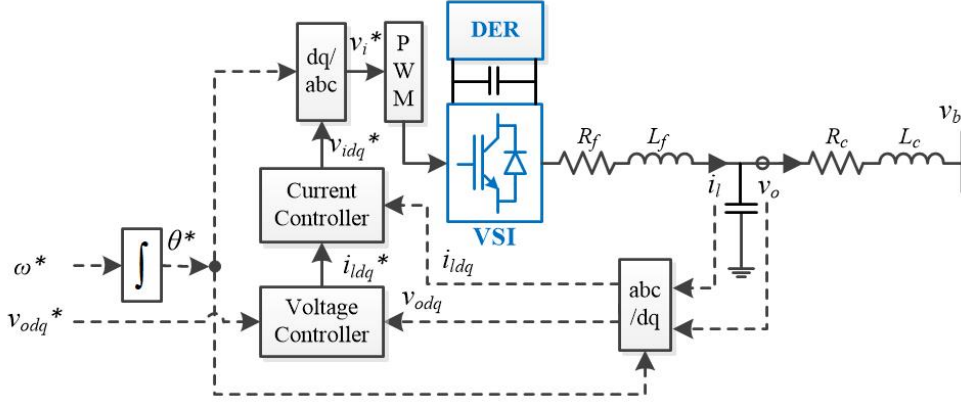


Fig. 2.8. Basic control structure in a three-phase grid-forming voltage source inverter generating a sinusoidal voltage with ω^* and V^* .

Fig. 2.8 shows a basic control structure for a grid-forming voltage source inverter (VSI). The system inputs are dq -axis reference voltage and frequency to be set by the grid-forming unit at the point of common coupling. The inverter controller has nested loop including outer voltage controller and inner current controller, operating on dq -frame. This is because the nested control loop has advantages as: i) there is explicit control of current and transient current can be limited by current controller; ii) the plant is considered as two first-order systems with no disturbance signal; iii) it can lend itself to current sharing between parallel modules.

One example of operating with a grid-forming unit is a CVCF control. This control scheme was adopted for IDERs, especially BESSs, to maintain frequency and voltages at their rated levels and consequently achieve real-time power balance in an islanded MG [49]. The control scheme was practically applied to isolated MGs in remote islands (including several islands in South Korea) mainly due to simple implementation and low fluctuations in grid frequency and voltages. However, this CVCF control scheme requires large capacities of DER and inverter to achieve the real-time power balance under the condition on large variations in load demand and RES outputs.

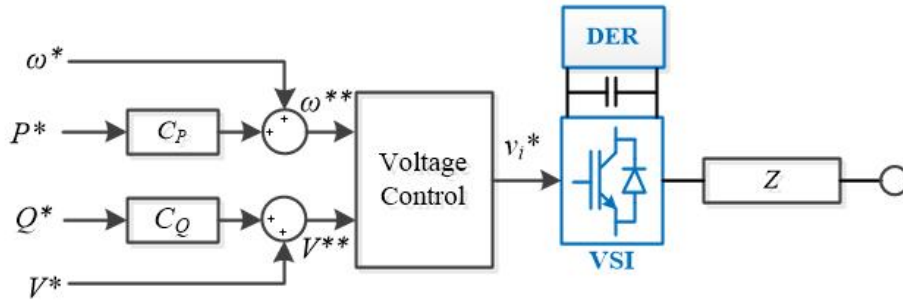


Fig. 2.9. Grid-support grid-forming inverter type with VSI and DER.

To mitigate the operational burden of single grid-forming unit, multiple grid-forming unit with the droop control can be operated for power sharing in isolated inverter-based MGs. This unit called grid-support grid-forming converter as shown in Fig. 2.9 [47]. The basic control structure of grid-support grid-forming unit is shown in Fig. 2.10.

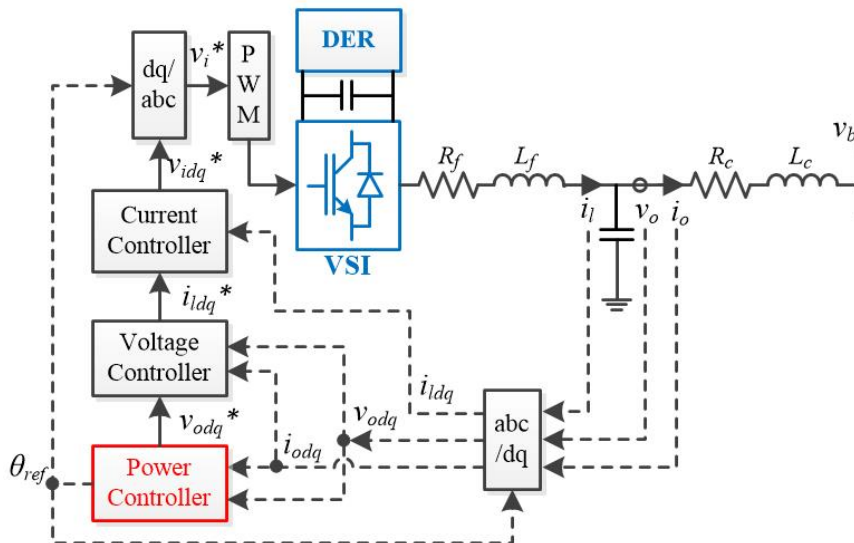


Fig. 2.10. Basic control structure in a three-phase grid-support grid-forming voltage source inverter generating a sinusoidal voltage with ω^* and V^* , calculated by the power controller with droop control.

The grid-support grid-forming units are mainly responsible for the MG frequency and voltage stability by sharing the power among grid-support grid-forming units required for the balance with the load demand. $P-\omega$ and $Q-V$ droop control, implemented on outer power controller, has been widely used to adjust the active and reactive power generation of each inverter. This controller generally uses a droop control for primary control using only local measurements and controllers without relying on a communication infrastructure. The local controller of the IDERs consists of outer power loop and nested control loops including voltage controller and current controller. The local controller is operated on the dq -frame and designed to form a reference voltage and frequency of inverter output and avoid over current by the limiter in a current control loop, which is same as those of grid-forming converter as shown in Fig. 2.8.

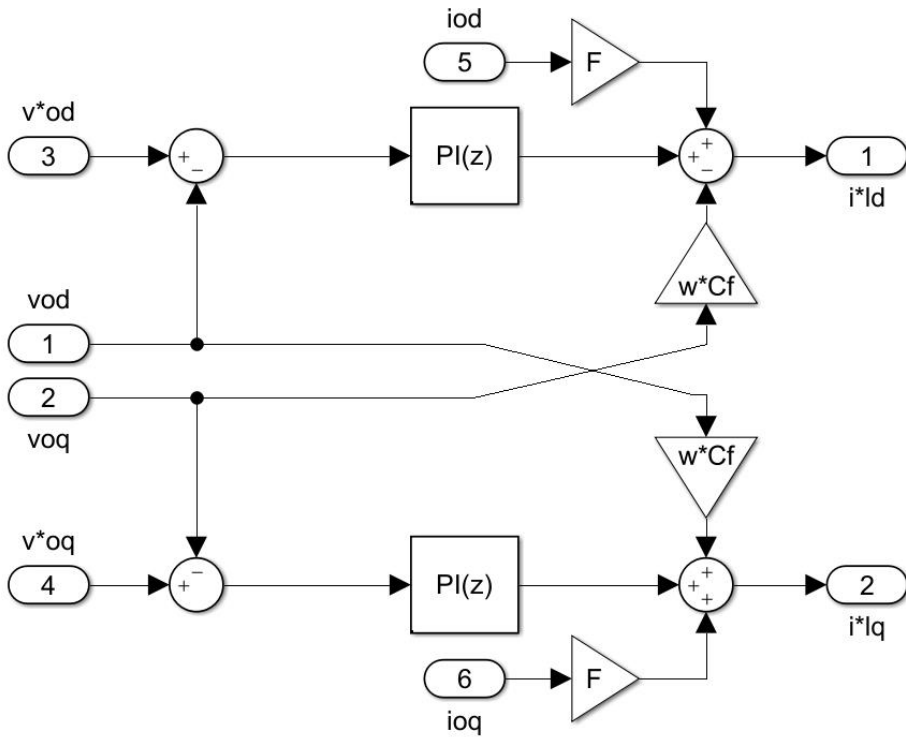


Fig. 2.11. Control block diagram of voltage controller in grid-forming unit.

The control block of outer voltage controller is shown in Fig. 2.11. The voltage controller receives a reference dq -axis output voltage from outer power controller and measured dq -axis output voltages and currents from local measurement, those of which as an input signal. The voltage reference signal is compared their measured value and processed by proportional integrator (PI) controller to provide an efficient tracking and regulation of the signal. The signal processed by PI controller also compared by feedforward signal, having a feed-forward gain constant F of measured output currents, for enhanced transient response. The equation of voltage controller can be expressed by the following equations:

$$i_{ld}^* = K_{pv}(v_{od}^* - v_d) + K_{iv} \int (v_{od}^* - v_d) dt - \omega C_f * v_{oq} + F * i_{od} \quad (2.3)$$

$$i_{lq}^* = K_{pv}(v_{oq}^* - v_q) + K_{iv} \int (v_{oq}^* - v_q) dt - \omega C_f * v_{od} + F * i_{oq} \quad (2.4)$$

where K_{pv} and K_{iv} are the proportional and integral gains for PI controllers in voltage controller, respectively, and C_f is a capacitance of the output filter.

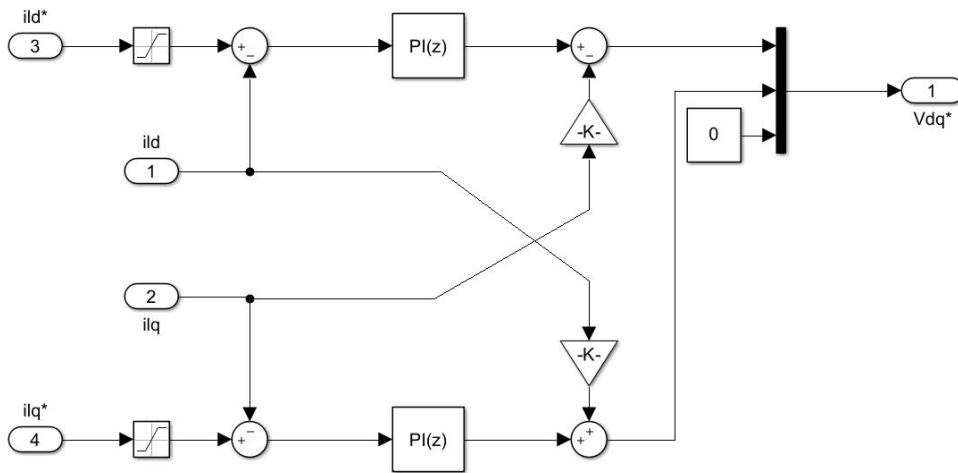


Fig. 2.12. Control block diagram of current controller.

The current controller, as shown in Fig. 2.12, aims to set the output voltage of inverter and prevent overcurrent during abnormal conditions such as a generator trip or a line fault. The dynamic equation of the current controller can be represented as

follows:

$$v_{od}^* = K_{pi}(i_{ld}^* - i_{ld}) + K_{ii} \int (i_{ld}^* - i_{ld}) dt - \omega L_f i_{oq}^* \quad (2.5)$$

$$v_{oq}^* = K_{pi}(i_{lq}^* - i_{lq}) + K_{ii} \int (i_{lq}^* - i_{lq}) dt - \omega L_f i_{od}^* \quad (2.6)$$

where K_{pi} and K_{ii} are the proportional and integral gains for the current controller's PI controller, respectively, and L_f is an inductance of the output filter.

On the other hand, the grid-feeding type inverters are controlled as current sources with high parallel output impedance as shown in Fig. 2.13. The grid-feeding inverter adjusts the output active and reactive power of the DER unit to the reference value P^* and Q^* without considering system state. Practically, most of the inverters (about 81%), to interface DERs are operated as grid-feeding unit [50]. For example, RESs with maximum power point tracking (MPPT) control are operated as a grid-feeding unit.

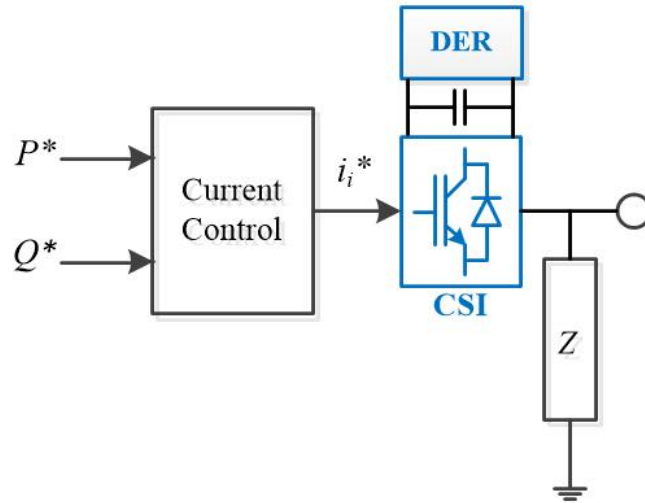


Fig. 2.13. Grid-feeding converter type with VSI and DER.

To help with the voltage and frequency stability of the system, the grid-feeding unit can be operated as grid-support grid-feeding unit, which is shown in Fig. 2.14. In grid-support grid-feeding control unit, ω - P and V - Q droop controls are

implemented for active and reactive power sharing with measured output voltage and system frequency as shown in Fig. 2.15. One example is a diesel generator connected to inverter-based MGs, which is used for grid support and source of charge (SOC) management.

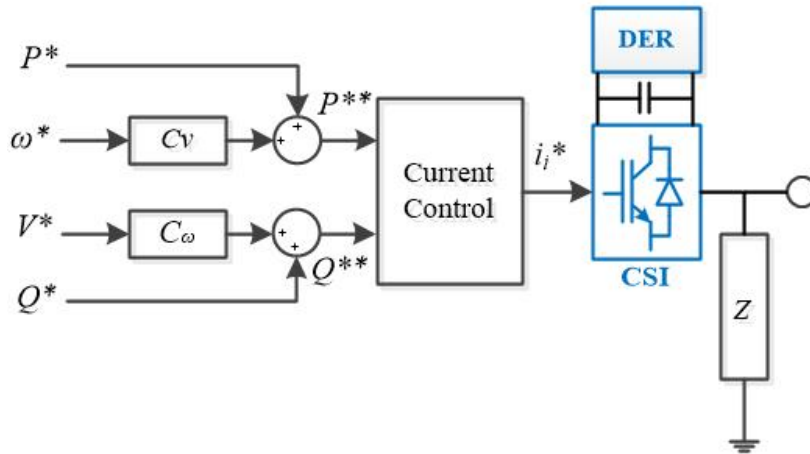


Fig. 2.14. Grid-support grid-feeding inverter type with VSI and DER.

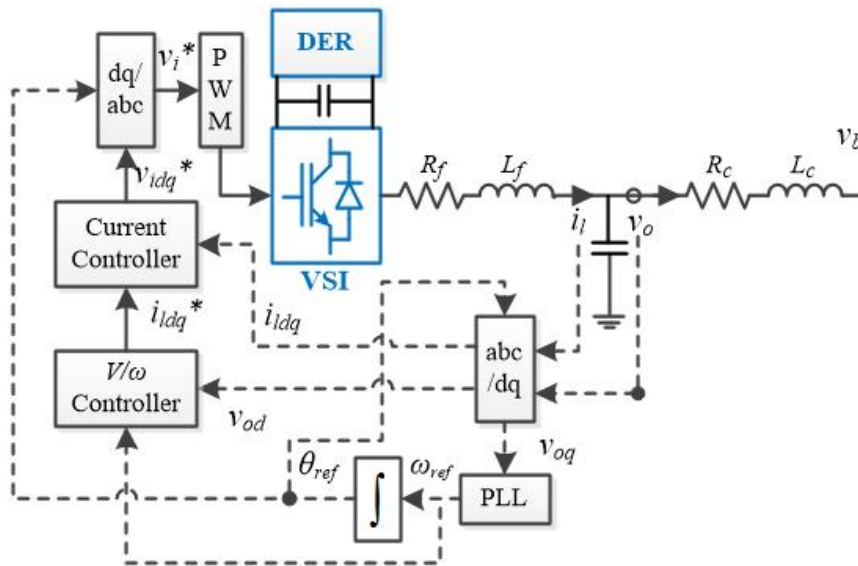


Fig. 2.15. Basic control structure in a three-phase grid-support grid-feeding current source inverter.

Control strategies for inverters in inverter-based islanded MG

In inverter-based islanded MGs, at least one inverter should be responsible for setting frequency and voltage of the MG system, while remaining inverters and other controllable units can support to achieve a power balance between generation and load demand acting as a grid-support unit. For autonomous operation of inverter-based islanded MGs, the IDER can generate reference frequency and voltage of system and react to network disturbances by using the local controllers and measurements available at its terminals. For proper coordination of IDERs and other controllable units, master-slave control scheme has been applied for DERs. Two main operation schemes for master-slave control depending on the number of master units can be applied for islanded inverter-based MGs as; i) SMO, ii) MMO [29].

In the SMO shown in Fig. 2.16, only one IDER regulates the reference voltage and frequency as a only one master unit by grid-forming control, while all the other DERs act as grid-feeding units, operated in PQ mode as slave units.

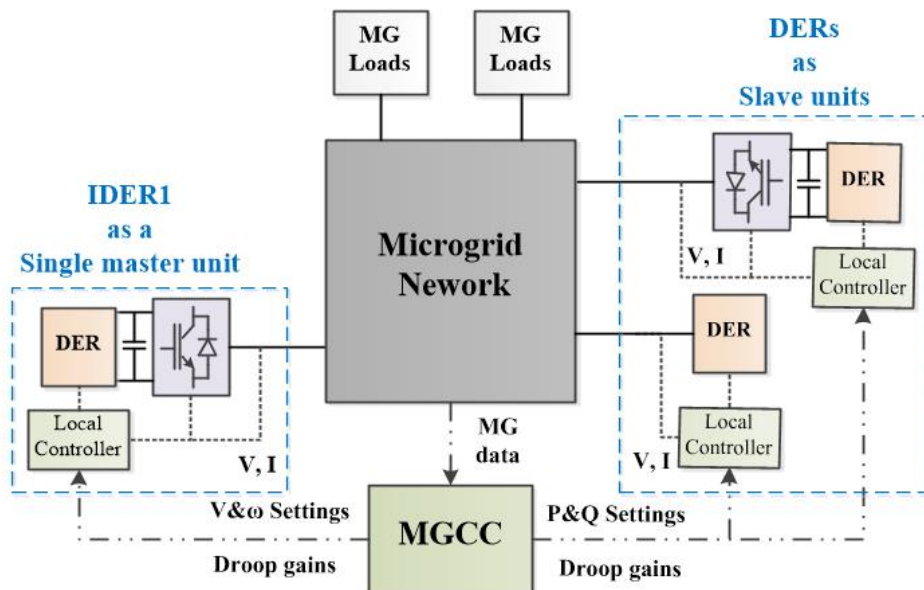


Fig. 2.16. General control scheme for SMO.

That is, the master unit acts as a VSI and the slave units operate as current source inverters. In the SMO, a simple control scheme at local controller can be applied. A CVCF control scheme is representative example of a SMO. In addition, it has been widely observed in these MGs that a dispatchable, IDER can act as a grid-forming master unit in charge of providing the primary spinning reserve to the MG and sending the frequency signal to multiple slave units. For cooperation, dispatchable DERs and other controllable units, acting as slave units, are known to be capable of adjusting their power outputs according to the frequency signal.

To achieve high penetration of renewables in such MGs, a BESS often acts as a grid-forming unit that is primarily responsible for the real-time balance between power supply and demand in the system, while compensating for the intermittent power outputs of RESs [15]–[27], [51], [52]. A MG system operator can access the BESS inverter and control the charging or discharging power of the battery within a short period of time, while maintaining SOC) within an acceptable range for device protection and continuous use for other MG operating schemes (e.g., economic dispatch).

Other DERs can be considered as grid-feeding units that follow the reference signals of active and reactive power. Diesel generators are widely used as auxiliary units that perform the secondary control to maintain the SOC level of the BESS within an acceptable range [18]–[27], [52]. However, SMO has a reliability problem with the failure of only one master unit and system is difficult to expand. This issue can be successfully resolved using a MMO, having multiple masters can operate as grid-support grid-forming units, incorporated with droop control scheme.

In a MMO scheme shown in Fig. 2.17, several inverters, at least two inverters can be operated as a voltage source by grid-support grid-forming with pre-determined $P-\omega$ and $Q-V$ characteristics. Eventually, other slave units, acting as a current source by grid-support grid-feeding, may also coexist. The main advantages of this approach are as:

- Simple expansion of the system
- Increased redundancy and enhanced reliability compared to SMO (i.e., even if one master unit is failure, it can be operated by using other master units)
- A simplified supervisory control with more complex control tasks assigned to the components

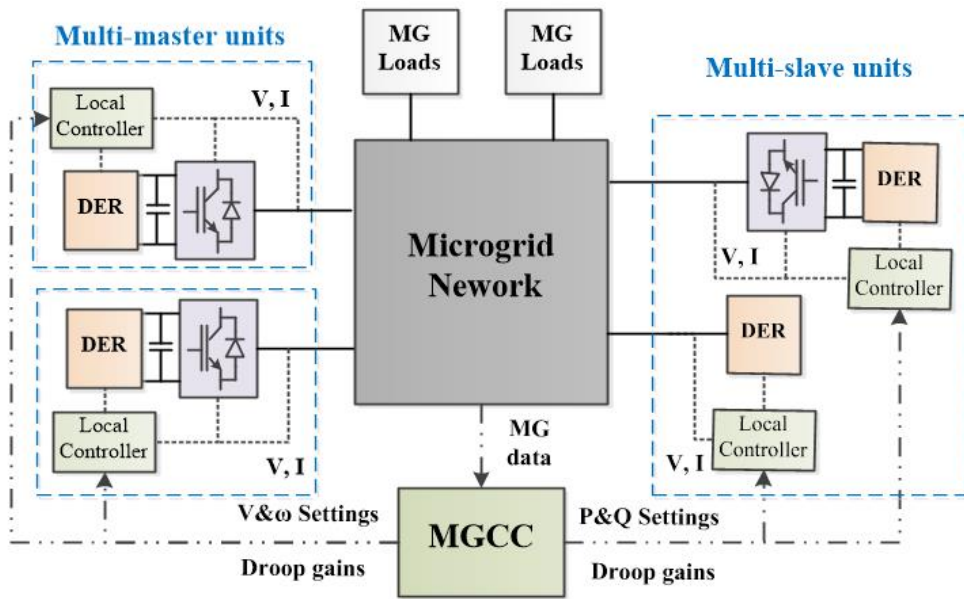


Fig. 2.17. General control scheme for MMO.

2.2 Load-voltage Dependence in Power Systems

2.2.1 Basic load modeling

To ensure the sustainable operation of an islanded MG, the power supply by DERs should always be balanced with the electrical load on the MG system. Consequently, the load characteristics have an impact on both the system reliability and stability. Thus, the load modeling, referred to the mathematical representation of the relationship between the power consumption of load and voltage/frequency in a load bus, is essential part for power system analysis, control, operation, and planning [53]. However, the accurate modeling of power system load is very complicated due to the large number of devices having various load type such as motors, lamps, heaters, compressors, and so on. Moreover, the load composition is continuously changed depending on many factors such as time, weather conditions, and other various situations. Therefore, the load modeling mainly aims to develop simple mathematical models to approximate and reflect complicate and composite load characteristics.

In recent years, load modeling has been received more attention to improve a modelling accuracy and consider the characteristics of modern load related with smarter grid such as electric vehicles, demand side management including demand response and CVR. The load modeling approach consists of two main steps as [54]:

1. Selecting an appropriate load modeling structure
2. Identifying the parameters for load model

The load models can be classified into two broad categories: static and dynamic models. In this dissertation, static load model is only considered for simulation. Note that static load model is inaccurate at low voltages.

Static Load models

Static load models represent the load characteristics, expressed active power and reactive power, respectively, at any instant of time as algebraic functions of voltage magnitudes of load buses and system frequency at that instant [55]. This modeling approach uses simple algebraic functions and can be used to determine static loads characteristics such as resistive loads and approximate for dynamic loads such as motors and compressor.

Exponential model

Traditionally, the exponential model has been used to represent the relationship for the load demand and the voltage at a load bus by the simple exponential equations. In this modeling methods, the voltage dependence of load characteristics can be expressed by the separated exponential model for active power and reactive power with voltage. Using exponential model, load demand can be represented in terms of bus voltage [53] as:

$$P = P_0 \left(\frac{V}{V_0} \right)^{n_p} \quad (2.6)$$

$$Q = Q_0 \left(\frac{V}{V_0} \right)^{n_q} \quad (2.7)$$

where P_0 and Q_0 are active and reactive power demands at the rated operating voltage V_0 . In addition, P and Q are active and reactive power demands for actual bus voltage V . Furthermore, n_p and n_q are the exponents that vary depending on the inherent characteristics of the load devices. These exponents essentially represent the sensitivities of the load demands with respect to the bus voltage V : i.e., $\partial P / \partial V$ and $\partial Q / \partial V$ at $V = V_0$. In [38], the average value of n_p was known to be between 1.1 and 1.7. In isolated MGs, n_p is expected to be larger, due to the high proportion of resistive loads such as heating and lighting [38]. The average value of n_q is usually between 1.5 and 6 in a bulk power system [53].

ZIP model

The ZIP model for load modeling is represented by polynomial equation of the bus voltage magnitude with active and reactive power demand of the load, that composed of constant impedance (Z), constant current (I), and constant power (P) components [55]. This alternative model has been commonly adopted in power system analysis as:

$$P = P_0 \left[Z_p \left(\frac{V}{V_0} \right)^2 + I_p \left(\frac{V}{V_0} \right) + P_p \right] \quad (2.8)$$

$$Z_p + I_p + P_p = 1 \quad (2.9)$$

$$Q = Q_0 \left[Z_q \left(\frac{V}{V_0} \right)^2 + I_q \left(\frac{V}{V_0} \right) + P_q \right] \quad (2.10)$$

$$Z_q + I_q + P_q = 1 \quad (2.11)$$

Table 2.1. ZIP Model parameters of electrical appliances [56].

Load	Z_p	I_p	P_p	Z_q	I_q	Q_q
Air Conditioner	1.6	-2.69	2.09	12.53	-21.1	9.58
CFL bulb	-0.63	1.66	-0.03	-0.34	1.4	-0.06
Elevator	2.36	-4.15	2.79	11.7	-19.5	8.81
Incandescent light	0.54	0.5	-0.04	0.46	0.51	0.03
LED Light	0.69	0.92	-0.61	1.84	-0.91	0.07
Microwave	-0.27	1.16	0.11	15.64	-27.7	13.1
Resistive Heater	0.92	0.1	-0.02	0.15	0.86	-0.01
PC	0.18	-0.26	1.08	-0.19	0.96	0.23

where Z_p , I_p , and P_p are the constant impedance, constant current, and constant power coefficients of active power demand, respectively. Similarly, Z_q , I_q , and Q_q are the

ZIP coefficients of reactive power demand, respectively. The sum of the three coefficients must be equal to one, as shown in (2.9) and (2.11), to meet the rated operating condition. The low-voltage load modeling for LV networks is studied using ZIP and exponential models [56]. Table 2.1 shows the ZIP model coefficients of typical electrical appliances.

Frequency dependent model

The power consumption of the load is also affected by system frequency variations. In a bulk power system, the system frequency is controlled and maintained near the rated value. However, the islanded MG, especially synchronous-machine-based islanded MG is vulnerable to both frequency and voltage fluctuations, thus the frequency dependent model can be more suitable for the synchronous-machine-based islanded MG, which has low inertia and slow dynamic responses compared to IDERs. The frequency dependent model is usually expressed by multiplying the exponential model or polynomial ZIP model by a factor, depending on the system frequency as follows:

$$P = P_0 \left(\frac{V}{V_0} \right)^{n_p} (1 + K_{pf} \Delta f) \quad (2.12)$$

$$Q = Q_0 \left(\frac{V}{V_0} \right)^{n_q} (1 + K_{pf} \Delta f) \quad (2.13)$$

$$P = P_0 \left[Z_p \left(\frac{V}{V_0} \right)^2 + I_p \left(\frac{V}{V_0} \right) + P_p \right] (1 + K_{pf} \Delta f) \quad (2.14)$$

$$Q = Q_0 \left[Z_q \left(\frac{V}{V_0} \right)^2 + I_q \left(\frac{V}{V_0} \right) + P_q \right] (1 + K_{pf} \Delta f) \quad (2.15)$$

where Δf is the system frequency deviation that is equal to $f - f_0$, and K_{pf} and K_{qf} are the frequency sensitivity parameters for active and reactive power, respectively, the

active power and frequency sensitivity coefficient ranges from 0 to 3.0, and that of reactive power ranges from -2.0 to 0 [57].

Modeling approach to determine model parameters

There are two type of approach to identify model parameters to determine system load characteristics: measurement-based and component-based, so called physically-based modeling method. The measurement-based approach uses data acquisition equipment to collect measurement data and derive load characteristics. The component-based approach is to obtain a mathematical function can represent the physical characteristics of loads, it aggregates model of various load components to form a combined model.

A measurement-based method, which is a bottom-up approach, starts from the measured data, while a component-based one, as a top-down approach requiring three datasets: Load class, components, and characteristics, start from the individual components as illustrated in Figs. 2.18. and 2.19. The two methods are summarized in Table 2.2.

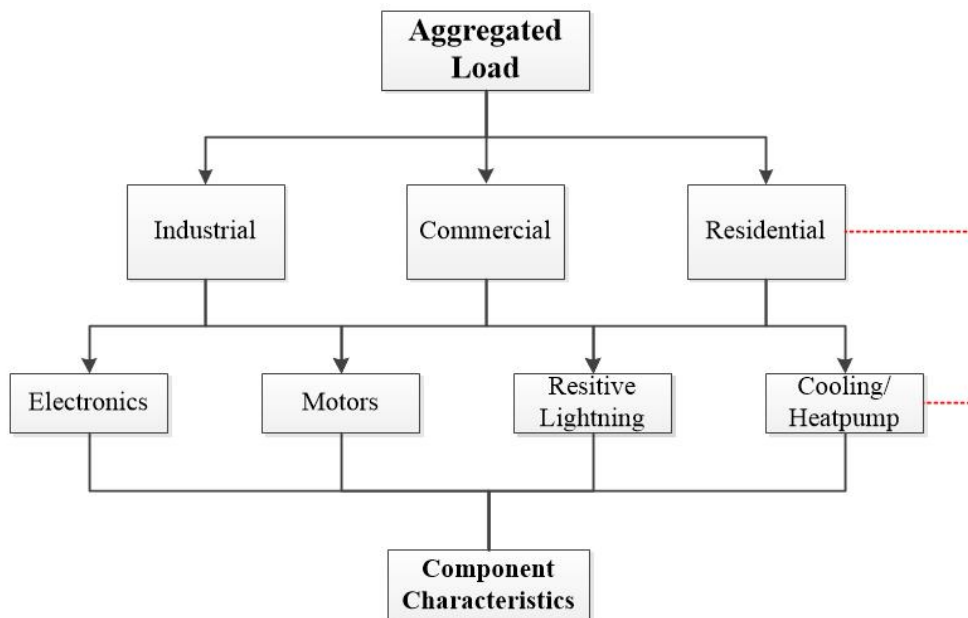


Fig. 2.18. Component-based modeling approach [54].

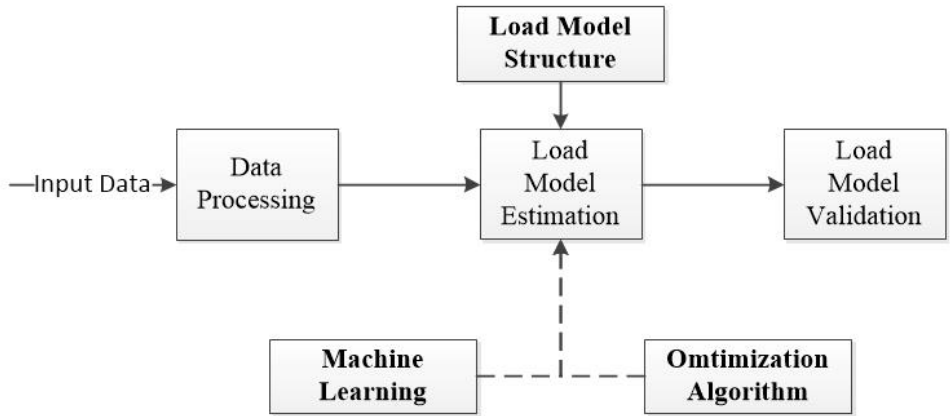


Fig. 2.19. Measurement-based modeling approach [54].

Table 2.2. Comparisons of two approaches for load modeling [54].

	Advantages	Disadvantages
Component-based	<ul style="list-style-type: none"> - Field measurement is not required - Physical representation of end-use devices - Can be applied to different operation conditions - Demand side management is Considered 	<ul style="list-style-type: none"> Unable to account for different operation conditions - Models are developed using data measured in certain periods at specific locations, which lacks generalizability - Measurements with large disturbances are hard to obtain
Measurement-based	<ul style="list-style-type: none"> - Based on gathered data from actual systems - Provide accurate models for measured locations and time - A generic method that can be applied to various models - No need to have deep knowledge of loads 	<ul style="list-style-type: none"> Requires characteristics of individual load components. - Accurate and comprehensive load composition information is hard to obtain - Low adaptability to the integration of new loads

2.2.2 Conservation voltage reduction

Overview and concept of CVR

CVR, an established and well-known idea for power system operation, aims to decrease load demands by regulating bus voltages at a low level (typically limited to from 2% to 3%). This technique is one of the most cost-effective way to save both energy and power, and has been widely adopted by utilities and system operators. Note that the reduced voltage level by CVR must be within acceptable range. It is mature technology that has proven its effectiveness in studies and demonstrations in various regions of many countries [37], [58], and [59].

The CVR has also been routinely implemented in decades in developing countries to provide electric power to more customers while reducing power quality. The conventional CVR has been implemented at the distribution level without DERs, and it has been controlled mainly in the form of volt/var control (VVC) using voltage regulation devices such as shunt capacitors, load tap changers (LTCs), and synchronous condenser (SCs).

In recent year, DERs have a tendency to be integrated into distribution networks and MGs. DERs can make the bus voltage and voltage profile change more quickly, thus may improve the effect and range of CVR in the systems. Moreover, the cost of electricity is steadily growing, and makes the CVR a more attractive option. In order to apply CVR effectively, the following three aspects must be considered as:

- Coordination of different volt/var control devices to reduce voltage in an optimal and reliable way
- Assessment and verification of CVR effects
- Coordination between CVR and DERs

There are two purposes in applying CVR into the distribution systems and MGs: i) short-term demand reduction; ii) long-term energy reduction; as shown in Fig 2. 20.

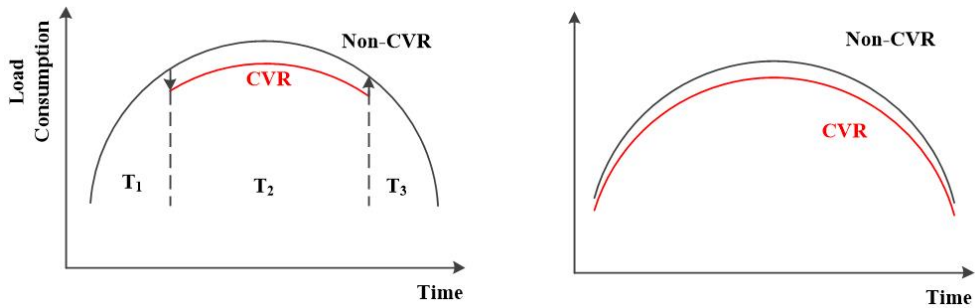


Fig. 2.20. Two ways to perform CVR: (left) Peak demand reduction and (right) 24-hr energy reduction [58]

The Fig. 2.20 on the left shows the CVR for reducing peak demand, during peak hours (T_2) the CVR is performed to drop the voltage, and consequently reducing peak demand. The right plot of Fig. 2.20 illustrates the long-term energy reduction by CVR. As shown in Fig.2.20, the CVR can be utilized for both peak demand and energy reduction, by the effect depends on the load characteristics, which is discussed in the Chapter 2.1.

In addition, the benefits of CVR for power system utilities include net loss reduction of the system, increasing social welfare such as fuel consumption and emission reduction, and potential incentives and requirements from regulatory (e.g., California Public Utilities Commission encouraged utilities to implement CVR, Northwest Power and Conservation Council performed extended research on CVR incentives [60]).

It is recommended to follow the voltage standard in order to perform CVR without harm to the consumer. American national standards institute (ANSI) standard C84.1, first developed in the 1960s and have been a landmark document for customer voltage standard, sets the voltage range at the distribution transformer secondary terminals to establish a high quality power supply standard for residential customers [61]. The voltage range at the customer is set to $\pm 5\%$ of its rated value, as shown in Fig. 2.21.

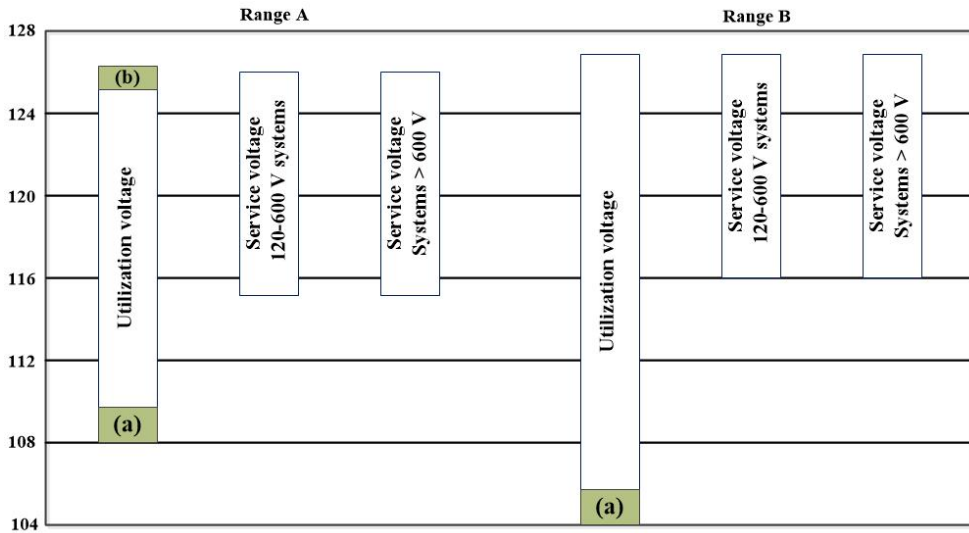


Fig. 2.21. ANSI standard C84.1 (a): Not available at light loads, (b): Not available at 120-600 V systems [61].

For the MGs, it is suggested in the IEEE 1547.2 Standard that MG bus voltages should be maintained between 0.88 pu and 1.10 pu under normal operating conditions [62]. In addition, national electrical manufacturers association (NEMA) recommends that all electrical appliances and motors should operate at nameplate $\pm 10\%$ satisfactorily. The national electrical code allows up to a 5% drop. The national steady state voltage regulation standards can be summarized as Table 2.3

Table 2.3. National steady state voltage regulation standards [63].

Nominal Standard	Service $\pm 5\%$	Utilization -13%, +6%	Nameplate Motor	NEMA $\pm 10\%$
120	114 - 126	104.4 – 127.2	115	103.5 – 126.5
208	197.6 – 218.4	181 – 220.5	200	180 – 220
240	228 – 252	208.9 – 254.4	230	207 – 253
277	263.2 – 290.9	241 – 293.6		
480	456 - 504	417.6 – 508.8	460	414 - 506

Assessment of CVR effect

Assessing the effectiveness of CVR is an important issue in implementing CVR on the distribution systems and MGs. The effect of CVR can be evaluated by the conservation voltage reduction factor (CVR_f) as:

$$CVR_f = \frac{\Delta E\%}{\Delta V\%} \quad (2.16)$$

where $\Delta E\%$ is the percentage of energy saving and $\Delta V\%$ is the percent voltage reduction. the value of E can be considered in active power, reactive power, and energy, respectively. 1:1 ratio (1% voltage reduction produces 1% reduction in peak demand and 1% energy saving) has been a “Rule of Thumb” in the industry (i.e., $CVR_f = 1$). However, in a recent study [37], the $CVR_{f(kw)}$ and $CVR_{f(kwh)}$ for modern distribution and load conditions is about 0.75 (ranges between 0.7 and 0.95), that is slightly less than the value of “Rule of Thumb”. Assessment methodologies for CVR_f can be classified into four categories as:

- Comparison-based method
 - Select two similar feeders and compare treatment group (CVR) and control group (Non-CVR) in the same performance period.
 - Perform a CVR test on a feeder and apply normal voltage to the same feeder under similar conditions.
- Regression-based method
 - Normal-voltage and reduced voltage loads are modeled as a function of their impact factors, and compared to calculate CVR_f .
- Synthesis-based method
 - Aggregate LTV behaviors to estimate the CVR_f .
- Simulation-based method
 - Based on system modeling and power flow calculation

These four representative methods are well described in detail in previous research [58]. The summary of CVR_f derived by various utilities and institutes are summarized in Table 2.4.

Table 2.4. Summary of CVR effect.

	Year	CVR_f	Comments
American Electric Power [64]	1978	0.62	For kWh Residential: 0.62 Commercial: 0.89 Industrial: 0.35
Northeast utilities [65]	1987	1	For kWh Average value (0.57-1.35)
Snohomish PUD, WA Northwest Utilities [66]	1991	0.62	For kWh
BC Hydro [67]	1995	0.7	For kWh Spring: 0.60 Summer: 0.77
Northwest Energy Efficiency Alliance [60]	2005	0.8	For kWh National average
Electric Power Research Institute [68]	2011	0.62	For kW Average value $CVR_{f(kVAR)}: 3.0$
Korea Electric Power Corporation [69]	2017	0.75	For kW Average value $CVR_{f(kVAR)}: 11.5$

Implementation of the CVR

The techniques to reduce voltage can be divided into two categories as:

- Open-loop methods
- Closed-loop VVC

The open-loop method is simple and early techniques for CVR by LTC, line drop compensation (LDC), voltage spread reduction, capacitor-based reduction, and home voltage reduction [70]. Among them, LTC and LDC are the most popular method for CVR. LTC is used to control the substation secondary voltage and almost available in all substations, which implies that very little cost is required to implement CVR. CVR by LTC is limited by the voltage spread due to line voltage drop and usually only lowers 2 to 3%. LDC is typically used to keep the most distant load above some minimum voltage levels by LTC, or static voltage regulators (SVRs).

However, there are three kinds of disadvantages for open-loop methods:

- Limited CVR level
- Hard to be optimized
- Difficult to respond to dynamic changes

On the other hand, the closed-loop feedback control methods can be applied for CVR with various measurements from supervisory control and data acquisition system (SCADA) and/or the advanced metering infrastructure (AMI). It enables that the CVR operates optimally in the system. This result in more effects and the CVR can be used to cope with system dynamic changes by utilizing various data. However, this approach needs a communication link to gather data from the measurements in the system and complex calculation to solve optimization problem. Therefore, it is necessary to apply a suitable method appropriate to the situation such as budget, availability of equipment, and existing infrastructure of each system.

Application of the CVR to islanded MGs

When CVR concept is applied to the MGs, the conventional methods used in the existing distribution system can be easily applied in grid-connected mode. However, in islanded mode, there is no presence of a utility grid which can regulate the overall voltage level. Therefore, a different approach than the existing method is needed as previous research in [37]–[40].

For example, in [38], the output voltages of synchronous machine-based DERs at the point of common coupling (PCC) were controlled by using MG frequency deviation as a common input signal for the proportional-integral (PI) controllers of the exciters. The other DERs located at different buses operated simply as slave units to supply the pre-determined active power, regardless of the PCC voltage. In [39], the ACVR approach was implemented using $V-I$ droop control of the IDERs in an islanded MG. However, the voltage reduction became large under light loading conditions, when the load demand reduction was not much required. On the contrary, the ACVR was rather limited under heavy loading conditions, when the load reduction was more valuable. In [40], coordination between ACVR and load shedding was discussed using $P-\omega$ and $Q-V$ droop controllers for inverter-based MGs. A ACVR strategy was implemented based on the variation in the apparent output power of each IDER, leading to different extents of voltage reduction at each bus when the IDERs operated under different droop coefficients and power ratings. Moreover, for the ACVR approaches discussed in [38]–[40], the small-signal stability needs to be investigated in more detail before they can be applied in practical situations.

Chapter 3. Autonomous Power Management Strategy for Single-Master Operation

This dissertation proposes a new autonomous control scheme integrated with frequency-bus-signaling and droop control based on a single-master configuration mainly to improve power sharing and real-time power balancing under the condition where serious disturbances occur in an islanded MG. In coordination with the CVCF controller, the proposed scheme enables the BESS to control the MG system frequency in response to the change in AC voltages, given that unexpected voltage changes at the grid-forming converter bus indicate the instantaneous active power imbalance in the MG system [36].

The proposed scheme enables autonomous power management in the MG via the coordination of the BESS with other DERs (particularly for the condition of lack of power generation), minimizing the frequency and voltage deviations. Simulation case studies are performed using detailed models of an isolated MG in South Korea implemented with real parameters. Case study results demonstrate the effectiveness of the proposed control scheme in [73] mainly from the aspects of the following key advantages:

- Given extreme disturbances (such as a trip of the DGs), real-time power balance in an isolated MG is achieved without using communication infrastructure.
- It has a simple structure and hence can be easily implemented in the outer control loop of the grid-forming BESS while ensuring the normal operations of inner control loops and, consequently, the device-level stability.
- Only the CVCF control is activated under normal operating conditions, minimizing the fluctuation of MG frequency and active power of other

slave units such as DGs.

3.1 System description

3.1.1 Grid-forming BESS as a single-master unit

A grid-forming BESS can be used for regulating the AC bus voltage and frequency by balancing power supply and demand in an islanded MG [74], [75]. The BESS consists of a battery pack, an LC filter, an inverter, and a transformer (see Fig. 3.1). It operates as an AC voltage source and determines the levels of MG system frequency and voltage by using conventional nested voltage and current control loops that operate on the dq -reference frame. The BESS detects the instantaneous power imbalance by measuring the capacitor voltage V_c and recovers it to the reference value with the internal voltage and current controller. In the conventional CVCF control scheme, the dq -axis voltage and frequency references are set to their rated values: i.e., $V_d^* = 1$ pu, $V_q^* = 0$, and $f^* = 1$ pu [76]. The active and reactive power outputs of the BESS are indirectly controlled to maintain the bus voltage to the rated value. In this study, the frequency reference is calculated to share active power with other DERs by the proposed voltage-frequency proportional controller (VFPC), based on the level of voltage deviation, as explained in Chapter 3.2 in detail.

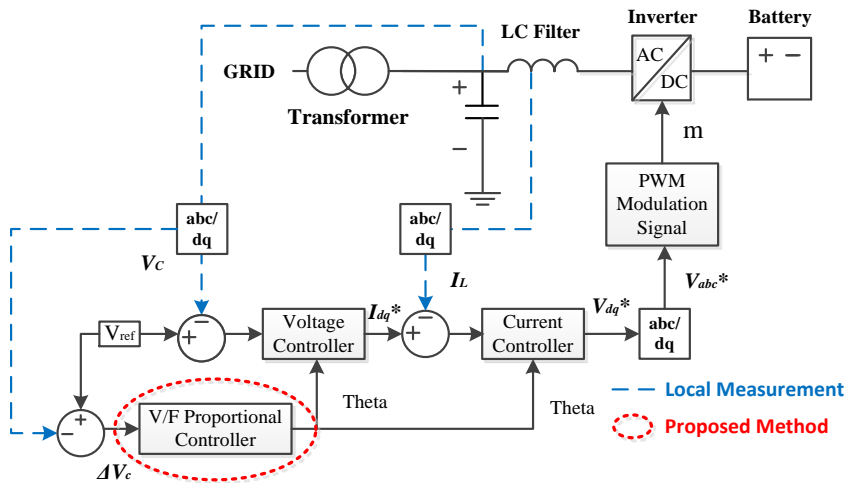


Fig. 3.1. A schematic diagram of the grid-forming BESS and its device-level controllers.

3.1.2 Diesel generator as a slave unit

Droop control is widely applied to improve the grid operational performance, stability, and reliability. It is based only on local measurements and allows generators in the system to operate autonomously. A droop control scheme is adopted such that the diesel generators, as a slave unit, can share active power with the BESS for real-time power balance. The droop control for power sharing can be expressed as (2.1) and (2.2).

Fig. 3.2 shows a schematic diagram of the active power controller, valve actuator, and diesel engine block of the diesel generator. It includes an active power droop controller and a PI controller for time-delay dynamic models of a valve actuator, a diesel engine, and a synchronous machine. Note that the synchronous machine was modelled using the SI fundamental block in the MATLAB/Simulink. The parameters related to the controller are determined using those provided in [24]. The droop controller generates ω_{ref_di} and the PI controller is used to track the reference signal by comparing ω_{ref_di} and ω_{m_di} . Note that ω_{m_di} is the measured angular frequency of a diesel generator.

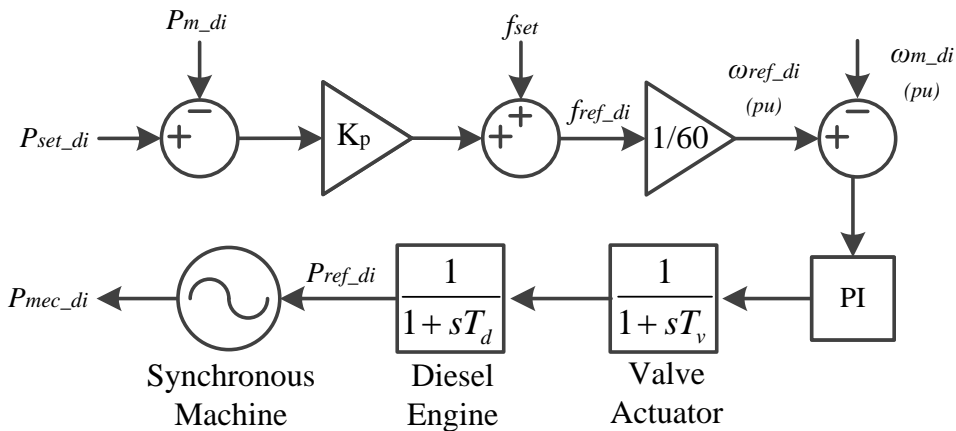


Fig. 3.2. A schematic diagram for the active power controller and system dynamics of the diesel generator.

The active power droop control can be expressed as:

$$f_{ref} = f_{set} - K_p(P_m - P_{set}), \quad (3.1)$$

where f_{ref} is the reference frequency of a generator and f_{set} and P_{set} are the presets of microgrid frequency and active power determined by the microgrid operator, respectively. P_m is a measured value of active output power of a generator and K_p is a droop coefficient that can be determined considering the operating frequency range in a microgrid as:

$$K_p = \frac{a(f_{nom} - f_{min})}{P_{nom}}, \quad (3.2)$$

where f_{nom} and f_{min} are the nominal and minimum values of the grid frequency, respectively. Moreover, P_{nom} is the nominal active power of a generator and a is a constant for determining the droop coefficient.

Similarly, the droop controller is widely used for reactive power control and consequently AC voltage control, as shown in Fig. 3.3. It consists mainly of a reactive power droop controller, a PI controller, and a transfer function model of an exciter.

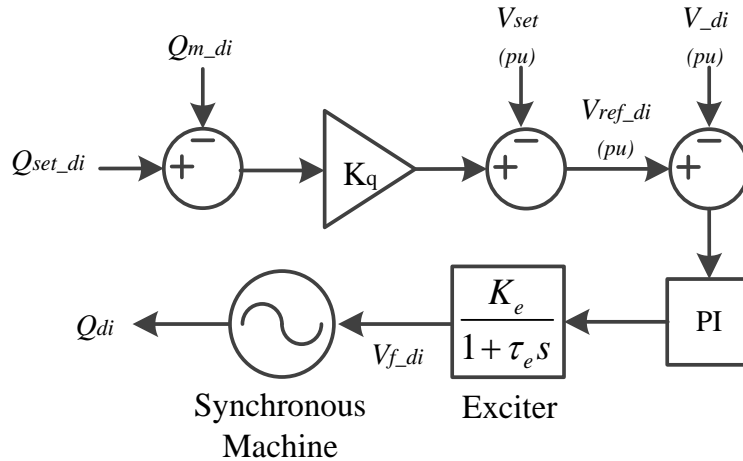


Fig. 3.3. A schematic diagram for the reactive power controller and exciter block of the diesel generator.

The reactive power control can be represented using the reactive droop coefficient K_q as:

$$V_{ref} = V_{set} - K_q (Q_m - Q_{set}) \quad (3.3)$$

$$K_q = \frac{b(V_{nom} - V_{min})}{Q_{nom}} \quad (3.4)$$

In (3.3), V_{ref} is the reference value of the bus voltage of a diesel generator. The values of V_{set} and Q_{set} correspond to the preset values of bus voltage and reactive power, respectively. In addition, Q_m and Q_{nom} are the measured and nominal reactive powers of a generator. Moreover, V_{nom} and V_{min} denote the nominal and minimum voltages of the system and b is a constant for determining the reactive power droop coefficient.

3.1.3 Active power balance equation in an isolated MG with CVCF control

Under the normal operating condition where the grid-forming BESS has sufficient power reserve to cover the active power change of a system, the active power balance can be satisfied as:

$$\Delta P_{BESS} = \Delta P_{Load} + \Delta P_{Loss} - \Delta P_{DG} \quad (3.5)$$

where ΔP_{BESS} and ΔP_{DG} are the variations in the active power outputs of the grid-forming BESS and the DGs, respectively. ΔP_{Load} is the variation in the rated load demand and ΔP_{Loss} is the variation in active power losses in the MG. In contrast, the active power output of the BESS reaches its limit when the BESS does not have a sufficient power reserve. This limit can be estimated as:

$$\Delta P_{BESS_max} = V_c (I_{d_max} - I_{d_set}) \quad (3.6)$$

where ΔP_{BESS_max} is the maximum variation in the active power output of the BESS. In (3.6), I_{d_max} and I_{d_set} are the maximum and preset values, respectively, of d-axis current. In this situation, the BESS cannot recover the voltage completely and,

consequently, the load shedding is initiated by the bus voltage reduction to achieve the active power balance in the MG, as shown in (3.7) and (3.8).

$$\Delta P_{BESS_max} = \Delta P_{Load} + \Delta P_{Loss} - \Delta P_{DG} - \Delta P_{Load_VR} \quad (3.7)$$

$$\Delta P_{Load_VR} = \sum \left[P_{Load_i0} \left\{ 1 - \left(\frac{V_i}{V_0} \right)^{n_{pi}} \right\} \right] \quad (3.8)$$

In (3.7), ΔP_{Load_VR} is a decrease in the total load demand at under-voltage buses. As shown in (3.8), the value of n_{pi} significantly affects the value of V_i at which the power balance in (3.7) is satisfied. The smaller n_{pi} , the bigger V_i that is required to induce the enough reduction of the load demand; this causes the degradation of voltage stability and even voltage collapse.

3.2 Proposed VFPC for autonomous power management

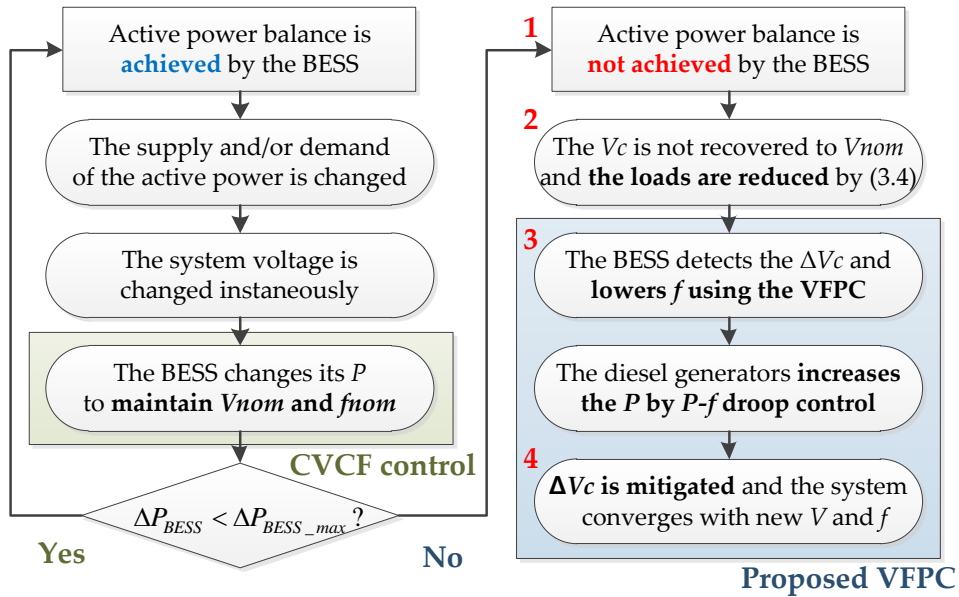


Fig. 3.4. Flow chart of the proposed VFPC for the autonomous power management at a primary control level.

The CVCF controller, discussed in Chapter 3.1, is effective in maintaining the voltages within the acceptable range particularly when the grid-forming BESS operates with sufficient primary reserve. Otherwise, a cooperative control scheme for the CVCF controller of the BESS and the local controllers of other DGs needs to be implemented to exploit the additional primary reserve capacities of the DGs for the reliable operation of the islanded/isolated MG.

The proposed cooperative control scheme aims at the active power sharing in an islanded MG when active power balance cannot be achieved solely by the CVCF controller of the grid-forming BESS. Fig. 3.4 shows the flow chart of the proposed method for the decentralised active power control. In the proposed method, the BESS operating with the CVCF controller detects insufficient active power supply in the MG by measuring the input voltage of the AC bus where the BESS is connected. It then controls the frequency proportional to the bus voltage deviation from the

nominal voltage. Further details on each module in Fig. 3.4 will be discussed in Sections 3.2.1 and 3.2.2.

3.2.1 Frequency control of BESS with VFPC

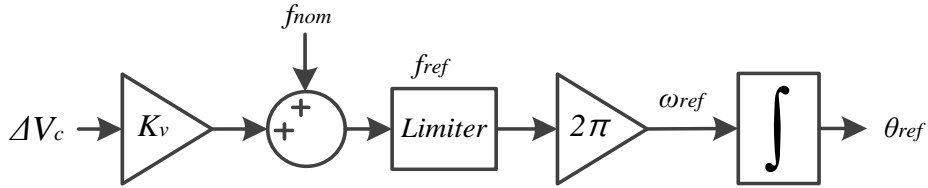


Fig. 3.5. A schematic diagram of the V - f proportional controller for the grid-forming BESS acting as single master unit.

In this chapter, a VFPC has been proposed to control the reference frequency of the grid-forming BESS, so that the primary active power reserve with the diesel generators is effectively exploited and shared in the MG system under a power shortage condition. Specifically, in Fig. 3.5, The reference frequency is determined as:

$$f_{ref} = f_{nom} + K_v \Delta V_c \quad (3.9)$$

where ΔV_c is the variation in the AC voltage estimated by subtracting the actual AC voltage measured at BESS bus V_c from the reference voltage of the BESS V^* . The coefficient K_v , denotes the proportional gain of the VFPC, which can be expressed as:

$$K_v = c \frac{f_{nom} - f_{min}}{V_{nom} - V_{min}} \quad (3.10)$$

where c is a constant to determine the V - f proportional gain. In Fig 3.5, the limiter consists of dead-band, rate-limiter, and saturation blocks to operate only when the primary reserve of the grid-forming BESS is smaller than the magnitude of the load demand variation. The VFPC enables the BESS inverter to determine the system frequency for a decrease in the AC voltage, as shown in (3.9) and (3.10), which is

measured at the input port of the inverter. The diesel generators then measure the reduced system frequency and increase their active power outputs by conventional $f-P$ droop controllers. Since the frequency is the same throughout the entire MG system, the proposed frequency-bus-signaling method for single master operation, which is discussed in Section 3.2.2, can achieve active power sharing in an autonomous manner.

3.2.2 Proposed autonomous power management

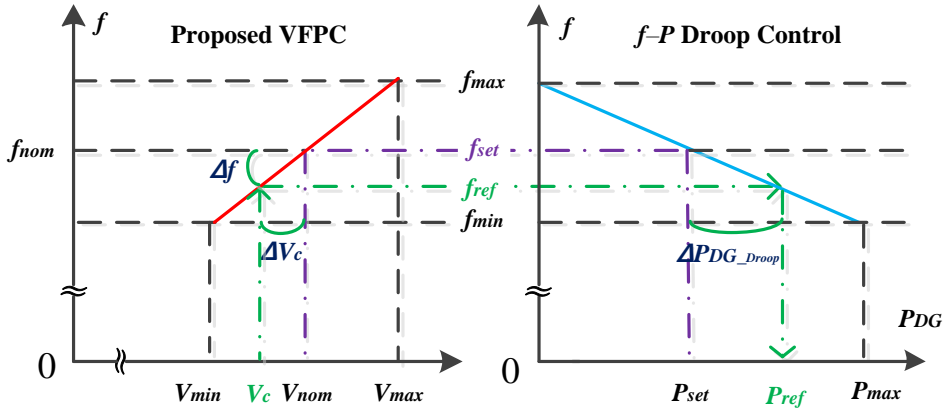


Fig. 3.6. Comparison between (a) the proposed control strategy (i.e., VFPC) of the grid-forming BESS and (b) the conventional control strategy (i.e., droop controller) of the diesel generators.

The proposed VFPC of the grid-forming BESS is activated only if the active power balance cannot be achieved because of lack of the primary reserve of the BESS. Specifically, the capacitor voltage V_c is not fully recovered to V_{nom} when the BESS has insufficient active power reserve and hence cannot compensate for all power imbalance in the MG system. The BESS controls the frequency (i.e., f_{set} to f_{ref}) proportional to ΔV_c , as shown in Fig. 3.6(a), and then controls the diesel generators with active power droop curves (i.e., P_{set} to P_{ref}), as illustrated in Fig. 3.6(b). Considering the VFPC operation, a new power balance equation is represented as follows:

$$\Delta P_{BESS_max} = \Delta P_{Load} + \Delta P_{Loss} - \Delta P_{DG} - \Delta P_{Load_VR} - \Delta P_{Load_FR} - \Delta P_{DG_Droop} \quad (3.11)$$

$$\Delta P_{Load_FR} = K_{pf} \Delta f * P_{Load_0} \quad (3.12)$$

$$\Delta P_{DG_Droop} = P_m - P_{set} = -\frac{1}{K_p} (f_{ref} - f_{set}) = -\frac{K_v}{K_p} \Delta V_c \quad (3.13)$$

where ΔP_{Load_FR} is a variation in the load demand for the change in the MG system frequency and ΔP_{DG_Droop} is the variation in the active power generation by droop control. In large-scale power systems, the load demand variation with respect to the frequency deviation can be characterized using the sensitivity coefficient K_{pf} in (3.12), which varies for the range from 0 to 3.0 [53]. However, in this dissertation, the load demand is assumed to remain unchanged for the frequency deviation for simplicity. This assumption is also valid because the reference frequency of the BESS is controlled to vary within a very small range, resulting in a slight variation in the system frequency. For the VFPC, (3.13) can then be derived from (2.1) and (3.9). (3.11) also can be expressed as:

$$\Delta P_{BESS_max} = \Delta P_{Load} + \Delta P_{Loss} - \Delta P_{DG} - \sum \left[P_{Load_i0} \left\{ 1 - \left(\frac{V_i}{V_0} \right)^{n_{pi}} \right\} \right] - K_{pf} \Delta f * P_{Load_0} + \frac{K_v}{K_p} \Delta V_c \quad (3.10)$$

The integration of the VFPC with the CVCF controller of the grid-forming BESS enables additional primary reserve from the diesel generators to be exploited for real-time power balance in the MG via their active power droop control loops. In this way, autonomous power management can be achieved for mitigating the active power shortage and the under-voltage, which often occur owing to the insufficient primary reserve of the BESS.

The proposed active power management strategy allows the grid-forming BESS to operate with the CVCF control under the normal condition where the BESS has sufficient primary reserve, so that the BESS can efficiently take charge of the primary reserve supply using its fast and accurate response characteristics. On the

other hand, the frequency-bus-signaling method using the proposed VFPC is adopted for active power sharing with the diesel generators only under the abnormal condition where the BESS has the limited primary reserve. Consequently, the power sharing issue in the conventional CVCF control can be effectively resolved in the proposed strategy, minimizing the system frequency variations and the active power fluctuations of other droop-based DGs. The sequential operations of the VFPC can be summarized as shown in Fig. 3.7.

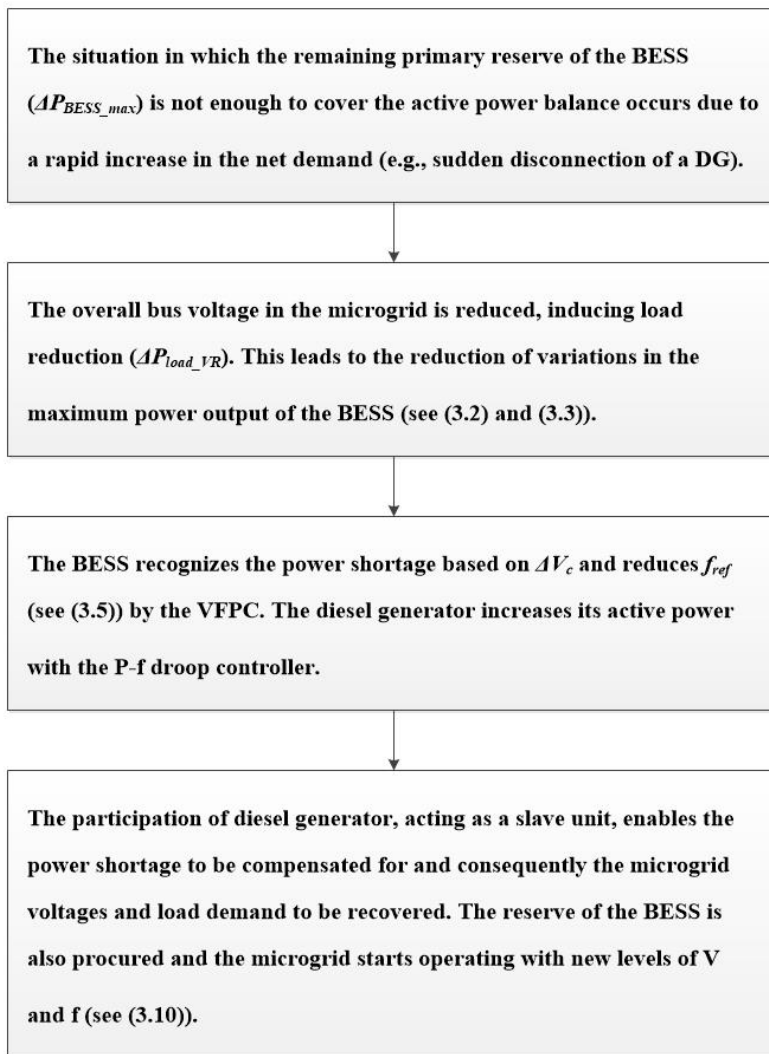


Fig. 3.7. Sequential operations of the VFPC.

Chapter 4. Autonomous Power Management Strategy for Multi-Master Operation

In this chapter, it is proposed that a frequency-based ACVR strategy using the proposed I_{dq} controller to provide a virtual reserve to the inverter-based islanded MG with MMO. The proposed method requires only the current outputs of IDERs for both power sharing and CVR, while still not relying on communications systems. In the proposed strategy, the $I_d-\omega$ and I_q-V droop controllers can mitigate inherent delay of P/Q measurements for $P-\omega$ and $Q-V$ droop controllers. It enables the IDERs to respond to faster than conventional controllers. Meanwhile, the I_d-V droop controller can improve both the system reliability and damping by inducing the frequency based ACVR.

The state-space models of the inverter-based MG with the proposed and conventional schemes are developed comprehensively to perform the comparative the small-signal analysis, so that the effectiveness of the proposed scheme in improving the steady-state stability is examined for various values of droop constants. Simulation case studies are also performed to demonstrate the effectiveness of the proposed control scheme under various loading conditions of the inverter-based MG, characterized by the factors such as load level, power factor, and load composition. The main contributions of proposed autonomous power management strategy for MMO are summarized as follows:

- the ACVR is achieved using an outer controller with a simple structure and consequently can be readily integrated with the outer feedback loops of the individual units for droop control;
- the virtual reserve can be more obtained under heavy loading condition in the islanded MG: i.e., when additional reserve is required;
- the small-signal analysis has been performed, consistent with the simulation case study results, to demonstrate that the proposed ACVR further improves

the stability and reliability of the inverter-based islanded MG.

4.1 Description of system with multi-master approach

4.1.1 Load model for MG system

A static load model, discussed in Chapter 2, is adopted to represent the active and reactive power demands (i.e., P_{Load} and Q_{Load} , respectively) of the variable load for actual bus voltage V as:

$$P_{Load} = P_0 \frac{\omega_l}{s + \omega_l} \left(\frac{V}{V_0} \right)^{n_p}, \quad (4.1)$$

$$Q_{Load} = Q_0 \frac{\omega_l}{s + \omega_l} \left(\frac{V}{V_0} \right)^{n_q}, \quad (4.2)$$

where P_0 and Q_0 are the active and reactive load demands, respectively, at the rated voltage V_0 . Moreover, n_p and n_q are the voltage exponents for active and reactive power, respectively, which are determined by the inherent characteristics of the load. In (4.1) and (4.2), ω_l is the cut-off frequency of the first-order low-pass filter (LPF) that reflects the transient load response for dynamic simulation in MATLAB/SIMULINK [54]. Note that (4.1) and (4.2) can be expressed equivalently using the ZIP coefficients [53].

4.1.2 MG forming of IDERs by multi-master units

As shown in Fig. 4.1, the IDER is a general type of a DER, such as a fuel cell, battery, or micro-turbine, which is connected to the network via a VSI. The VSI interface changes the DC output voltage from the DER to the AC voltage for the grid. An RLC filter is also required to have low ripple current on the grid side and set a resonant frequency at the desirable value [13]. The local controller of the IDER includes an outer feedback loop for the power (or proposed I_{dq}) controller that determines the voltage and frequency references required for the real-time power

addition, P and Q correspond to the low frequency components of the instantaneous active and reactive power, respectively, that are measured at the output ports of the LPFs in the power controller as:

$$P = \frac{\omega_c}{s + \omega_c} p_{ins}, \quad (4.6)$$

$$Q = \frac{\omega_c}{s + \omega_c} q_{ins}, \quad (4.7)$$

$$p_{ins} = v_{od} i_{od} + v_{oq} i_{oq}, \quad (4.8)$$

$$q_{ins} = v_{oq} i_{od} - v_{od} i_{oq}, \quad (4.9)$$

where v_{od} , v_{oq} , i_{od} , and i_{oq} are the dq -axis output components for voltages and currents of the IDER, respectively. Moreover, ω_c is the cut-off frequency of the LPF of power controller.

4.2 Proposed frequency-based ACVR with current-based droop controller

4.2.1 Proposed I_{dq} controller

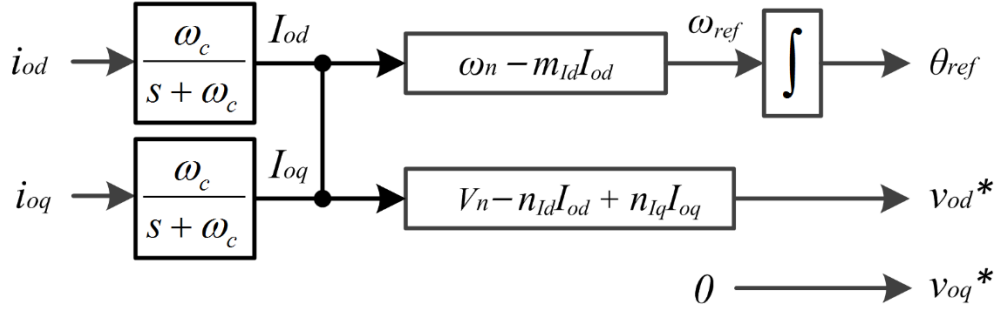


Fig. 4.2. A block diagram of the proposed I_{dq} controller for the frequency-based ACVR incorporated in the current-based droop control.

Fig. 4.2 shows a block diagram of the proposed I_{dq} controller where the I_d - V controller reduces the output voltage of the IDER for the frequency-based ACVR in coordination with the current-based droop (i.e., I_d - ω and I_q - V) controllers for the active and reactive power sharing. Specifically, the proposed I_{dq} controller operates on the voltage-oriented dq -reference frame where v_{od} has only DC component and v_{oq} is set to zero. From (4.8) and (4.9), instantaneous powers p_{ins} and q_{ins} can then be expressed as:

$$p_{ins} = v_{od} \dot{i}_{od}, \quad (4.10)$$

$$q_{ins} = -v_{od} \dot{i}_{oq}. \quad (4.11)$$

As v_{od} is close to the rated value under normal operating conditions of the IDER, p_{ins} and q_{ins} can mainly be controlled based on i_{od} and i_{oq} , respectively. The conventional (i.e., P - ω and Q - V) droop controllers, shown in (4.3) and (4.4), can then be replaced by the dq -axis current-based droop controllers as:

$$\omega^* = \omega_n - m_{Id} I_{od}, \quad (4.12)$$

$$v_{od}^* = V_n + n_{Iq} I_{oq}, \quad (4.13)$$

$$v_{oq}^* = 0, \quad (4.14)$$

where I_{od} and I_{oq} are the low-pass-filtered values of i_{od} and i_{oq} , respectively, as shown in Fig. 4.2. In (4.12) and (4.13), m_{Id} and n_{Iq} are the corresponding droop coefficients. Compared to (4.3)–(4.5), the current-based droop controller (4.12)–(4.14) can respond faster to the variations in the load demand, mainly due to the shorter time delays in the measurement, which is beneficial to improving the stability of frequency and voltage of the MG [34].

For the integration with (4.12)–(4.14), the I_d - V controller for the proposed ACVR is implemented in the form of the droop controller as follows:

$$v_{od}^* = V_n - n_{Id} I_{od} + n_{Iq} I_{oq}, \quad (4.15)$$

where n_{Id} is the ACVR coefficient for the relationship between I_{od} and v_{od} . As the total load demand in the MG increases, the power outputs p_{ins} and, consequently, current output i_{od} of the IDERs, increase according to (4.12) for MG frequency regulation: i.e., to maintain the instantaneous balance of active power. This leads to a decrease in v_{od}^* (and v_{od}), as shown in (4.15), reducing the power consumption of the voltage-dependent loads and mitigating the increase in the total load demand. In other words, the IDERs participate in both proposed ACVR and active power sharing. Incorporation of the I_d - V controller into current-based droop controllers enables the individual IDERs to adjust their output voltages by the same amount in a fully decentralized manner, while monitoring the MG frequency, as discussed in Chapter 4.2.2.

ACVR can be achieved without communication between IDERs, because the frequency is a global signal in the MG. Moreover, the larger the increase in the load demand, the larger the reduction of the bus voltages that can be achieved, because the MG frequency deviation is proportional to the load demand variation for fixed

I_d - ω droop coefficients. Proposed ACVR provides MGs a virtual reserve with demand side management by load-voltage dependence of system loads. Thus, it helps to improve system reliability. Figs 4.3 shows the flow chart of proposed I_{dq} controller including power sharing and CVR.

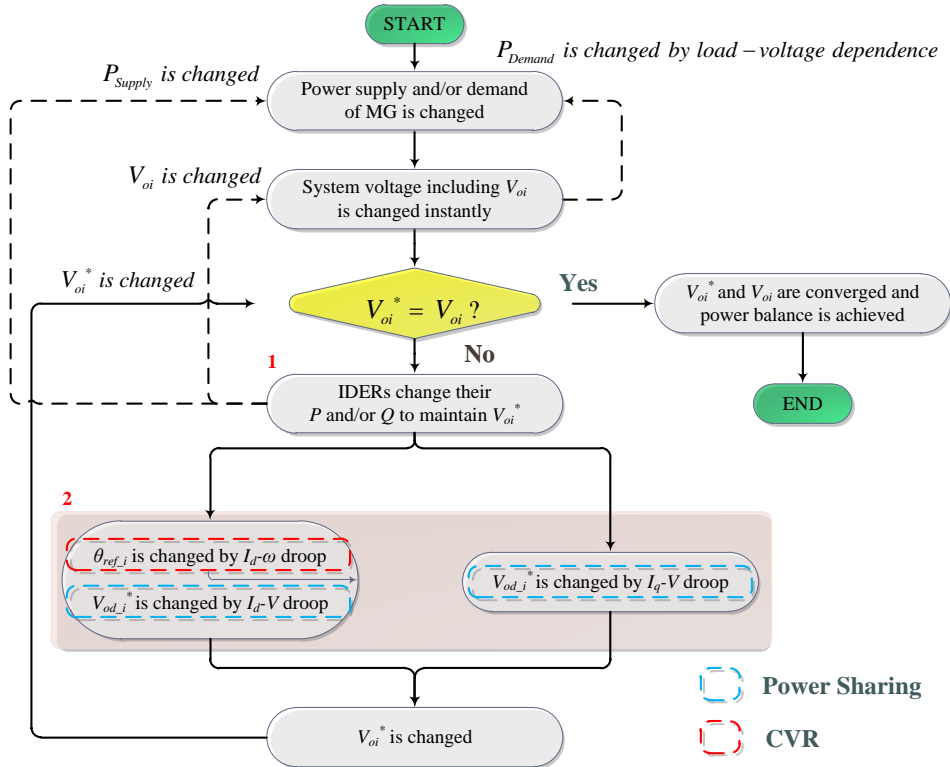


Fig. 4.3. Flow chart of the proposed I_{dq} controller for the power sharing and CVR.

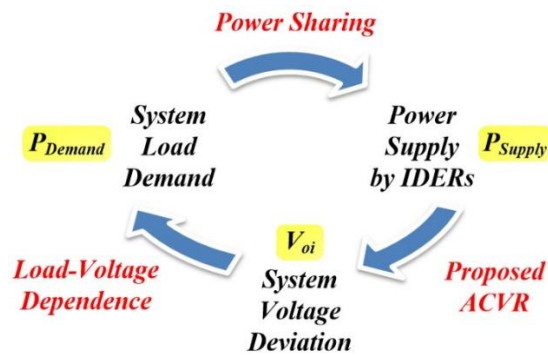


Fig. 4.4. Mechanism of the proposed I_{dq} controller.

As shown in Fig. 4.3, if power supply and/or demand changes and the power supply and demand of the MG system is momentarily imbalanced, the system voltage is changed instantly. In this case, there is a difference between the existing voltage reference value and the actual value, and IDERs change their active and reactive power output to maintain V_{oi}^* . In this process, the output voltage of the IDER is also changed, so that the load consumption is also changed by the load-voltage dependence. As a result, the proposed I_{dq} controller operates and outputs a new voltage and phase reference value (i.e., V_{oi}^* is changed). This process continues until the output voltage V_{oi} converges to the new voltage reference value V_{oi}^* . Briefly, the mechanism of the proposed I_{dq} controller is shown in Fig. 4.4.

4.2.2. Determination of droop coefficients for I_{dq} controller

Active and reactive droop coefficients

Similar to Chapter 3.1.3, the droop gain m_{Idi} for active power sharing between IDERs can be determined by dq -axis current and frequency as:

$$m_{Idi} = \frac{\alpha_i (\omega_n - \omega_{min})}{I_{odi.n}}, \quad (4.16)$$

where ω_n and ω_{min} are the nominal and minimum values of the angular frequency in the MG system, respectively. Moreover, $I_{odi.n}$ is the nominal d -axis current of a IDER and α_i is a constant for determining the I_d - ω droop coefficient of the IDER_{*i*}. For example, if α_i is set to 1, the system frequency in steady states becomes ω_{min} when the IDER_{*i*} outputs the rated d -axis current output. Typical value of α_i is determined within the ratio of maximum value to nominal value. As the m_{Idi} is increased by increasing α_i , the power sharing accuracy is increased instead of decreasing the frequency when the load is increased. Conversely, lowering the m_{Idi} deteriorates the power sharing accuracy, but lessens the frequency deviation. Therefore, the MG system operator should select an appropriate α_i considering such trade-off.

On the other hand, the reactive droop gain n_{Iqi} can be represented as:

$$n_{Iqi} = \frac{\beta_i (V_n - V_{min})}{I_{oqi.n}}, \quad (4.17)$$

where V_n and V_{min} are the nominal and minimum values of the voltage in the MG system, respectively. Moreover, $I_{oqi.n}$ denotes the nominal q -axis current of a IDER and β_i is a constant for determining the I_q - V droop coefficient of the IDER $_i$. Similarly, if β_i is set to 1, the bus voltage deviation by I_q - V droop in steady states becomes $V_n - V_{min}$ when the IDER $_i$ outputs the rated q -axis current output. However, the voltage deviation can be further varied by other voltage control equipment, the voltage deviation of adjacent bus, and line flow changes. Hence, considering the margin, the value of β_i is should be determined to be less than 1.

As the n_{Idi} is increased by increasing α_i , the power sharing accuracy is increased instead of decreasing the frequency when the load is increased. Conversely, lowering the m_{Idi} deteriorates the power sharing accuracy, but lessens the frequency deviation. Therefore, the MG system operator should select an appropriate α_i considering such trade-off.

ΔV_{ACVR} with respect to k_{ACVR} coefficients and n_{Id}

As described in Chapter 2.2.2, bus voltages in a microgrid should be operated within acceptable ranges (for example, 0.88-1.1 pu of the nominal value by IEEE 1547.2 Standard) under normal operating conditions. Given the local measurements and controllers, we adopted a simple and effective approach to determine n_{Id} in (4.15), so that the output voltages of the IDERs are reduced while maintaining the overall profile of the original bus voltages in the MG as shown in Fig 4.5. In other words, the output voltage drops of the IDERs with an increase in load demand are set equal to each other, as follows:

$$\Delta V_{ACVR} = -n_{Id1} I_{od1} = \dots = -n_{Idi} I_{odi} = \dots = -n_{Idn} I_{odn} . \quad (4.18)$$

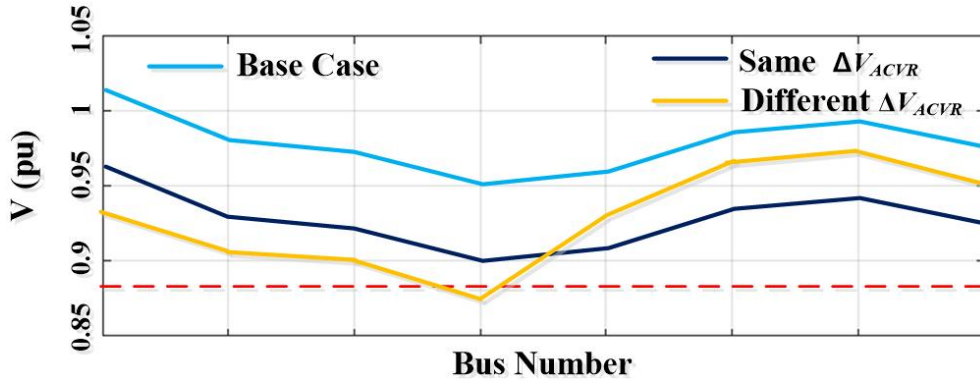


Fig. 4.5. Comparison of system voltage profiles for original and ACVR.

For all IDER_{*i*}, (4.18) can be satisfied by using the frequency deviation $\Delta\omega = \omega^* - \omega_n = -m_{Id} I_{od}$, that is, if the I_d - V droop coefficients n_{Idi} are set to be $k_{ACVR} m_{Idi}$, then (4.18) is satisfied for various I_d - ω droop coefficients and rated powers of IDERs in the MG system. It can be represented as:

$$\Delta V_{ACVR} = -n_{Idi} I_{odi} = k_{DCVR} \Delta\omega = -k_{ACVR} m_{Idi} I_{odi}, \quad \forall i, \quad (4.19)$$

where k_{ACVR} is defined as the ACVR coefficient related to the sensitivity of ΔV_{ACVR} to $\Delta\omega$.

Based on (4.10)–(4.16), (4.17) can be expressed equivalently as:

$$\Delta V_{ACVR} = k_{ACVR} \Delta\omega = -k_{ACVR} \frac{\Delta P_D}{\sum_{i=1}^n (v_{odi_ss} / m_{Idi})}, \quad (4.20)$$

where ΔP_D is the variation in the total load demand and v_{odi_ss} is the steady state value of v_{odi} .

This verifies that the individual IDERs can reduce their output voltages by the same amount, in proportion to the variation in the MG frequency or the net load demand, even in the general case where the IDERs have different droop constants, steady-state voltages, and power ratings. Note that the resulting output voltages of the IDERs are determined not only by ΔV_{ACVR} , but also by the I_q - V droop controller for the reactive power sharing. The voltage variation by the reactive droop control is determined by the time-varying reactive power demand of the MG.

Furthermore, the voltage in power system has local characteristics. That is, the voltage of each bus line varies with system conditions such as power flow and system topology; this introduces an uncertainty over the system voltage. Hence the appropriate droop coefficients should be determined considering voltage variations on other buses so that all the system voltages are maintained within the allowable range. The voltage deviation at n^{th} bus with uncertainty can be illustrated as Fig. 4.6. and can be represented as:

$$\Delta V_n = -n_{Idi}I_{odi} + n_{Iqi}I_{oqi} + \Delta V_{UNC.n} = \Delta V_{Idq} + \Delta V_{UNC.n} \quad (4.21)$$

where ΔV_n is the variation in voltage at n^{th} bus and $\Delta V_{UNC.n}$ is the voltage variation due to the uncertainty depending on various system conditions. (In [38], for a typical isolated microgrid, the voltage drop from generator buses to the feeder buses were around 1 to 2%) ΔV_{Idq} denotes the voltage variation by proposed I_{dq} controller.

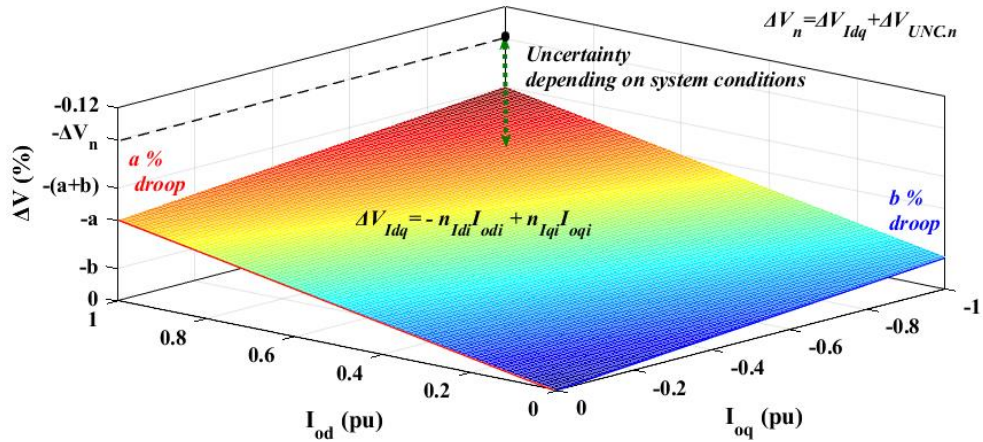


Fig. 4.6. Schematic diagram for voltage reduction at n^{th} bus.

With a similar approach in (4.16) and (4.17), the I_d - V droop coefficient n_{Idi} can be represented as:

$$n_{Idi} = \frac{\gamma_i(V_n - V_{min})}{I_{odi.n}}, \quad (4.22)$$

where γ is a constant for determining the I_d - V droop coefficient.

To determine an appropriate range of γ_i , it is necessary to take into account the voltage standard of the target system and the further voltage drop caused by I_q-V droop and the uncertainties. Moreover, with (4.16), the I_d-V droop coefficient n_{Idi} can be also represented as:

$$n_{Idi} = k_{ACVR} \frac{\alpha_i(\omega_n - \omega_{min})}{I_{odi.n}}, \quad (4.23)$$

Since all γ_i must satisfy the above condition (i.e., $n_{Idi} = k_{ACVR} \cdot m_{Idi}$) in (4.19), In order for (4.18) to be established for proposed ACVR, the value of k_{ACVR} is determined by the following equation in (4.22) and (4.23), as:

$$\gamma_i = \frac{k_{ACVR}(V_n - V_{min})}{\alpha_i(\omega_n - \omega_{min})}, \quad (4.24)$$

If k_{ACVR} is specified so that all of γ_i have a value within the proper range, it will be possible to maintain system voltage within the allowable range while performing ACVR. Furthermore, an adaptive approach to determining droop coefficients; m_{Id} , n_{Id} , n_{Iq} , and k_{ACVR} , in coordination with voltage-regulating devices will also be worth investigating in future research.

4.3 Comparative small-signal stability analysis for proposed I_{dq} controller

In this section, a complete small-signal state-space model of the study MG test bed system including inverters for DERs, lines, and loads is established to analyze the small-signal stability for the proposed ACVR strategy. The small-signal state-space modeling approach and derived entire system state matrices are represented in appendix A. The MG system state matrix \mathbf{A}_{MG} is used for small-signal stability analysis in following Chapter 4.3.1 and 4.3.2. The parameters for a normal operating condition with fixed load demand in MG test bed is shown in Table 4.1, that is the same as [13], [71]. Note that the droop coefficient n_{ld} for proposed ACVR is set to 5% at the rated current for the rated power of 10 kW and voltage of 380 V. Initial conditions for small-signal analysis also same as the values given in [13].

Table 4.1. Study system parameter for MG test bed.

Parameters	Values	Parameters	Values
f [Hz]	50	m_p [rad/s/W]	9.40e-5
L_f [mH]	1.35	n_Q [V/Var]	1.27e-3
R_f [Ω]	0.1	m_{ld} [V/A]	3.59e-2
C_f [μ F]	50	n_{ld} [V/A]	2.42e-1
L_c [mH]	0.35	n_{lq} [V/A]	7.26e-1
R_c [Ω]	0.03	K_{pv}	0.05
ω_c [rad/s]	31.41	K_{iv}	390
r_N [Ω]	1000	K_{pc}	10.5
F	0.75	K_{ic}	16e3

4.3.1. Root Loci of Eigenvalues

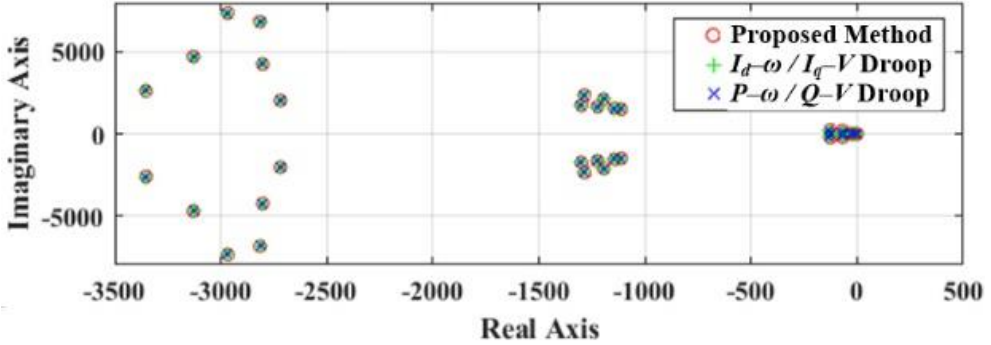


Fig. 4.7. Three eigenvalue clusters for the proposed ACVR, current-based droop control, and conventional droop control strategies.

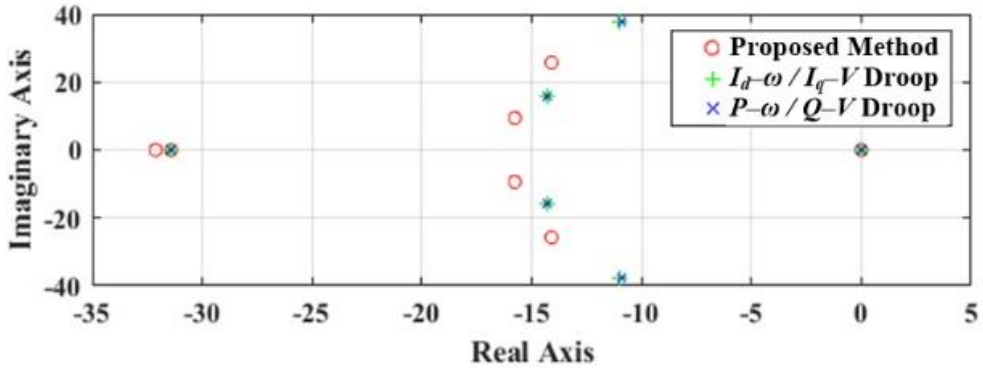


Fig. 4.8. Close-up plots in Fig. 4.7 for the critical eigenvalues in the rightmost cluster.

Fig. 4.7 shows the eigenvalues of \mathbf{A}_{MG} in Appendix A for the three different cases: the proposed ACVR, the current-based (i.e., $I_d-\omega$ and I_q-V) droop control, and the conventional (i.e., $P-\omega$ and $Q-V$) droop control, which are represented by red, green, and blue, respectively. It can be seen that the eigenvalues in the three clusters for the current-based droop control with the state variables of $[\Delta I_{odi}, \Delta I_{oqi}]$ are almost the same as those of the conventional droop control with $[\Delta P_i, \Delta Q_i]$. This demonstrates that (4.3)–(4.5) can be successfully replaced with (4.12)–(4.14), respectively, to take advantage of the reducing measurement time delay in practical applications.

In addition, Fig. 4.8 shows that for the proposed ACVR strategy, the eigenvalues in the rightmost cluster move to the left side, compared to those for the current- and power-based droop control strategies. This represents an increase in the system damping and, consequently, an improvement in the small-signal stability of the MG.

The comparisons shown in Fig. 4.8 indicate that the dominant poles in the rightmost cluster are sensitive primarily to the state variables $[\Delta I_{odi}, \Delta I_{oqi}]$ of the proposed I_{dq} controller (or, more accurately, \mathbf{C}_{Pv} in (A7), and hence the diagonal elements of \mathbf{A}_{MG} in (A78) in the Appendix A), as they are mainly affected by $[\Delta P_i, \Delta Q_i]$ in the case of conventional power controllers [13]. Meanwhile, the middle-cluster eigenvalues are sensitive to the state variables of the voltage and current controllers, and eigenvalues of the leftmost cluster are mainly influenced by the state variables of the inverter filters and the line currents. The proposed ACVR strategy marginally affects the eigenvalues in both clusters, ensuring the overall stability of the inverter-based islanded MG.

4.3.2. Eigenvalue sensitivity

Eigenvalue sensitivity for fixed I_d - V gain (5% and 10%)

Furthermore, for the proposed ACVR strategy, the root loci of the eigenvalues are analyzed in the case of variations in the I_d - ω and I_q - V droop coefficients (i.e., m_{Id} and n_{Iq}), while coefficient for the ACVR (i.e., n_{Id}) is fixed to 2.42×10^{-1} and 4.84×10^{-1} for 5% and 10% droop gains, respectively. The root loci are then compared to those for the conventional droop control, obtained for variations in m_P and n_Q , respectively.

Eigenvalue sensitivity for P - ω and I_d - ω droop gains

Fig. 4.9 shows the trajectories of the dominant poles (i.e., part of the low frequency cluster), as m_{Id} and m_P increase from 0.2% to 1% for the proposed and

conventional strategies, respectively. The eigenvalues move in the directions corresponding to increase in the absolute magnitudes of their imaginary values. This indicates that, as m_{Id} and m_P increase, the system damping is reduced in both strategies and, consequently, the IDERs become more responsive to variations in the MG frequency and voltage. In the conventional strategy, the eigenvalues move to the right, entering the unstable region (i.e., the right half-plane) for $m_P > 1.82 \times 10^{-4}$ as shown in Fig. 4.9.

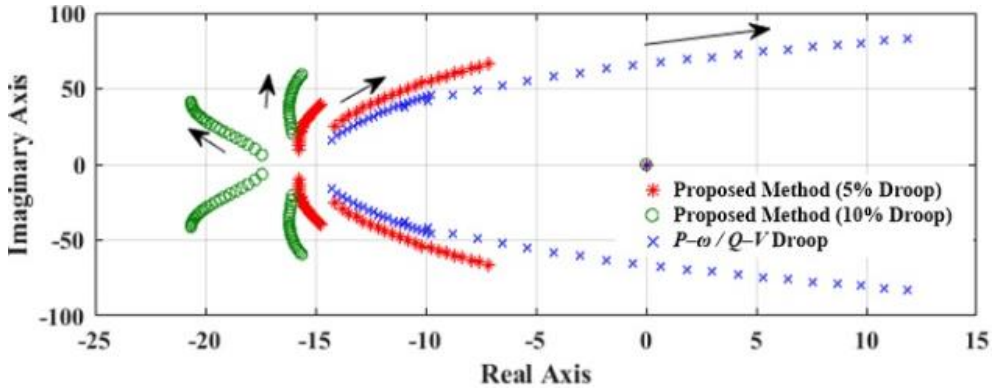


Fig. 4.9. Locus of eigenvalues as a function of m_{Id} and m_P for 0.2 % to 1 % droop ($2.39 \times 10^{-2} \leq m_{Id} \leq 1.20 \times 10^{-1}$ and $6.28 \times 10^{-5} \leq m_P \leq 3.14 \times 10^{-4}$).

On the contrary, the proposed strategy successfully mitigates the tendency of the MG to become unstable. In particular, for the case of the 10% I_d - V droop gain, a pair of complex conjugate poles only moves a little to the right, and another pair even move to the left. This implies that the proposed ACVR strategy is effective at stabilizing the MG operation, for example, when the power outputs of the IDERs happen to change abruptly due to large uncertainties in the frequency droop coefficients in practice.

Eigenvalue sensitivity for Q - V and I_q - V droop gain

Fig. 4.10 shows the root loci for an increase in n_{Iq} and n_Q from 1% to 11%. The real and complex-conjugate eigenvalues move to the right in both strategies.

Specifically, in the conventional strategy, a pair of complex-conjugate eigenvalues moves to the right, eventually entering the unstable region. The tendency is rather mitigated for the proposed one, as in the case shown in Fig. 4.10. The mitigation becomes more noticeable for $n_{ld} = 10\%$. This confirms that the proposed ACVR enables the MG to become more robust against uncertainties in the voltage droop coefficients. Note that for the proposed strategy, the eigenvalues close to the origin move slightly towards the imaginary axis in the beginning, then change direction to the left (see the close-up plot in Fig. 4.10).

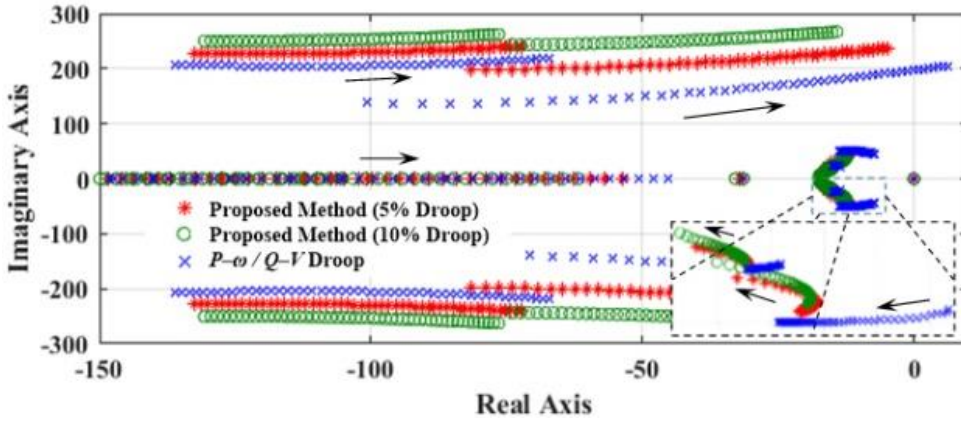


Fig. 4.10. Locus of eigenvalues as a function of n_{lq} and n_{l0} for 1% to 11% droop ($2.42 \times 10^{-1} \leq n_{lq} \leq 2.66$ and $6.35 \times 10^{-1} \leq n_{l0} \leq 7 \times 10^{-3}$).

Eigenvalue sensitivity for ω_c (cutoff frequency of LPF)

The cutoff frequency of LPF should be determined by taking into account the measurement delay of input signal, so it is able to indirectly express the time delay [72]. Fig. 4.11 shows the root loci for an increase in ω_c by 4% of original value (About 1.25 rad/s) per step. The eigenvalues move to the left in both cases; proposed method and current-based droop for power sharing only. Specifically, in the droop only case, a pair of complex-conjugate eigenvalues moves to the left until ω_c increased by 90% over the original value. The tendency is rather reduced for the proposed method, as in the case shown in Fig. 4.11. The value of maximum ω_c at

which the eigenvalues moves to the left are reduced by 136% of the original value. The tendency becomes more reduced for $n_{ld} = 10\%$ (116% of the original ω_c). This confirms that the proposed current-based droop enables the MG to respond more fast because the shorter measurement delay can increase the cutoff frequency. Note that for the proposed CVR, as the n_{ld} increases, the effect of increased the cutoff frequency is reduced. Therefore, this must be taken into account when designing controllers for practical applications.

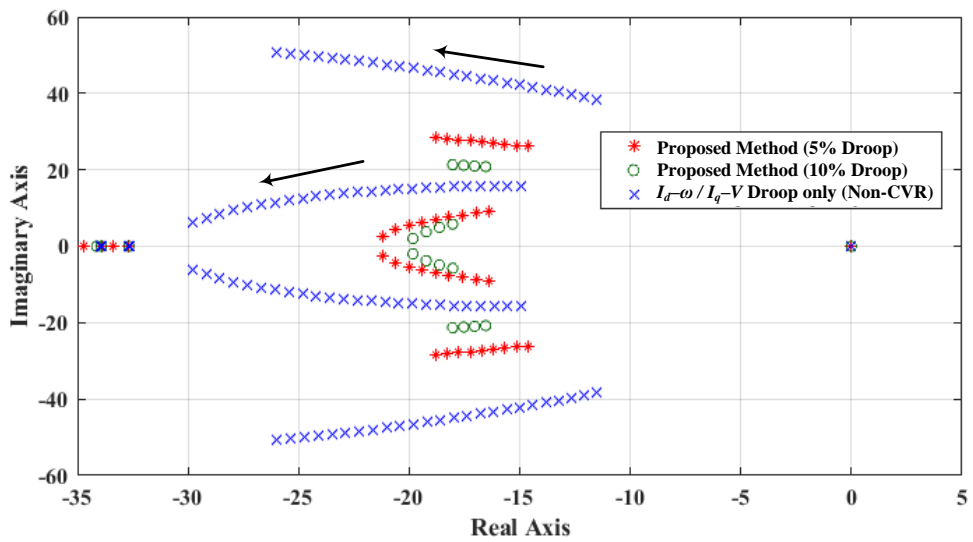


Fig. 4.11. Locus of eigenvalues as a function of ω_c (90%, 36%, and 16% increases from the original value, respectively. About 1.25 rad/s per step.).

Chapter 5. Case Studies and Simulation

Results

In this chapter, case studies are carried out to demonstrate the effectiveness of the Autonomous power management schemes developed in the chapters 3 and 4. The two test systems for case studies are modeled for SMO and MMO environment, respectively. The case studies for SMO and MMO were conducted using MATLAB/SIMULINK. The simulation model for SMO is the comprehensive model of Geocha Island in South Korea, based on real data obtained by KEPCO. On the other hand, the test model for MMO is 3-bus test MG system, which is also used in Chapter 4.3 and [13], [71].

5.1 Case studies for single-master operation

Fig. 5.1 shows a schematic diagram of the MG configuration. The upper and lower parts represent the distribution lines in the west and east islands, respectively. The Geocha MG system includes a 250-kW, 500-kWh BESS, a 100-kW PV, a 100-kW WT, and three 150-kW diesel generators. Moreover, additional BESS having 125-kW, 300-kWh of rating, will be installed to replace conventional diesel generators [76].

In Geocha island isolated MG, EMS, which is developed by KEPCO, has been implemented to monitor the real-time operation of the DERs and control in a centralized manner. Specifically, the PV and WT operate using MPPT algorithms to maximize their power outputs for variations in solar insolation and wind speed, respectively [77], [78]. In addition to the PV and WT, the diesel generators supply power as a grid-feeding unit to meet the load demand and maintain the SOC levels of the BESS within an acceptable range. In this dissertation, only one diesel generator is considered for simplicity.

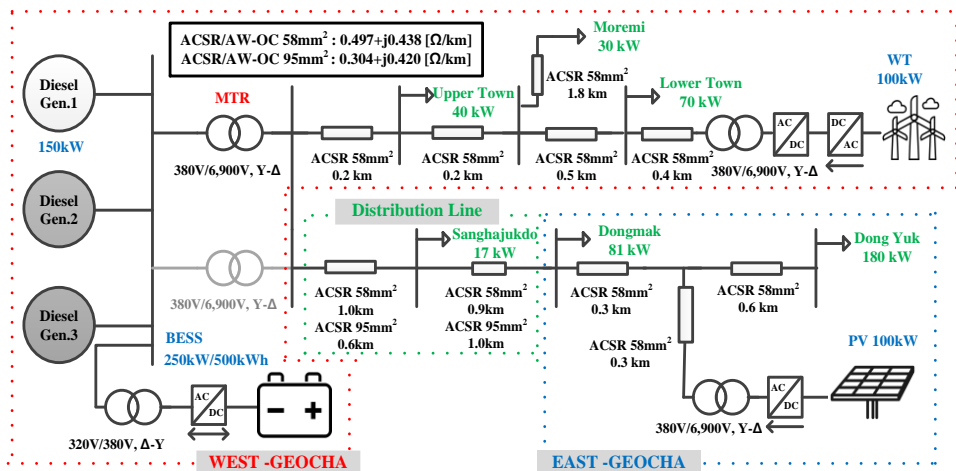


Fig. 5.1 Schematic diagram of Geocha Island MG.

5.1.1. Simulation model of case studies for single-master operation

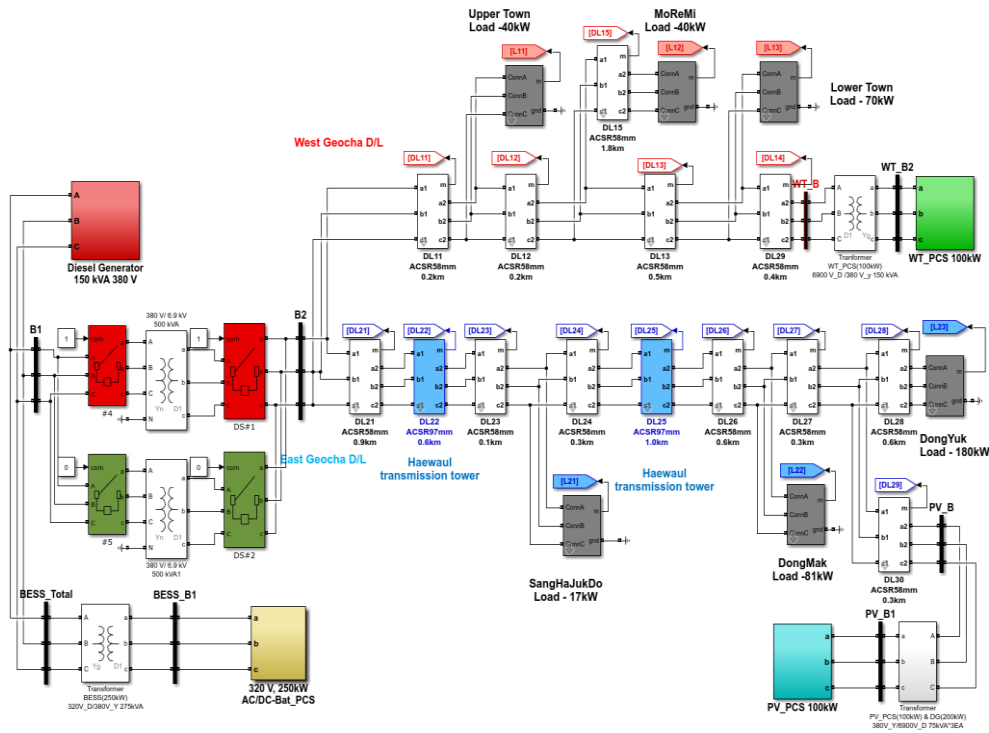


Fig. 5.2. Simulation model of Geocha Island MG using MATLAB/Simulink software environment.

Geocha island MG has been modeled based on the real parameters from KEPCO. The line type and parameters are shown in Fig 5.1. Case studies have been performed using the model of the isolated MG on Geocha Island. As shown in Fig. 5.2, the Geocha island MG model has been implemented using MATLAB/Simulink with the parameters listed in Table 5.1. The parameters with related to synchronous machine controller is shown in Table 5.2. the parameters of synchronous machine model are shown in Table 5.3.

For simplicity, it was assumed in the case studies that the power factors of all loads are maintained at unity and a single generator is assumed to participate in the real-time frequency regulation.

Table 5.1. Parameters used for the simulation model of the isolated MG on Geocha Island.

Parameter name	Symbols	Values	Units
Rated voltage of the system	V_{nom}	1	pu
System nominal frequency	f_{nom}	60	Hz
Minimum reference frequency	f_{min}	59.4	Hz
Dead-band of the VFPC of the BESS	-	± 0.01	
Rate limit of the reference frequency	-	0.3	Per Sec.
V - f proportional gain	K_v	6	-
Maximum limit of d-axis current in the BESS	$I_{d,max}$	1	pu
d-axis voltage reference of the BESS	V_d^*	1	pu
q-axis voltage reference of the BESS	V_q^*	0	pu
Sample time of the simulation	T_s	5e-5	sec

Table 5.2. Parameters of controller for diesel generator in Geocha Island.

Parameters	Symbols	Values	Units
Time constant of diesel engine	T_d	0.5	s
Time constant of valve actuator	T_v	0.05	s
P - f droop coefficients of the diesel generator	K_p	4.0e-6	-
Amplification gain of the exciter	K_e	70	-
Time constant of the exciter	τ_e	2.0e-3	-
Q - V droop coefficient of the diesel generator	K_q	2.5e-6	-
P gain of PI controller for active power control	K_{pp}	20	-
I gain of PI controller for active power control	K_{ip}	60	-
P gain of PI controller for reactive power control	K_{pq}	5	-
I gain of PI controller for reactive power control	K_{iq}	13	-

Table 5.3. Parameters diesel generator in Geocha Island.

Parameters	Symbols	Values	Units
Inertia coefficient	J	3.35	kg.m ²
Friction factor	F	0	N.m.s
Pole pairs	p	2	-
Stator resistance per phase	R_s	1.66e-2	Ohm
Stator leakage inductance	L_l	1.68e-4	H
d -axis magnetizing inductance viewed from stator	L_{md}	5.86e-3	H
q -axis magnetizing inductance viewed from stator	L_{mq}	5.05e-3	H
Field resistance	R_f	5.25e-3	Ohm
Field leakage inductance	L_{lfd}	6.82e-4	H
d -axis resistance of Damper	R_{kd}	1.53e-1	Ohm
d -axis leakage inductance of Damper	L_{lkd}	3.40e-3	H
q -axis resistance of Damper	R_{kq}	4.06e-2	H
q -axis leakage inductance of Damper	L_{lkq}	6.08e-4	H
P gain of PI controller for active power control	K_{pp}	20	-
I gain of PI controller for active power control	K_{ip}	60	-
P gain of PI controller for reactive power control	K_{pq}	5	-
I gain of PI controller for reactive power control	K_{iq}	13	-

The wind speed is assumed to change continuously from 11 m/s to 14 m/s. The proposed control scheme has been implemented in the MG for primary active power sharing under the condition where the low voltages occur due to an increase in the load demand. The proposed autonomous power management for single master operation can be similarly tested under the high voltage condition. The MG system is assumed to experience three successive events:

- (i) the 180-kW load is connected at the Dongyuk bus of the East Geocha distribution feeder at $t = 3$ s

- (ii) the WT at the end bus of the West-Geocha feeder is tripped at $t = 6$ s,
- (iii) the PV system on the East-Geocha island feeder is tripped at $t = 9$ s.

At $t = 0$ s, the total load demand and the power outputs of the PV system and diesel generator are set to 238-kW, 90-kW, and 100-kW, respectively. The reactive power output of the diesel generator is set to 10-kvar, and the reactive power reference of PV and WT are set to 0.

5.1.2. Simulation results for single-master operation

Cases 1 and 2: Simulation results with conventional and proposed method

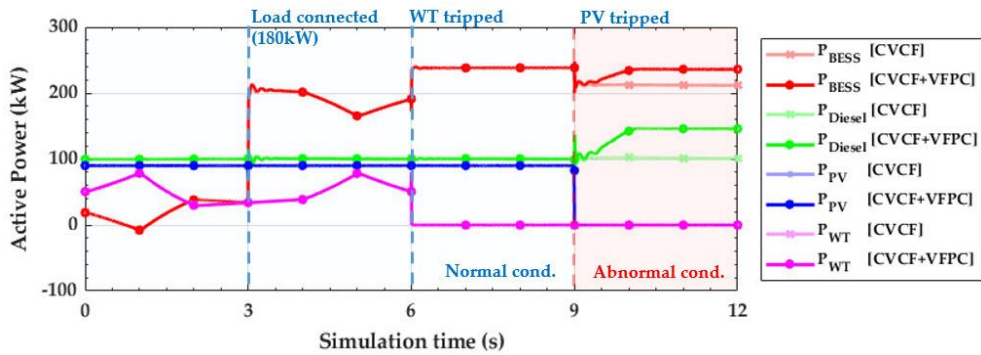


Fig. 5.3. Profiles of the active power outputs of the BESS, WT, PV, and diesel generator.

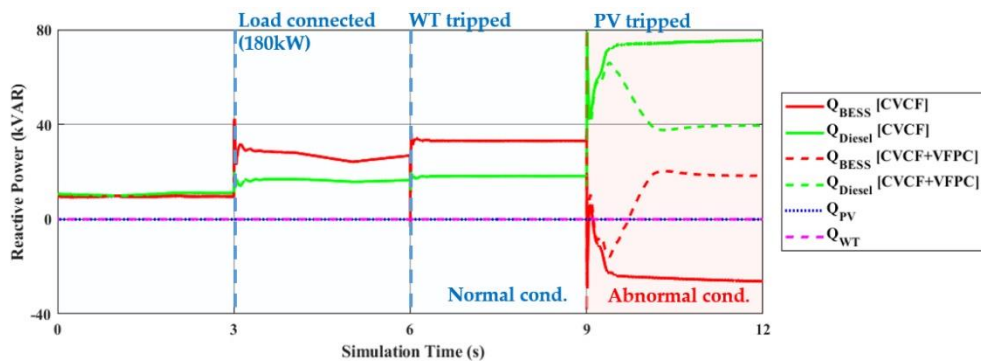


Fig. 5.4. The reactive power profiles of the BESS, WT, PV, and diesel generator.

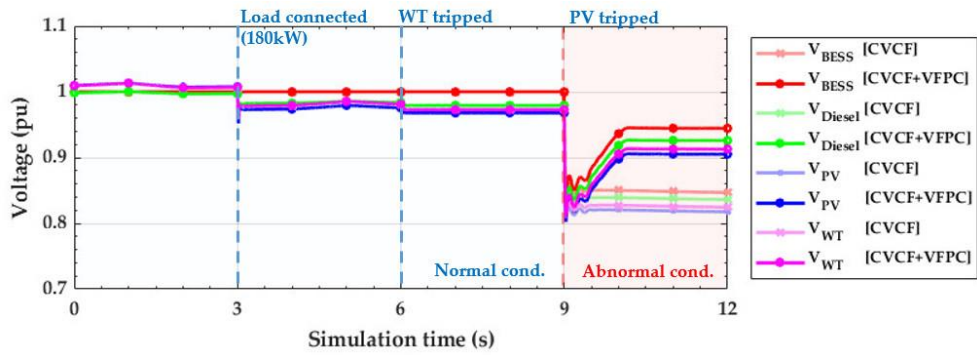


Fig. 5.5. Profiles of the input voltages of the BESS, WT, PV, and diesel generator.

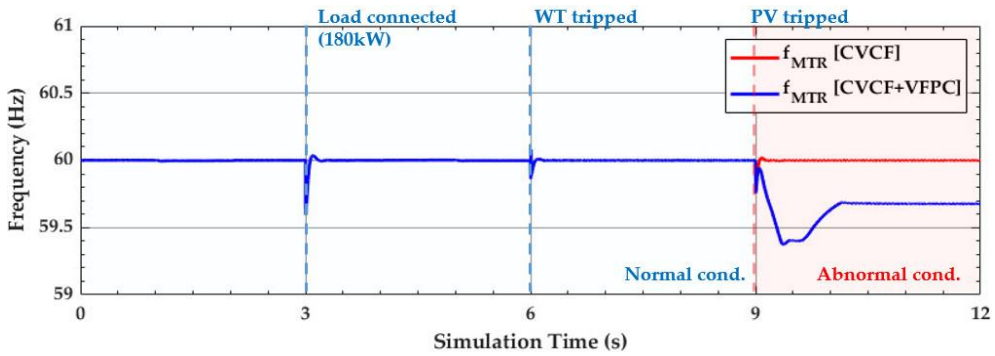


Fig. 5.6. Comparison of the grid frequency profiles in the Geocha MG.

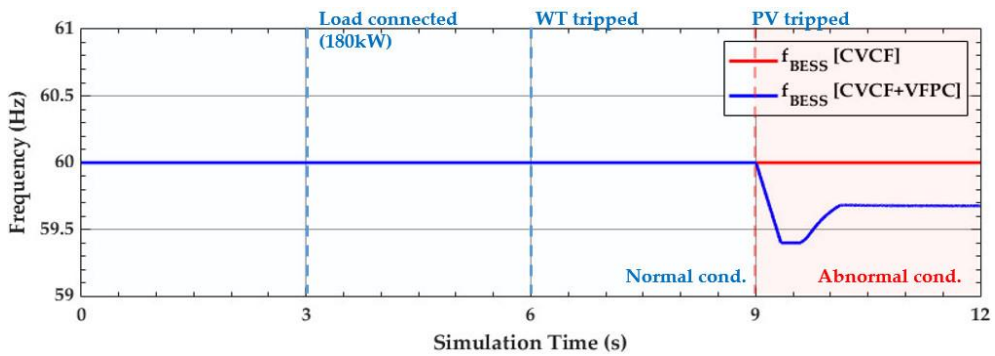


Fig. 5.7. Comparison of the reference frequency profiles of the BESS in the Geocha MG.

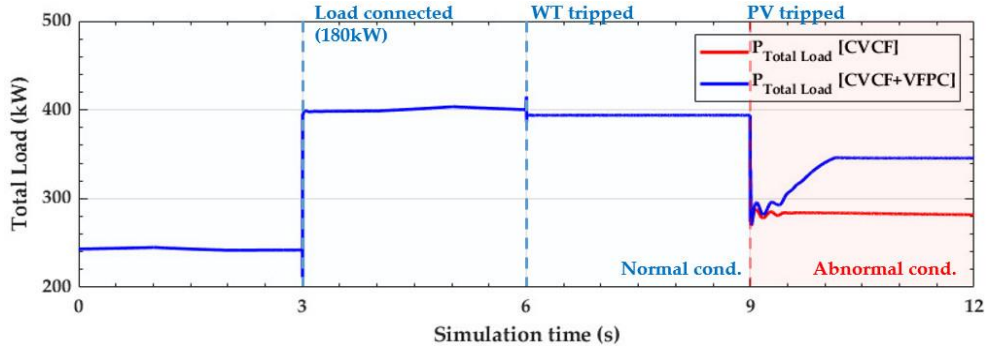


Fig. 5.8. Comparison of the total load demand profiles in the Geocha MG.

Simulation results under the normal conditions ($t < 9$ s)

Fig. 5.3 shows the active power profiles of the grid-forming BESS, WT, PV, and diesel generator for Cases 1 and 2, respectively: (Case 1) where only the conventional CVCF controller was adopted; (Case 2) where the proposed VFPC was integrated with the CVCF controller. The proposed VFPC was not activated by its limiter (see Fig. 3.6) under the normal condition where the active power imbalance can be compensated for by the BESS. Therefore, Cases 1 and 2 have the same profiles of the active powers, voltages, frequencies, and load demand until $t < 9$ s, as shown in Figs. 5.3 to 5.8. In both cases, the BESS maintained the active power balance and, consequently, the V_{BESS} and f_{BESS} at the rated values in the Geocha MG during $0 \text{ s} \leq t \leq 9 \text{ s}$.

Specifically, during $0 \text{ s} \leq t \leq 3 \text{ s}$, the bus voltages at the WT and PV system increased to levels slightly higher than 1 pu. The voltages at the BESS were well maintained at almost 1 pu, as shown in Fig. 5.5. Figs. 5.4 and 5.6 to 5.8 compare the profiles of the reactive power outputs, the system frequency at the main transformer, the reference frequency of the BESS, and the total load demand in the MG for Cases 1 and 2. As shown in Fig. 5.8, the actual load demand was observed at approximately 243 kW, which was greater than rated load demand 238 kW at the rated bus voltages; the voltages at several load buses were higher than 1 pu, increasing the load demand due to the load-voltage dependency, as shown in (3.4). In Fig. 5.4, the reactive power

outputs of the BESS and the diesel generator were maintained at an almost constant level due to the small variations in the reactive power loss and the feeder voltage.

When the 180-kW load was connected to the Dong-Yuk bus of the MG at $t = 3$ s, the nominal load demand increased from 238 kW to 418 kW in total. The MG voltage and frequency were then reduced instantaneously due to the large step increase in the load demand. The CVCF controller detected the voltage reduction and adjusted the output power of the BESS quickly from 34 kW to 213 kW, so as to maintain the power balance and the input voltage at the rated value. Meanwhile, the active power of the diesel generator fluctuated due to the frequency deviation during a short period of time.

Fig. 5.3 shows that the CVCF controller enabled the battery to respond to a large step-wise increase in the load demand within a short time period and maintain the real-time power balance in the MG. As shown in Fig. 5.5, the small voltage drops were detected for the WT, PV system, and the diesel generator because of the increase in the power flowing along the distribution feeders connected from the west island to the east island. This increased active and reactive power losses on the substation transformers and in the distribution lines. The reactive power output of the BESS increased due to the increase in the reactive power loss in the MG, and the diesel generator then increased its reactive power output via the $Q-V$ droop controller. During the period of $3 \text{ s} \leq t \leq 6 \text{ s}$, as shown in Fig. 5.8, the actual load demand increased about from 398 kW to 403 kW and the bus voltage was increased about from 0.967 pu to 0.986 pu.

At $t = 6$ s, the WT was tripped from the distribution feeder. The active power of the BESS then increased to maintain the power balance via the CVCF control, causing a further drop in the voltage at the buses of other DERs owing to the increase in the power flow from the substation. The total load demand then decreased owing to the additional voltage drops at the load buses.

Meanwhile, other DERs retain their active power because the BESS was solely responsible for maintaining the active power balance at the primary control level.

The active power output of the BESS increased from 190 kW to approximately 238 kW, as shown in Fig. 5.3, which is similar to the rated active power output of 250 kW. The power balance of the MG could be achieved within a short period of time. However, the primary active power reserve was significantly reduced in the MG, affecting the power system reliability. The reactive power outputs of the BESS and the diesel generator slightly increased for the same reason as aforementioned.

Simulation results under the abnormal conditions ($t > 9$ s)

When the PV system was tripped at $t = 9$ s, the active power reserve of the BESS could not afford the power balance. As a result, the bus voltages and hence the load demand decreased significantly, as shown in Figs. 5.5 and 5.8. In the CVCF-only case, the diesel generator maintained its active power output as constants, because the MG frequency was maintained at f_{set} and the diesel generator could not detect the power imbalance with only its local measurement, as shown in Figs. 5.3, 5.6 and 5.7. Consequently, the total load demand was significantly reduced to 281.9 kW, which is about 67% of the nominal demand, owing to the severe voltage reductions beyond the lower voltage limit of 0.9 pu: i.e., $V_{aBESS} = 0.847$ pu, $V_{aDiesel} = 0.836$ pu, $V_{aWT} = 0.824$ pu, and $V_{aPV} = 0.817$, as shown in Fig. 5.8.

Moreover, the reduction of the bus voltage at which the BESS is located also affected the active power output of the BESS, as shown in (3.7). This is illustrated in Fig. 5.3 where the active power output of the BESS is about 211.7 kW; it is lower than the rated active power. This further decreased the bus voltage. The large reduction of the feeder voltage caused the excessive compensation of the Q - V droop controller for the reactive power. Since the BESS is located close to the diesel generator in the remote MG, the excessive compensation could be immediately balanced using the BESS. It can be seen that the total reactive power supply and the reactive power loss increased mainly because of a further increase in the power flowing from the west island to the east island.

In contrast, the reference frequency of the BESS was reduced to 59.4 Hz due to

the voltage drop (as shown in Fig. 5.8) for Case 2 where the proposed VFPC was applied to the CVCF control in the BESS. The system frequency was then reduced to 59.37 Hz and the diesel generator increased the active power to 146.1 kW via the droop control. The active power output of the BESS was also increased to 236.1 kW, as shown in (3.7), enabling the further recovery of the voltage drop. This coordinated control between the BESS and the diesel generator caused the bus voltages to rise by acquiring additional primary active power reserve in the MG system. The compensation of the diesel generator for the reactive power was mitigated as the feeder voltage was gradually recovered. The system frequency measured by a PLL was gradually restored to 59.68 Hz by increased power outputs of the diesel generator and the BESS. As shown in Figs. 5.5 and 5.8, the proposed VFPC successfully mitigated the voltage drop ($V_{aBESS} = 0.944$ pu, $V_{aDiesel} = 0.926$ pu, $V_{aWT} = 0.913$ pu, and $V_{aPV} = 0.905$ pu) and the load reduction (about 72 kW, about 17% of the nominal demand).

Cases 3 and 4: Simulation results with less voltage-dependent loads

In Case 3, the constant current load with the rated power of 81-kW was taken into consideration at the Dong-Mak bus (see Fig. 5.1); n_p was reduced to approximately 1.65 at $t = 0$ s. After the constant impedance load of 180-kW was connected at the Dong-Yuk bus at $t = 3$ s, n_p increased from 1.65 to 1.81. The power shortage then led to larger decreases in the feeder voltages and consequently in the system frequency during $t \geq 9$ s, compared to the original condition (i.e., Case 2) where only the constant impedance loads were considered. Figs. 5.9 to 5.12 and Table 5.4 show that the lower n_p , the lower active power output of the BESS, further reducing the bus voltage, the frequency, and actual total load demand, particularly when the diesel generator failed to completely follow the command of the master BESS owing to the insufficient reserve capacity. In Figs 5.9 to 5.12, the full and dotted lines represent the cases of $n_p = 2$ and 1.56, respectively.

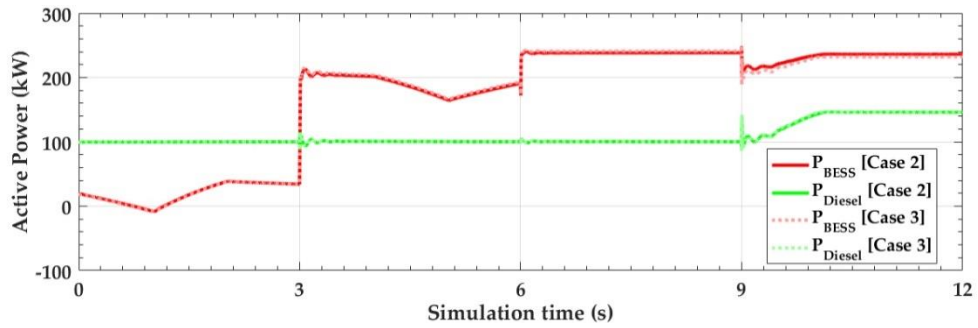


Fig. 5.9. Active power profiles of the BESS and diesel generator in Cases 2 and 3.

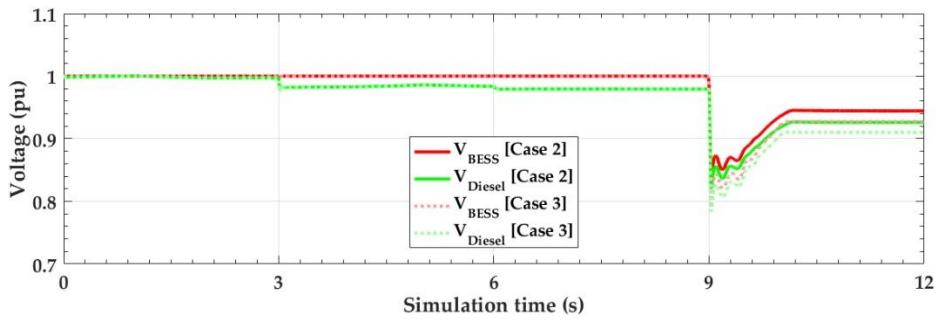


Fig. 5.10. Profiles of the input voltages of the BESS and diesel generator in Cases 2 and 3.

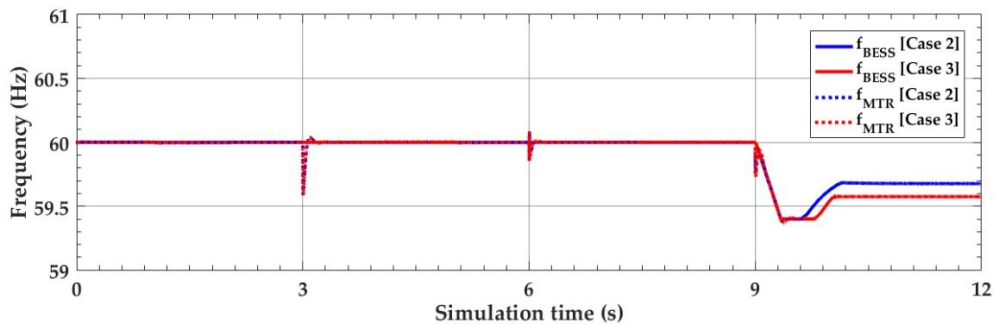


Fig. 5.11. Comparisons of the frequency profiles at the main transformer and BESS in Cases 2 and 3.

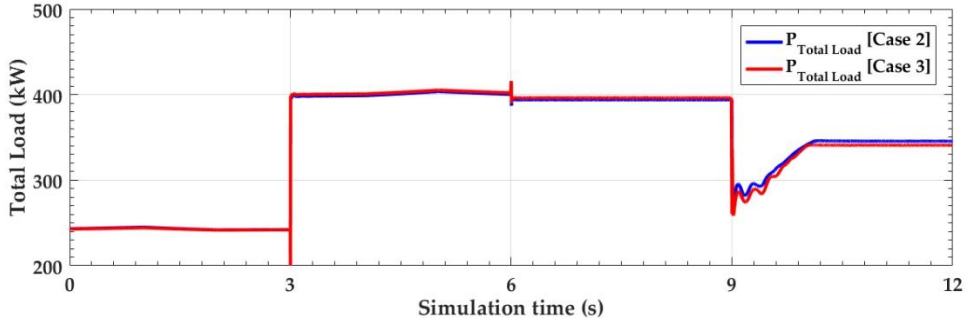


Fig. 5.12. Comparisons of the total load demand profiles in the Geocha MG.

Table 5.4. Comparisons between the simulation results acquired for different load demand and compositions at $t = 12$ s.

	n_p	P_{load_0} (kW)	V_{aBESS} (pu)	$V_{aDiesel}$ (pu)	P_{BESS} (kW)	P_{Diesel} (kW)	P_{load} (kW)	f_{MTR} (Hz)
Case 2	2	418	0.944	0.926	236.1	146.1	345.6	59.68
Case 3	1.81	418	0.927	0.910	231.8	146.1	340.8	59.58
Case 2*	2	388	0.975	0.955	243.8	135.4	343.7	59.86
Case 4	1.56	388	0.969	0.949	242.3	143.7	350	59.83

In Cases 2* and 4, to simulate the less severe power shortage condition, the original condition was slightly modified to reduce Dong-Mak load from 81-kW to 51-kW. In addition, in Case 4, the 51-kW Dong-Mak load and the 40-kW Upper-Town load were modeled as constant power loads, reducing equivalent n_p of the MG to approximately 1.24 at $t = 0$ s. After the constant impedance load of 180-kW was connected at the Dong-Yuk bus at $t = 3$ s, increasing n_p from about 1.24 to 1.56. The power shortage occurred at $t = 9$ s in the MG, resulting in $n_p = 1.56$. It led to the bigger drop in the voltage and, consequently, caused the larger decrease in the frequency, in comparison to Case 2*. The maximum variation in the power output of the BESS was also reduced owing to the voltage drop by (3.2). The diesel generator measured the frequency, which was further reduced, and increased its output power

larger than those in Case 2*. This allowed the power shortage to be better compensated for and, consequently, the system voltages and total load demand in the MG to be more recovered.

Figs. 5.13 to 5.16 then show that the lower n_p , the higher active power supply when the diesel generators had the sufficient reserve capacities and succeeded in following completely the command of the master BESS. This mitigated the reduction of actual load demand. Note the full and dotted lines represent the cases of $n_p = 2$ and 1.56, respectively. Table 5.4 shows that although the bus voltage, system frequency, and BESS power output were reduced at $t = 12$ s for $n_p = 1.56$, the output power of the diesel generator and the total load demand were higher in Case 4 than those in Case 2*.

As shown in Cases 2-3 and 2*-4, the voltage drop becomes larger as n_p is reduced, particularly, under the power shortage condition. This implies that the proposed controller is more effective in alleviating the power shortage problem and voltage stability issue for a remote MG with less voltage-dependent load. The effect of the proposed controller becomes more evident when the slave units have sufficient reserve capacities.

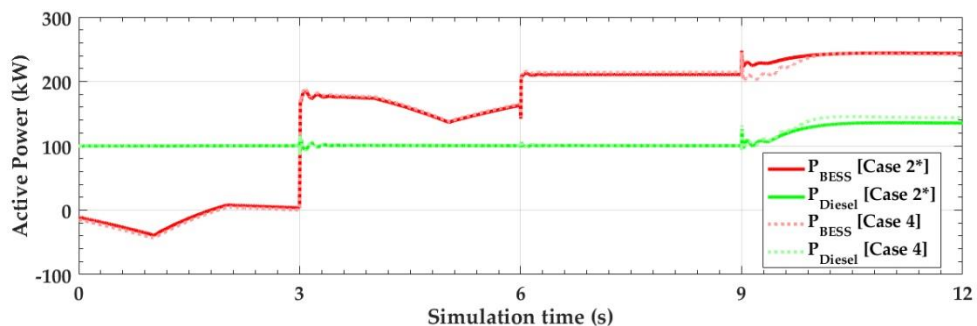


Fig. 5.13. Profiles of the active power outputs of the BESS and diesel generator in Cases 2* and 4.

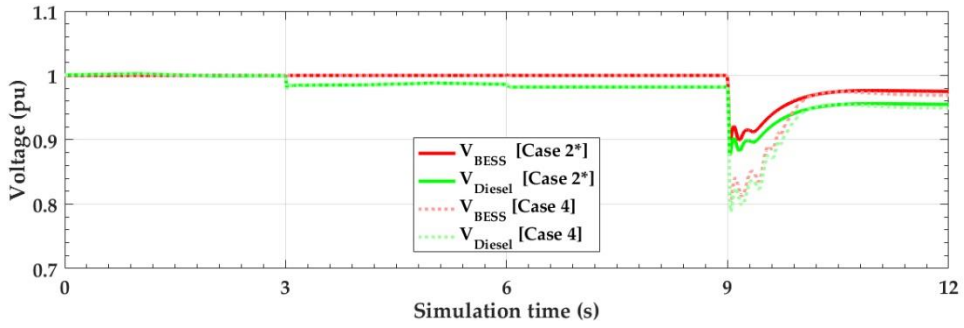


Fig. 5.14. Profiles of the input voltages of the BESS and diesel generator in Cases 2* and 4.

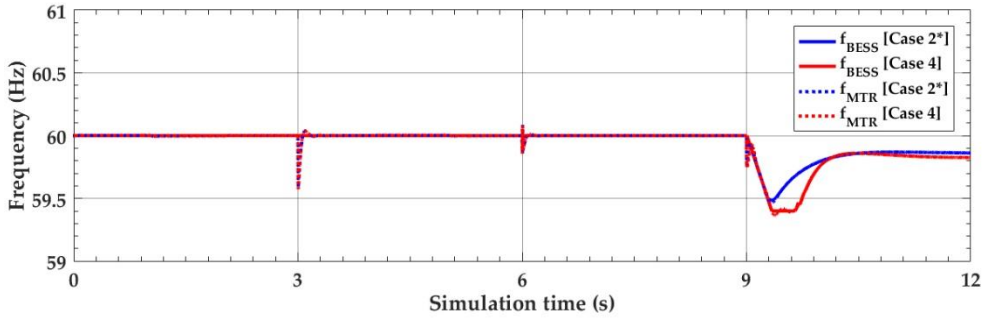


Fig. 5.15. Comparisons of the frequency profiles at the main transformer and BESS in Cases 2* and 4.

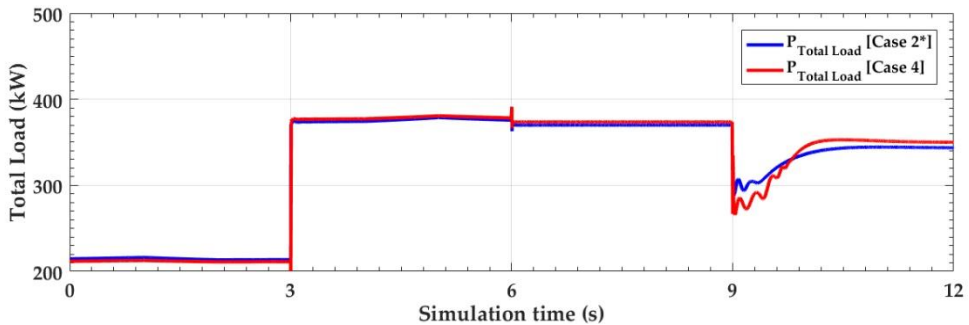


Fig. 5.16. Comparisons of the total load demand profiles in Cases 2* and 4.

Discussion

The proposed VFPC operates only when the primary active power reserve of the MG is not enough by measuring the AC voltage of the BESS under the low-voltage condition. Under the normal condition (until $t = 9$ s in Chapter 5.1.2), the proposed method can be able to reduce the system frequency variation and the active power fluctuation, compared to the conventional P - f droop control method of the grid-forming BESS.

The simulation results in Chapter 5.1.2 show that when the primary active power reserve of the BESS is insufficient, and the load demand exceeds the power supply (after $t = 9$ s), the grid voltage is then greatly reduced overall, which reduces the load demand by the voltage-dependent characteristics of the loads. Furthermore, the active power reserve of the BESS is also reduced by the voltage drop at the BESS, exacerbating the active power imbalance in the MG. The summary of the results for Case 1 (Conventional CVCF) and Case 2 (CVCF + Proposed VFPC) at $t = 12$ is shown in Fig 5.17.

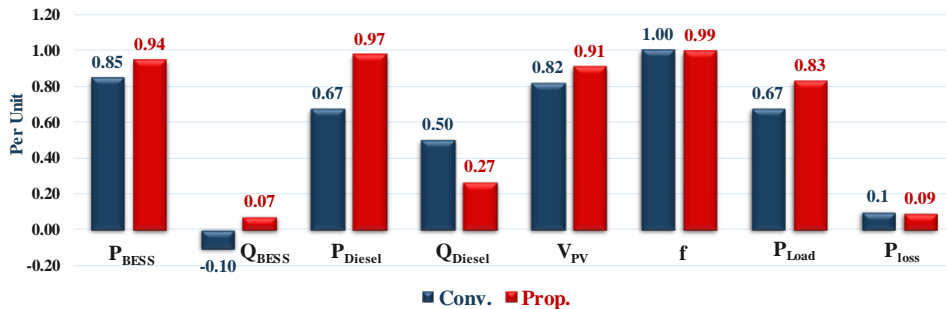


Fig. 5.17. Comparison of simulation results for Cases 1 (Navy) and 2 (Red) at $t = 12$ s.

Simulation results suggest that the conventional control methods of the grid-forming BESS cannot operate properly when a large change in active power, such as a generator trip and step-load change, instantaneously occurs in the MG. These changes induce an instantaneous voltage drop, which reduces the maximum active

power output of the grid-forming BESS. In this case, the conventional P - f droop controller receives the reduced active power of the BESS due to the voltage drop as an input signal, outputting the less reduced frequency. Then other DGs using f - P droop controllers cannot increase their active power outputs enough due to the frequency not being sufficiently reduced in the transient state.

It needs to be noted that in practice, it is likely for the system operator to limit the reactive power supply to ensure the stable operation of the MG without significantly affecting the overall performance of the proposed active power management. In addition, due to the independent control of active and reactive power, the proposed method does not prevent the normal operation of the conventional reactive power controllers, mitigating the excessive compensation even for the case where the active power reserve is not sufficient.

5.2 Case studies for multi-master operation

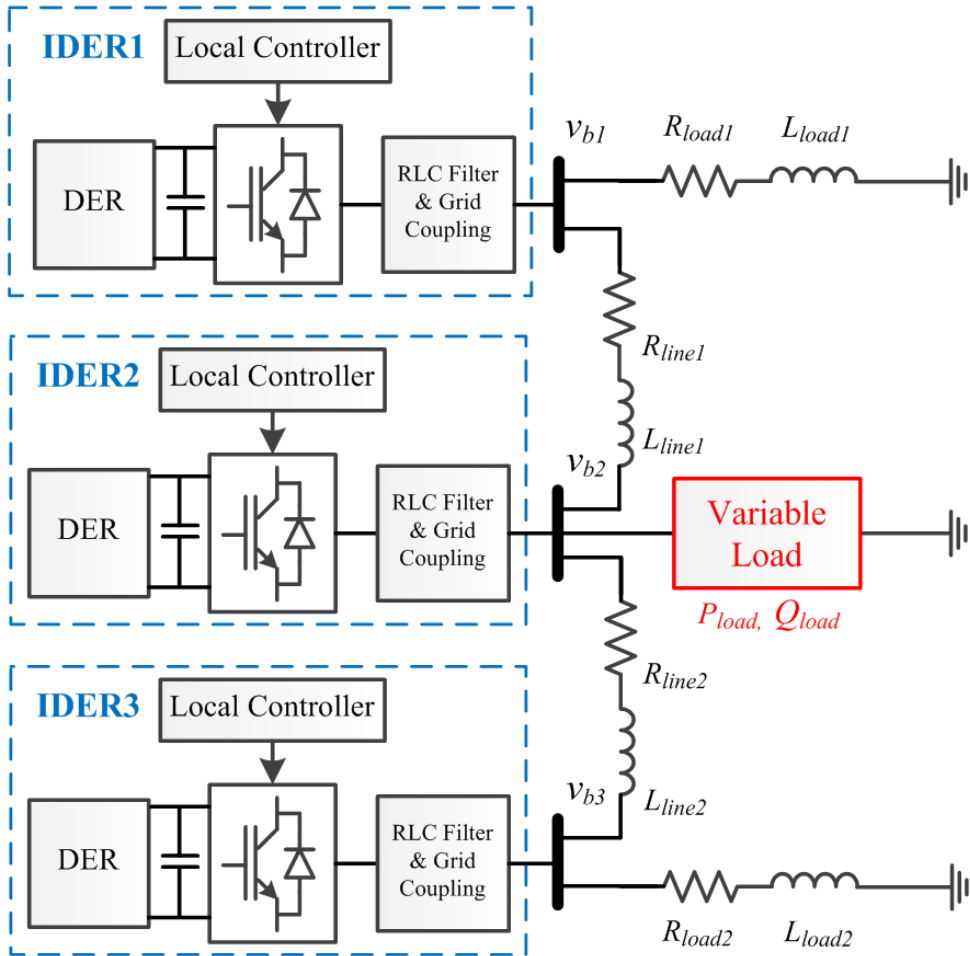


Fig. 5.18. An islanded MG including IDERs and voltage-dependent loads.

In this dissertation, a three-bus inverter-based islanded MG [13], [71] is considered as a test bed to develop and analyze the proposed ACVR strategy with MMO by IDERs, as shown in Fig. 5.18. Specifically, the MG includes three IDERs, each of which is equipped with a local controller and acts as a grid-support grid-forming unit as described in Chapter 2.1. In other words, the IDERs determine the MG frequency and voltages in a multi-master approach while maintaining the real-time balance between generation and load demand. The MG also contains the variable load that operates as a grid-following unit: i.e., its input power is adjusted

according to bus voltage v_{b2} . Similarly, the power inputs of two constant- impedance loads vary depending on bus voltages v_{b1} and v_{b3} .

The MG test bed, shown in Fig. 5.18, was implemented using MATLAB/SIMULINK to analyze the real-time performance of the proposed ACVR strategy with variation in the load demand, compared to the conventional $P-\omega$ and $Q-V$ droop control (i.e., non-CVR) strategy. The variable load was modelled using (4.1) and (4.2) to analyze the effects of the power factors and voltage exponents on ACVR performance. The Load impedances and line parameters for MG test bed modeling are shown in Table 5.5.

Table 5.5. Load impedances and line parameters in the MG test bed.

Parameters	Values	Parameters	Values
R_{load1}	25 Ω	L_{load1}	10 nH
R_{load2}	20 Ω	L_{load2}	10 nH
R_{line1}	0.23 Ω	L_{line1}	0.3 mH
R_{line2}	0.35 Ω	L_{line2}	1.8 mH

For simplicity, the IDERs were modelled using three-phase ideal voltage sources, considering the fast dynamic response of the VSI. In (4.15), n_{ld} and V_n were set to 5% and 1 pu, respectively. The other parameters for the IDERs, lines, and loads remained the same as those used for the small-signal analysis in Chapter 4.3.

5.2.1. Performance validation of the proposed ACVR strategy

Fig. 5.19 shows the profiles of the active and reactive power outputs of the IDERs for stepwise increases in P_{Load} (by 6.55 kW every second); this is equivalent to 50% of the rated power of the constant-impedance loads at Buses 1 and 3. In other words, the variable load consumed 19.65 kW for $t \geq 3$ s, accounting for approximately 60% of the total load demand. The variable load operated with a unity

power factor and $n_p = 2$. Fig. 5.18 shows the corresponding frequency and voltage profiles measured at the output nodes of the IDERs.

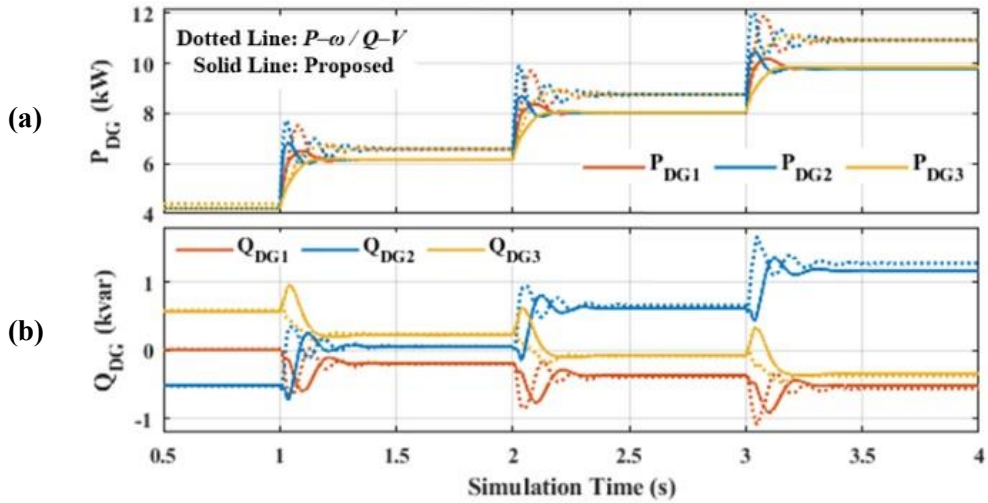


Fig. 5.19. (a) Active and (b) reactive power outputs of the IDERs for $n_{ld} = 5\%$.

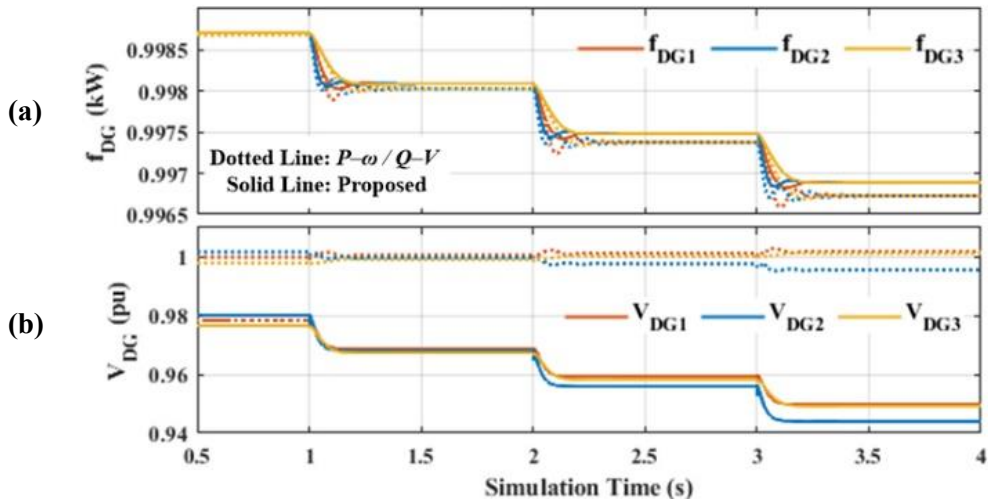


Fig. 5.20. (a) Frequency and (b) voltage profiles at the output nodes of the IDER.

Fig. 5.19 shows the profiles of the active and reactive power outputs of the IDERs for stepwise increases in P_{Load} (by 6.55 kW every second); this is equivalent to 50% of the rated power of the constant-impedance loads at buses 1 and 3. In other words, the variable load consumed 19.65 kW for $t \geq 3$ s, accounting for

approximately 60% of the total load demand. The variable load operated with a unity power factor and $n_p = 2$. Fig. 5.20 shows the corresponding frequency and voltage profiles measured at the output nodes of the IDERs.

Specifically, Fig. 5.19(a) shows that each IDER generated $P_{DG} = 4$ kW (or, equivalently, 40% of $P_{DG, rated} = 10$ kW) during $0.5 \text{ s} \leq t \leq 1 \text{ s}$. In the proposed ACVR strategy, the I_d - V controller with $n_{Id} = 5\%$ led to decreases in the V_{DG} of the IDERs by approximately 0.02 pu, as shown in Fig. 5.20(b). As P_{Load} increased during the period $1 \text{ s} \leq t \leq 4 \text{ s}$, i_{od} increased and f_{DG} then decreased in both strategies, as shown in Fig. 5.20(a); also, see (4.10) and (4.12).

On the contrary, the V_{DG} levels were only reduced in the proposed strategy, as shown in Fig. 5.20(b); compare (4.4) and (4.15). Fig. 5.18(a) shows that due to the voltage-dependent loads, the total load demand for the proposed strategy became lower than that for the conventional strategy. Therefore, f_{DG} deviated less during $1 \text{ s} \leq t \leq 4 \text{ s}$ in the proposed strategy than in the conventional strategy, as shown in Fig. 5.20(a).

Note that in Fig. 5.19(b), the I_q - V controllers were as effective as the Q - V controllers at reactive power sharing. This is due to the coupling between the line resistance and reactance, particularly in the case of the small-scale, low-voltage MG [31]. Fig. 5.20(b) shows that for the conventional strategy, V_{DGs} were barely reduced from 1 pu during $1 \text{ s} \leq t \leq 4 \text{ s}$, because the line power flows and reactive power loads were small. The small changes in V_{DG} were attributed to variations in the line power flows.

As the MG load demand increased, the output voltages of the IDERs decreased further, as shown in (4.20). Consequently, a larger decrease in the load demand occurred, as shown in Table 5.6. This confirms that the proposed strategy is effective for improving the reliability of MG operation by mitigating severe increases in the load demand or, equivalently, the lack of generation reserve capacity, as shown in Fig. 5.20. Moreover, the proposed CVR strategy improved the transient response of the IDERs, as shown in Table 5.6 and Fig 5.21. Specifically, the average percent

overshoot and settling time of $IDER_2$ were reduced by approximately 36.7% and 47.1%, respectively, compared to those in the conventional strategy. This is consistent with the results of the eigenvalue analysis, discussed in Chapter 4.3.

Table 5.6. Performance comparisons between the proposed ACVR and conventional droop control strategies.

	Settling time of $IDER_2$ (s)		Percent overshoot of $IDER_2$ (%)		Load reduction (%)		
	1-2 s	2-3 s	1-2 s	2-3 s	1-2 s	2-3 s	3-4 s
Time	1-2 s	2-3 s	1-2 s	2-3 s	1-2 s	2-3 s	3-4 s
Prop.	0.45	0.45	34.2	36.3	6.63	8.62	10.7
Conv.	0.85	0.85	55.7	55.6	0.38	0.44	0.51

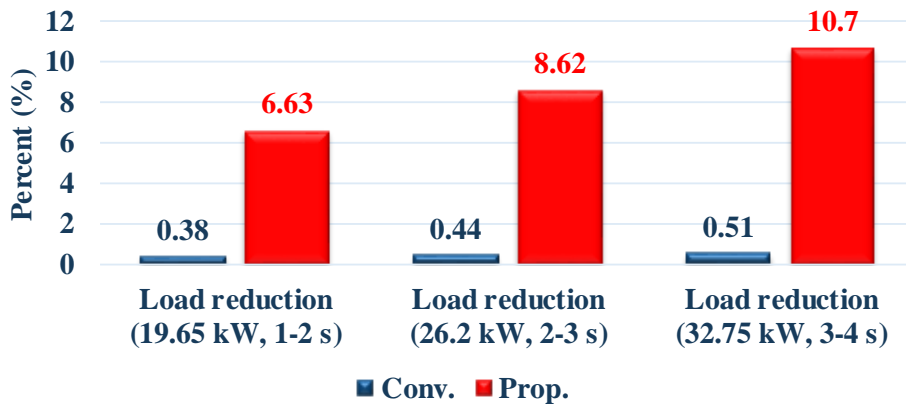


Fig. 5.21. Comparison of load reduction between conventional and proposed methods.

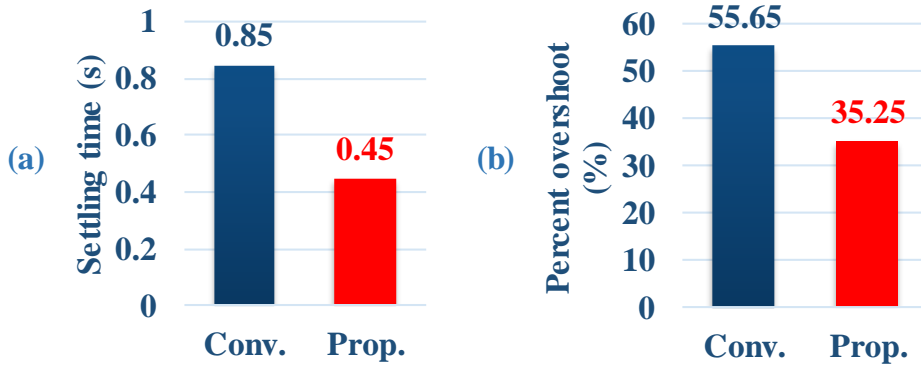


Fig. 5.22. Comparison of control performance between the conventional and proposed methods.

5.2.2. Effects of load power factors on the proposed ACVR

The proposed ACVR strategy was tested for power factors $pf = 1, 0.9,$ and 0.8 of the variable load. In other words, Q_{Load} changed by $0, \pm 6.34$ kvar, and ± 9.83 kvar, respectively, for a step variation in P_{Load} of ± 13.10 kW at $t = 1$ s and 2 s. In (4.1) and (4.2), both n_p and n_q were set to 2. For each power factor, Figs. 5.23 and 5.24 show the variations in the total load demand of the MG and the corresponding profiles of the output voltages of the IDERs, respectively. In Table 5.7, we summarize the results for the proposed and conventional strategies particularly with respect to the maximum voltage reductions and reductions in the active and reactive load demands.

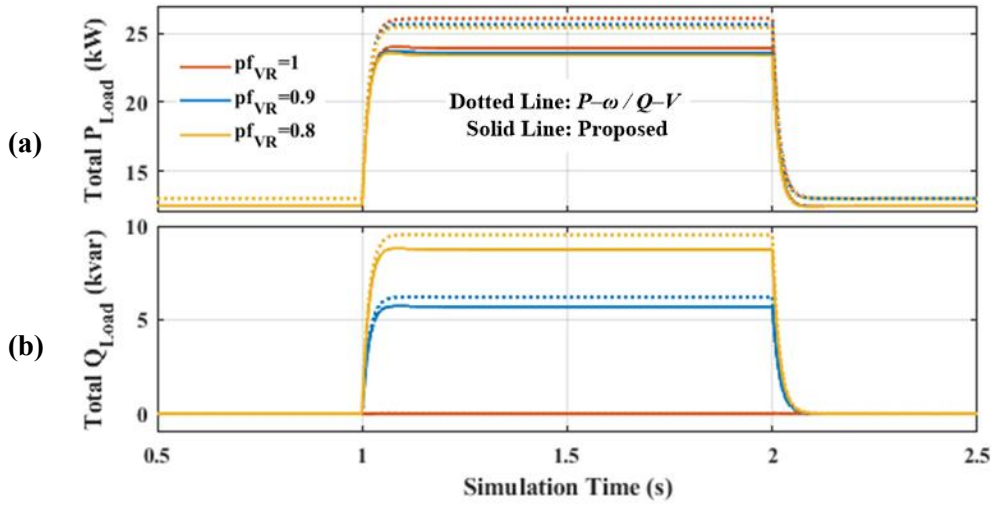


Fig. 5.23. Total (a) active and (b) reactive load demands for different pf s.

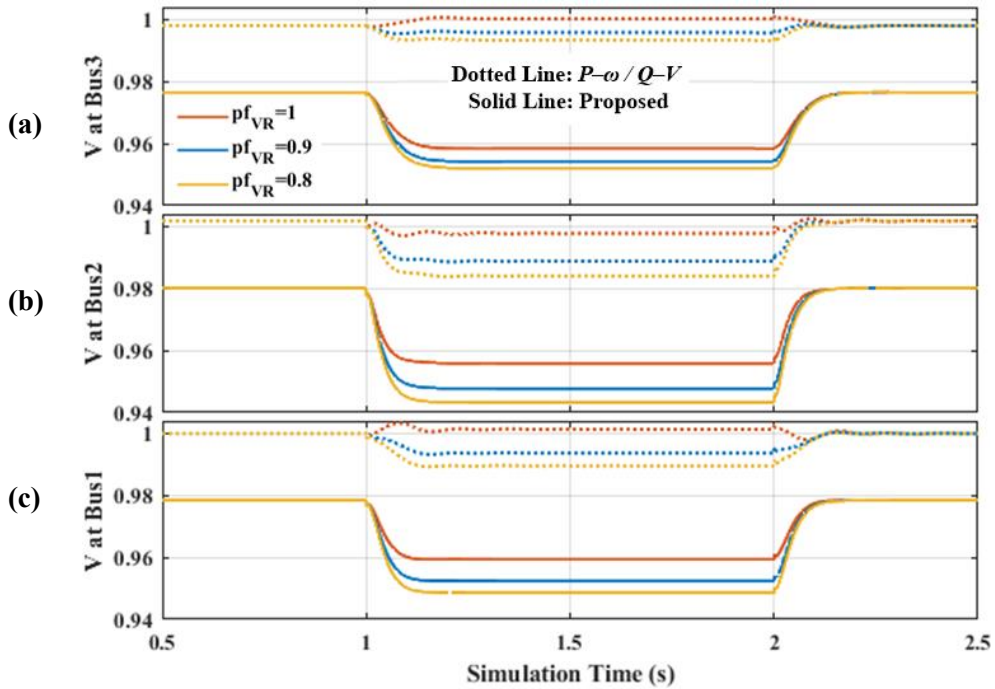


Fig. 5.24. Bus voltage profiles for different pf s.

For example, for $pf = 0.8$, the proposed strategy enabled the IDERs to decrease output voltage by up to 3.69%, in turn reducing the total active and reactive load demands by 10.76% and 11.02%, respectively. In the conventional strategy, the bus voltages were reduced slightly (i.e., by 1.78%). This demonstrates that the proposed

ACVR strategy becomes particularly effective in the case where the MG includes conventional loads (e.g., induction motors and home appliances [79]) operating with relatively low power factors.

Moreover, in both strategies, the lower the power factor, the greater the decrease in the output voltage and, consequently, the total achievable load demand due to the I_q - V and Q - V controllers for reactive power sharing. This implies that n_{ld} and n_{lq} must be determined based on the operating power factors of the loads to improve the performance of the proposed frequency-based CVR strategy while ensuring the voltage stability.

Table 5.7. Performance comparisons for different power factors of the variable load.

	Maximum reduction of V (%)	Reduction of P (%)	Reduction of Q (%)
Prop. (unity pf)	2.43	8.63	-
Prop. ($pf = 0.9$)	3.25	10.00	10.18
Prop. ($pf = 0.8$)	3.69	10.76	11.02
Conv. (unity pf)	0.41	0.42	-
Conv. ($pf = 0.9$)	1.30	2.06	2.22
Conv. ($pf = 0.8$)	1.78	2.90	3.17

5.2.3. Effects of load compositions on the proposed ACVR

The case study, discussed in Chapter 5.2.2, was repeated with different values of n_p in (4.1) and (4.2) to analyze the effects of the voltage dependence of the variable load on the proposed ACVR strategy. Specifically, the analysis was conducted for $n_p = 2, 1, \text{ and } 0$, representing the variable load being operated as a constant-impedance, current, and power load, respectively. As the variable load consumed as much power P_{Load} as half of the total load demand in the MG, the equivalent voltage exponent $n_{p,eq}$ for the total MG load was estimated as 2, 1.5, and 1, respectively. Note that Q_{Load} was set to zero: i.e., $pf = 1$.

Figs. 5.25 and 5.26 show the variations in total load demand and bus voltages, respectively, for step changes in P_{Load} . Table 5.8 shows that for the proposed strategy, bus voltage was reduced by up to 0.956, 0.955, and 0.954 pu (i.e., by up to 2.42%, 2.54%, and 2.66%) for $n_{p,eq} = 2, 1.5,$ and 1, respectively. This led to a reduction in the total load demand of 2.26, 1.74, and 1.17 kW (i.e., 8.62%, 6.65 %, and 4.48%), respectively. In other words, the larger the value of $n_{p,eq}$, the larger the reduction in the load demand. This confirms that the proposed ACVR strategy is effective for reducing the total load demand, particularly for the case where the constant-impedance loads account for a large proportion of the load. On the contrary, the conventional droop control strategy led to little variations in the bus voltages due to $Q_{Load} = 0$. Fig. 5.26 shows that the voltage profile at each bus remained the same for $n_p = 2, 1,$ and 0.

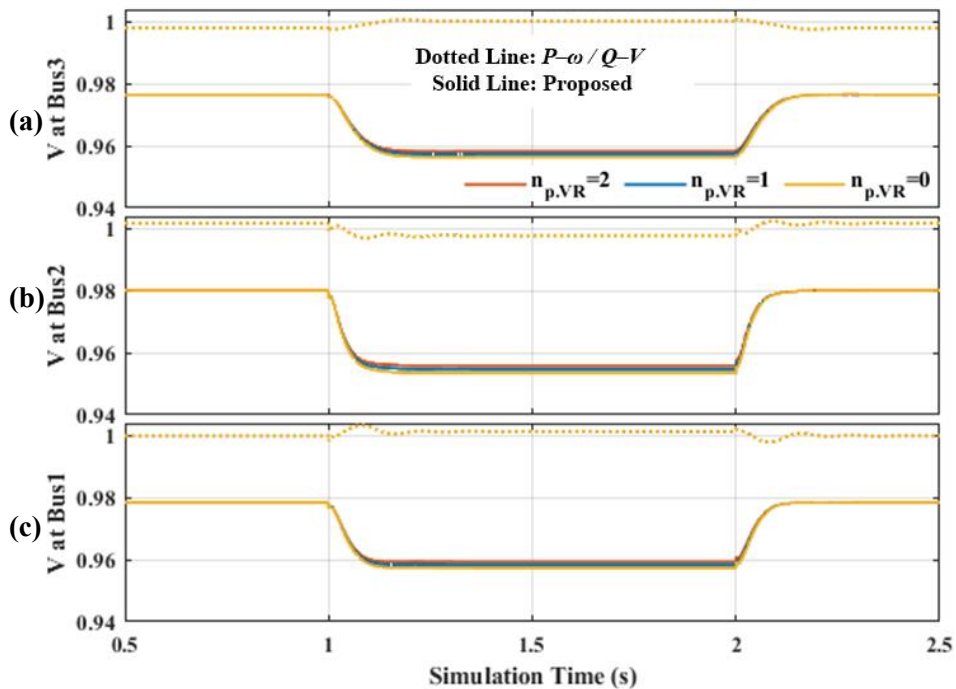


Fig. 5.25. Total (a) active and (b) reactive load demands for different n_p in (4.1).

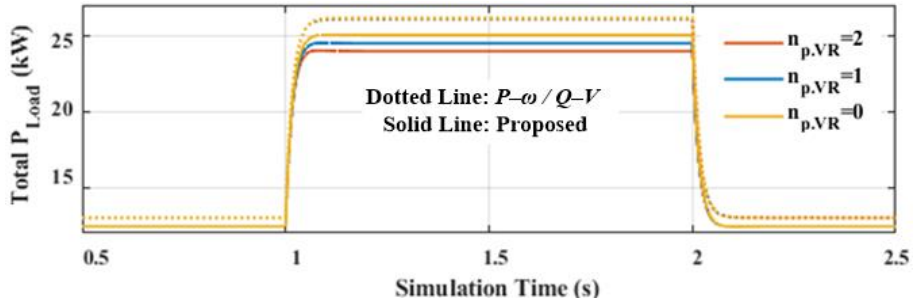


Fig. 5.26. Bus voltage profiles for different values of n_p in (4.1).

Table 5.8. Performance comparisons for different voltage exponents of the variable load.

	Equivalent voltage exponent, $n_{p,eq}$	Maximum reduction of V (%)	Reduction of P (%)
Conv.	2	0.41	0.42
Prop. ($n_p = 2$)	2	2.42	8.62
Prop. ($n_p = 1$)	1.5	2.54	6.65
Prop. ($n_p = 0$)	1	2.66	4.48

5.2.4. Performance validation of the proposed ACVR strategy for different n_{Id}

The case study, discussed in Chapter 5.2.1, was repeated until $t = 3$ s with different values of n_{Id} to confirm that the proposed ACVR works well although the I_d - ω droop coefficients of IDERs have different values. Specifically, the analysis was conducted for different values of m_{Id1} (original value, $m_{Id1}=3.59 \times 10^{-2}$), m_{Id2} (20% increased value, $m_{Id2}=4.31 \times 10^{-2}$), and m_{Id3} (20% reduced value, $m_{Id3}=2.87 \times 10^{-2}$). The corresponding values of n_{Id2} and n_{Id3} were recalculated by (4.19) for the original value of k_{ACVR} ($k_{ACVR}=20.22$). Consequently, n_{Id2} and n_{Id3} are set to 0.871 and 0.58, respectively.

Figs. 5.27 and 5.28 show the active/reactive power outputs and frequency/voltage profiles of the IDERs for different m_{id} and n_{Id} , respectively. Since the values of m_{Id} have been changed, the active power output is shared by their corresponding droop coefficients as shown in Fig 5.27(a). For the reactive power

outputs shown in Fig 5.27(b), since the power flow has been changed according to the changed m_{ld} , the reactive power sharing by IDERs is also changed.

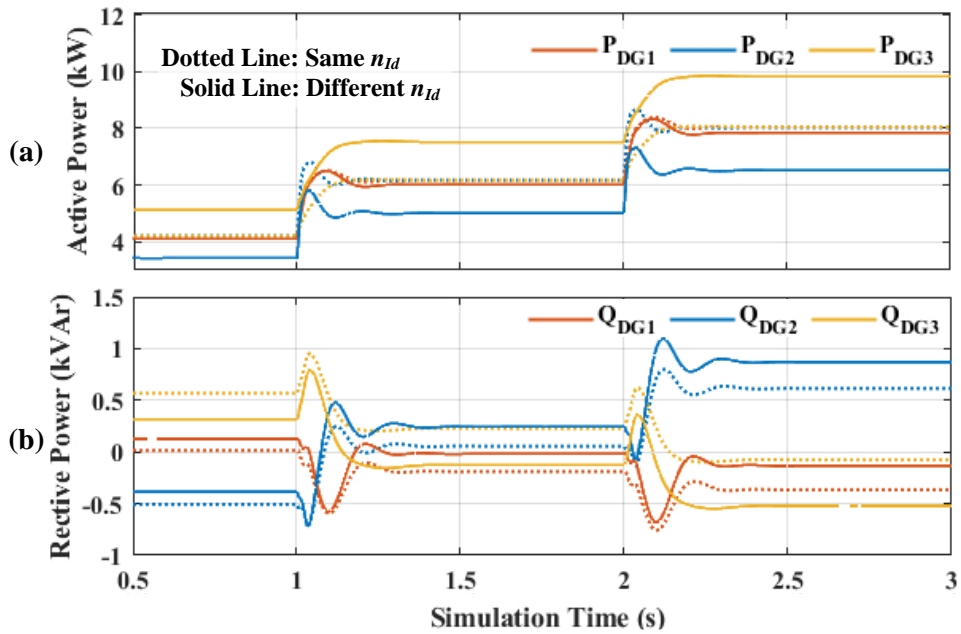


Fig. 5.27. (a) Active and (b) reactive power outputs of the IDERs for different m_{ld} and n_{ld} .

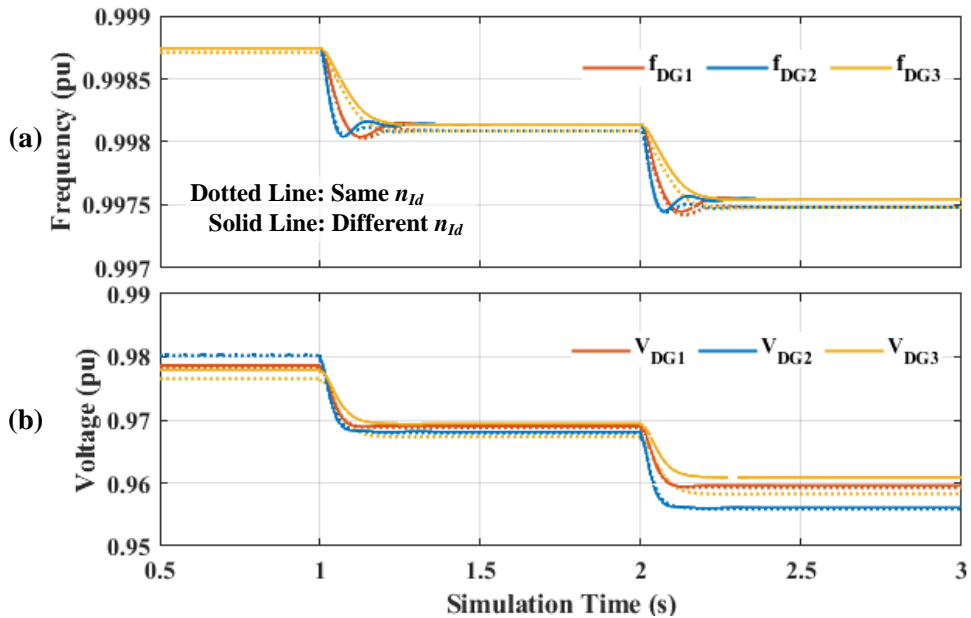


Fig. 5.28. (a) Frequency and (b) voltage profiles at the output nodes of the IDERs for different m_{ld} and n_{ld} .

As m_{Id2} and m_{Id3} of IDER₂ and IDER₃ are changed, the active power output of each IDER is different. However, in order to apply the proposed ACVR, the value of n_{Id} also changed by (4.19). Consequently, the voltage drop by I_d - V droop control of individual IDER is the same as $k_{ACVR}*\Delta\omega$. On the other hand, as shown in Fig 5.28(b), the voltage reduction by I_q - V droop control is different for each bus as in the original case, and has a different value from the original case since the reactive power profile is different from the original one as shown in Fig 5.27(b).

In particular, since the voltage at the bus 3 has been reduced from 0.9609 to 0.9583 pu, the load reduction caused by the voltage drop is increased and the total power output of IDERs is reduced. Therefore, the frequency is converged slightly higher than in the conventional case. This results confirms that proposed ACVR can be operated while maintaining the voltage profile without communication links even when the droop coefficient of IDER is different. The results are also consistent with the equations of the proposed I_{dq} controllers, discussed in Chapter 4.2.

Chapter 6. Conclusions and Future Extensions

6.1 Conclusions

Islanded operation scheme of MGs is attracting considerable attention since it can be applied to the various fields as well as general MGs connected to utilities. MG applications for those cases have advantages as: leveraging the capabilities of RES; improving power availability and reliability; enabling sustainable and eco-friendly energy system. Moreover, IDER allows more fast and prompt responses compared to conventional synchronous generator for system dynamics.

This dissertation focuses on an inverter-based islanded MG, and proposes an autonomous power management strategy of inverter-based islanded MGs for the scheme of SMO and MMO, respectively, to achieve a reliable and stable system operation. Both schemes used a load-voltage dependence and system frequency determined by master IDER. The frequency is utilized for communication and the load-voltage dependence is utilized for detecting abnormal condition for SMO, which is the power balance is no more maintained. In MMO, this dependence is used for demand side management to obtain a virtual reserve by reducing power consumption of the load.

For SMO, the VFPC has been proposed as an additional controller that can be easily integrated with the conventional CVCF controller of the BESS in the isolated MG. This effectively assists a MG system operator to resolve the under-voltage problem owing to the limited reserve of the grid-forming BESS. This method uses the system frequency as a global bus signal, enabling the indirect control of other DERs without communications systems. Moreover, the detailed simulation model was implemented in MATLAB/Simulink using actual system parameters to verify the effectiveness of the proposed active power management strategy. The simulation results show that the proposed VFPC method can mitigate the active power shortage

and the bus voltage reduction using the frequency-based operation of the DERs in the MG. From the simulation results, the main advantages of the proposed VFPC can be summarized as follows:

- The proposed VFPC can be easily applied to the existing CVCF controller of the grid-forming BESS and enables the coordinated control with other DERs that operate with conventional P - f droop controllers.
- The proposed VFPC can be activated based on the local measurement of its bus voltage, not active power, even when sudden and severe imbalance of active power takes place in the MG.
- The proposed controller is activated only during the period of active power imbalance unlike the conventional f - P droop method, the CVCF controller can still reduce the fluctuation of frequency and active power under the normal operating condition.

For islanded mode with MMO, proposed a new ACVR strategy incorporated with the current-based droop control to improve the operational reliability of the inverter-based MG. For the proposed ACVR, the I_{dq} controller was developed as the outer feedback controller of the IDER, requiring no communications systems. The I_{dq} controller consists of the I_d - V controller for ACVR and the I_d - ω and I_q - V controllers for power sharing. The I_d - V controllers adjusted the output voltages of the individual IDERs by the same amount in proportion to the MG frequency variation, mainly determined by the I_d - ω controllers. In other words, the autonomous operation of the IDERs could be achieved using the global signal throughout the MG, so that the local controllers of the IDERs reduced the output voltages while maintaining the overall profile of the original voltages at the MG buses. The I_q - V controllers, integrated with the I_d - V controllers, also adjusted the IDER voltages for the reactive power sharing. The current-based controllers can enable the IDERs to respond faster to the variations in the load demand, improving the transient responses of the IDERs. The state-space model of the three-bus MG test bed was implemented to perform the small-signal analysis particularly for variations in the coefficients of

m_{ld} and n_{lq} . The proposed ACVR was verified to increase the system damping and consequently improve the reliability in the MG operation. The case studies were also performed to demonstrate that for an increase in the load demand, the proposed ACVR led to the larger reductions in the bus voltages and consequently in the power inputs of the constant-impedance loads, resulting in the larger system damping. The proposed ACVR was also verified to be effective for the MG that includes large constant impedance loads operating with relatively low power factors. The main contributions of proposed frequency-based ACVR scheme for MMO are summarized as follows:

- Proposed frequency-based ACVR is achieved using an outer controller with a simple structure and consequently can be readily integrated with the outer feedback loops of the individual units for droop control;
- Using only local measurements and controllers of each IDER, the virtual reserve can be more obtained under heavy loading condition by ACVR in the islanded MG: i.e., when additional reserve is required;
- The small-signal analysis has been performed, consistent with the simulation case study results, to demonstrate that the proposed frequency-based ACVR further improves the stability and reliability of the inverter-based islanded MG.

By using the proposed operation methods, it is anticipated that the penetration level of intermittent RESs and the utilization of the DC technology into the power system will increase, and further the system operation can be more reliable and economical, particularly in situations, where frequent and rapid variations in the load demand and RES output power occur.

6.2 Future extensions

The proposed methods can be improved considering following contents:

- load models in MG test systems are based on simple mathematical model. However, because the dynamic response of actual load for system transients is different by their load characteristics, more detailed load modeling approach, as described in Chapter 2.2.1, is necessary to better reflect the characteristics of the real MG systems.

- In MMO scheme, a proposed frequency-based CVR may be possible to determine the optimal values of n_{Idi} and ΔV_{ACVRi} for the individual IDERs in an autonomous manner. To consider line drop and overall voltage profile, this may require additional information such as the coefficients of other droop generators, line impedance information, and so on. This is left for future work.

- An adaptive approach to determine n_{Id} or k_{ACVR} , in coordination with voltage regulating devices such as LTC, SC, and shunt capacitor by utilizing frequency as a global signal, is also worth investigating in future research.

- A hierarchical scheme can be applicable for proposed autonomous schemes. The proposed control schemes are in a primary control layer from the viewpoint of hierarchical structure. If it can be linked with additional secondary control, can complement the p control and enable more efficient and optimal system operation can be realized. To establish hierarchical control scheme, further study and research are needed.

Bibliographies

- [1] R. Teodorescu, M. Liserre, and P. Rodriguez, Grid converters for photovoltaic and wind power systems. John Wiley & Sons, 2011.
- [2] L. M. Jing, D. H. Son, S. H. Kang, and S. R. Nam, "A novel protection method for single line-to-ground faults in ungrounded low-inertia microgrids," *Energies*, vol. 9, no. 6, p. 459, Jun. 2016.
- [3] N. Hatziargyriou, *Microgrids: architectures and control*. Chichester: Wiley, IEEE-Press,, 2014, pp. XXI, 317 S.
- [4] M. A. Hossain, H. R. Pota, M. J. Hossain, and F. Blaabjerg, "Evolution of microgrids with converter-interfaced generations: challenges and opportunities," *Int. J. Elec. Power.*, vol. 109, pp. 160-186, 2019.
- [5] X. N. Lu and J. H. Wang. (2017, Jun) A game changer: Electrifying remote communities by using isolated microgrids. *IEEE Electrification Magazine*. 56-63. Available: <Go to ISI>://WOS:000414996600007
- [6] J. H. Lee, S. H. Lee, and S. K. Sul, "Variable-speed engine generator with super capacitor: Isolated power generation system and fuel efficiency," *IEEE Trans. Ind. Appl.*, vol. 45, no. 6, pp. 2130-2135, Nov-Dec 2009.
- [7] M. R. B. Neto, P. C. M. Carvalho, J. O. B. Carioca, and F. J. F. Canafistula, "Biogas/photovoltaic hybrid power system for decentralized energy supply of rural areas," (in English), *Energy Policy*, vol. 38, no. 8, pp. 4497-4506, Aug. 2010.
- [8] Z. M. Tong and K. M. Zhang, "The near-source impacts of diesel backup generators in urban environments," *Atmospheric Environment*, vol. 109, pp. 262-271, May 2015.
- [9] D. Arent, J. Barnett, G. Mosey, and A. Wise, "The potential of renewable energy to reduce the dependence of the state of hawaii on oil," in *System Sciences, 2009. HICSS'09. 42nd Hawaii International Conference on*, 2009: IEEE, pp. 1-11.

- [10] M. N. Uddin, M. A. Rahman, and M. Sir, "Reduce generators noise with better performance of a diesel generator set using modified absorption silencer," *Global Journal of Research in Engineering*, 2016.
- [11] B. Kroposki, C. Pink, R. DeBlasio, H. Thomas, M. Simoes, and P. K. Sen, "Benefits of power electronic interfaces for distributed energy systems," *IEEE Trans. Energy Convers.*, vol. 25, no. 3, pp. 901-908, Sep. 2010.
- [12] Q. C. Zhong, "Power-electronics-enabled autonomous power systems: architecture and technical routes," *IEEE Trans. Ind. Electron.*, vol. 64, no. 7, pp. 5907-5918, Jul. 2017.
- [13] N. Pogaku, M. Prodanovic, and T. C. Green, "Modeling, analysis and testing of autonomous operation of an inverter-based microgrid," *IEEE Trans. Power Electr.*, vol. 22, no. 2, pp. 613-625, Mar. 2007.
- [14] D. E. Olivares, C. A. Canizares, and M. Kazerani, "A centralized energy management system for isolated microgrids," *IEEE Trans. Smart Grid*, vol. 5, no. 4, pp. 1864-1875, Jul. 2014.
- [15] D. E. Olivares et al., "Trends in microgrid control," *IEEE Trans. Smart Grid*, vol. 5, no. 4, pp. 1905-1919, Jul. 2014.
- [16] S. Parhizi, H. Lotfi, A. Khodaei, and S. Bahramirad, "State of the art in research on microgrids: A Review," *IEEE Access*, vol. 3, pp. 890-925, 2015.
- [17] A. Kaur, J. Kaushal, and P. Basak, "A review on microgrid central controller," *Renew. Sustain. Energy Rev.*, vol. 55, pp. 338-345, Mar 2016.
- [18] H. Kim, J. Bae, S. Baek, D. Nam, H. Cho, and H. J. Chang, "Comparative Analysis between the Government Micro-Grid Plan and Computer Simulation Results Based on Real Data: The Practical Case for a South Korean Island," *Sustainability-Basel*, vol. 9, no. 2, p. 197, Feb 2017.
- [19] S.-Y. Kim and J. A. Mathews, "Korea's Greening Strategy: The role of smart microgrids," *The asia-Pacific Journal*, vol. 14, no. 24, 2016.

- [20] W. H. Hwang et al., "Autonomous microgrid design for supplying electricity in carbon-free island," *J. Electr. Energy Technol.*, vol. 9, no. 3, pp. 1112-1118, May 2014.
- [21] W. K. Chae, H. J. Lee, J. N. Won, J. S. Park, and J. E. Kim, "Design and field tests of an inverter-based remote microgrid on a Korean Island," *Energies*, vol. 8, no. 8, pp. 8193-8210, Aug. 2015.
- [22] S.-H. Kim, I.-Y. Chung, H.-J. Lee, and W.-K. Chae, "Voltage and frequency control method using battery energy storage system for a stand-alone microgrid," *The Transactions of the Korean Institute of Electrical Engineers*, vol. 64, no. 8, pp. 1168-1179, 2015.
- [23] W. K. Chae, J. N. Won, H. J. Lee, J. E. Kim, and J. Kim, "Comparative analysis of voltage control in battery power converters for inverter-based AC microgrids," *Energies*, vol. 9, no. 8, p. 596, Aug. 2016.
- [24] Y. S. Kim, E. S. Kim, and S. I. Moon, "Frequency and voltage control strategy of standalone microgrids with high penetration of intermittent renewable generation systems," *IEEE Trans. Power Syst.*, vol. 31, no. 1, pp. 718-728, Jan. 2016.
- [25] H. Kim et al., "Comparative analysis of on- and off-grid electrification: the case of two South Korean Islands," *Sustainability-Basel*, vol. 8, no. 4, p. 350, Apr. 2016.
- [26] H.-J. Moon, J. W. Chang, E.-S. Kim, and S.-I. Moon, "Frequency-based wireless control of distributed generators in an isolated microgrid: A case of Geocha Island in South Korea," in *Universities Power Engineering Conference (UPEC), 2017 52nd International, 2017: IEEE*, pp. 1-6.
- [27] J. Won, W. Chae, H. Lee, J. Park, J. Sim, and C. Shin, "Demonstration of remote microgrid system in Korean island," *CIREN-Open Access Proceedings Journal*, vol. 2017, no. 1, pp. 2212-2214, 2017.
- [28] M. C. Chandorkar, D. M. Divan, and R. Adapa, "Control of parallel connected inverters in standalone AC supply-systems," *IEEE Trans. Ind. Appl.*, vol. 29, no. 1, pp. 136-143, Jan-Feb 1993.

- [29] J. A. P. Lopes, C. L. Moreira, and A. G. Madureira, "Defining control strategies for microgrids islanded operation," *IEEE Trans. Power Syst.*, vol. 21, no. 2, pp. 916-924, May 2006.
- [30] I. Y. Chung, W. X. Liu, D. A. Cartes, E. G. Collins, and S. I. Moon, "Control methods of inverter-interfaced distributed generators in a microgrid system," *IEEE Trans. Ind. Appl.*, vol. 46, no. 3, pp. 1078-1088, May-Jun 2010.
- [31] J. Kim, J. M. Guerrero, P. Rodriguez, R. Teodorescu, and K. Nam, "Mode adaptive droop control with virtual output impedances for an inverter-based flexible AC microgrid," *IEEE Trans. Power Electr.*, vol. 26, no. 3, pp. 689-701, Mar. 2011.
- [32] M. B. Delghavi and A. Yazdani, "An adaptive feedforward compensation for stability enhancement in droop-controlled inverter-based microgrids," *IEEE Trans. Power Del.*, vol. 26, no. 3, pp. 1764-1773, Jul. 2011.
- [33] Y. Sun, X. C. Hou, J. Yang, H. Han, M. Su, and J. M. Guerrero, "New perspectives on droop control in AC microgrid," *IEEE Trans. Ind. Electron.*, vol. 64, no. 7, pp. 5741-5745, Jul. 2017.
- [34] M. S. Golsorkhi and D. D. Lu, "A control method for inverter-based islanded microgrids based on V-I droop characteristics," *IEEE Trans. Power Del.*, vol. 30, no. 3, pp. 1196-1204, 2015.
- [35] A. Solanki, A. Nasiri, V. Bhavaraju, Y. L. Familiant, and Q. Fu, "A new framework for microgrid management: virtual droop control," *IEEE Trans. Smart Grid*, vol. 7, no. 2, pp. 554-566, Mar. 2016.
- [36] R. A. Mastromauro, "Voltage control of a grid-forming converter for an AC microgrid: A real case study," in *Renewable Power Generation Conference (RPG 2014)*, 3rd, 2014: IET, pp. 1-6.
- [37] P. K. Sen and K. H. Lee, "Conservation voltage reduction technique: an application guideline for smarter grid," *IEEE Trans. Ind. Appl.*, vol. 52, no. 3, pp. 2122-2128, May-Jun 2016.

- [38] M. Farrokhhabadi, C. A. Canizares, and K. Bhattacharya, "Frequency control in isolated/islanded microgrids through voltage regulation," *IEEE Trans. Smart Grid*, vol. 8, no. 3, pp. 1185-1194, May 2017.
- [39] A. M. Pasha, H. H. Zeineldin, A. S. Al-Sumaiti, M. S. El Moursi, and E. F. El Sadaany, "Conservation voltage reduction for autonomous microgrids based on V–I droop characteristics," *IEEE Trans. Sustain. Energ.*, vol. 8, no. 3, pp. 1076-1085, 2017.
- [40] A. Aderibole, H. H. Zeineldin, M. Al Hosani, and E. El-Saadany, "Demand side management strategy for droop-based autonomous microgrids through voltage reduction," *IEEE Trans. Energy Convers.*, 2018.
- [41] M. Yazdani and A. Mehrizi-Sani, "Distributed control techniques in microgrids," *IEEE Trans. Smart Grid*, vol. 5, no. 6, pp. 2901-2918, Nov. 2014.
- [42] M. M. A. Abdelaziz and H. E. Farag, "An enhanced supervisory control for islanded microgrid systems," *IEEE Trans. Smart Grid*, vol. 7, no. 4, pp. 1941-1943, Jul. 2016.
- [43] B. Lasseter, "Microgrids [distributed power generation]," in 2001 IEEE power engineering society winter meeting. Conference proceedings (Cat. No. 01CH37194), 2001, vol. 1: IEEE, pp. 146-149.
- [44] R. H. Lasseter, "Microgrids," in 2002 IEEE Power Engineering Society Winter Meeting. Conference Proceedings (Cat. No. 02CH37309), 2002, vol. 1: IEEE, pp. 305-308.
- [45] L. Meng et al., "Flexible system integration and advanced hierarchical control architectures in the microgrid research laboratory of Aalborg University," *IEEE Trans. Ind. Appl.*, vol. 52, no. 2, pp. 1736-1749, 2016.
- [46] B. L. Capehart, "Distributed energy resources (DER)," College of Engineering, University of Florida, 2010.
- [47] J. Rocabert, A. Luna, F. Blaabjerg, and P. Rodriguez, "Control of power converters in AC microgrids," *IEEE Trans. Power Electr.*, vol. 27, no. 11, pp. 4734-4749, Nov 2012.

- [48] A. D. Paquette, M. J. Reno, R. G. Harley, and D. M. Divan, "Sharing transient loads: Causes of unequal transient load sharing in islanded microgrid operation," *IEEE Ind. Appl. Mag.*, vol. 20, no. 2, pp. 23-34, 2014.
- [49] H. Bevrani, B. François, and T. Ise, *Microgrid dynamics and control*. John Wiley & Sons, 2017.
- [50] M. A. Eltawil and Z. Zhao, "Grid-connected photovoltaic power systems: Technical and potential problems—A review," *Renewable and sustainable energy reviews*, vol. 14, no. 1, pp. 112-129, 2010.
- [51] Y. S. Kim, C. S. Hwang, E. S. Kim, and C. Cho, "State of charge-based active power sharing method in a standalone microgrid with high penetration level of renewable energy sources," *Energies*, vol. 9, no. 7, Jul. 2016.
- [52] M. Y. Worku, M. A. Hassan, and M. A. Abido, "Real time energy management and control of renewable energy based microgrid in grid connected and island modes," *Energies*, vol. 12, no. 2, Jan. 2019.
- [53] P. Kundur, N. J. Balu, and M. G. Lauby, *Power system stability and control* (EPRI power system engineering series). New York: McGraw-Hill, 1994, pp. xxiii, 1176 p.
- [54] A. Arif, Z. Y. Wang, J. H. Wang, B. Mather, H. Bashualdo, and D. B. Zhao, "Load modeling-A review," *IEEE Trans. Smart Grid*, vol. 9, no. 6, pp. 5986-5999, Nov 2018.
- [55] W. Price et al., "Load representation for dynamic performance analysis," *IEEE Trans. on Power Sys.*, vol. 8, no. 2, 1993.
- [56] L. G. Swan and V. I. Ugursal, "Modeling of end-use energy consumption in the residential sector: A review of modeling techniques," *Renewable and sustainable energy reviews*, vol. 13, no. 8, pp. 1819-1835, 2009.
- [57] C. Concordia and S. Ihara, "Load representation in power system stability studies," *IEEE Trans. on power apparatus and systems*, no. 4, pp. 969-977, 1982.

- [58] Z. Y. Wang and J. H. Wang, "Review on implementation and assessment of conservation voltage reduction," *IEEE Trans. Power Syst.*, vol. 29, no. 3, pp. 1306-1315, May 2014.
- [59] M. Gheydi, A. Nouri, and N. Ghadimi, "Planning in microgrids with conservation of voltage reduction," *IEEE Syst. J.*, vol. 12, no. 3, pp. 2782-2790, Sep 2018.
- [60] R. Beck, "Distribution efficiency initiative final report," Northwest Energy Efficiency Alliance Report, 2007.
- [61] A. Standard, "C84. 1-1982," American National Standard for Electric Power Systems and Equipment-Voltage Ratings (60Hz).
- [62] IEEE Guide for Design, Operation, and Integration of Distributed Resource Island Systems with Electric Power Systems, 2011.
- [63] P. G. a. E. Company. (1999). Voltage Tolerance Boundary [Online]. Available: https://www.pge.com/includes/docs/pdfs/mybusiness/customerservice/energystatus/powerquality/voltage_tolerance.pdf.
- [64] R. Preiss and V. Warnock, "Impact of voltage reduction on energy and demand," *IEEE Trans. Power Apparatus and Systems*, no. 5, pp. 1665-1671, 1978.
- [65] D. Lauria, "Conservation voltage reduction (CVR) at Northeast utilities," *IEEE Trans. Power Del.*, vol. 2, no. 4, pp. 1186-1191, 1987.
- [66] B. Kennedy and R. Fletcher, "Conservation voltage reduction (CVR) at Snohomish County PUD," *IEEE Trans. Power Syst.*, vol. 6, no. 3, pp. 986-998, 1991.
- [67] A. Dwyer, R. E. Nielsen, J. Stangl, and N. S. Markushevich, "Load to voltage dependency tests at BC Hydro," *IEEE Trans. Power Syst.*, vol. 10, no. 2, pp. 709-715, 1995.
- [68] E. P. R. Institute. (2011). Green Circuits: Distribution Efficiency Case Studies, Available: <https://www.epri.com/#/pages/product/1023518/>.

- [69] K.-S. Shim et al., "Estimation of conservation voltage reduction factors using measurement data of KEPCO system," *Energies*, vol. 10, no. 12, p. 2148, Dec. 2017.
- [70] T. Wilson, "Energy conservation with voltage reduction-fact or fantasy," in 2002 Rural Electric Power Conference. Papers Presented at the 46th Annual Conference (Cat. No. 02CH37360), 2002: IEEE, pp. C3-1.
- [71] S. Leitner, M. Yazdani, A. Mehrizi-Sani, and A. Muetze, "Small-Signal Stability Analysis of an Inverter-Based Microgrid with Internal Model-Based Controllers," *IEEE Trans. Smart Grid*, vol. 9, no. 5, pp. 5393-5402, Sep. 2018.
- [72] T. Tsuji, M. Mizuochi, and K. Ohnishi, "Technical issues on velocity measurement for motion control," in 2006 12th International Power Electronics and Motion Control Conference, IEEE, pp. 326-331, 2, Oct. 2006.
- [73] H.-J. Moon, J. W. Chang, S.-Y. Lee, and S.-I. Moon, "Autonomous active power management in isolated microgrid based on proportional and droop control," *Energy Procedia*, vol. 153, pp. 48-55, Oct. 2018.
- [74] F. Katiraei, R. Iravani, N. Hatziargyriou, and A. Dimeas, "Microgrids management," *IEEE Power Energy Mag.*, vol. 6, no. 3, pp. 54-65, May-Jun 2008.
- [75] T. C. Green and M. Prodanovic, "Control of inverter-based micro-grids," *Electr. Power Syst. Res.*, vol. 77, no. 9, pp. 1204-1213, Jul. 2007.
- [76] J.-W. Chang, G.-S. Lee, H.-J. Moon, M. B. Glick, and S.-I. Moon, "Coordinated frequency and state-of-charge control with multi-battery energy storage systems and diesel generators in an isolated microgrid," *Energies*, vol. 12, no. 9, p. 1614, 2019.
- [77] N. Femia, G. Petrone, G. Spagnuolo, and M. Vitelli, "Optimization of perturb and observe maximum power point tracking method," *IEEE Trans. Power Electr.*, vol. 20, no. 4, pp. 963-973, Jul. 2005.
- [78] M. A. Abdullah, A. H. M. Yatim, C. W. A. Tan, and R. Saidur, "A review of maximum power point tracking algorithms for wind energy systems," *Renew. Sust. Energy Rev.*, vol. 16, no. 5, pp. 3220-3227, Jun. 2012.

- [79] A. Bokhari et al., “Experimental determination of the ZIP coefficients for modern residential commercial and industrial loads”, IEEE Trans. Power Del., vol. 29, no. 3, pp. 1372-1381, Jun. 2014.

Appendix A. Small-signal State-Space Model of General Inverter-Based Island Microgrids

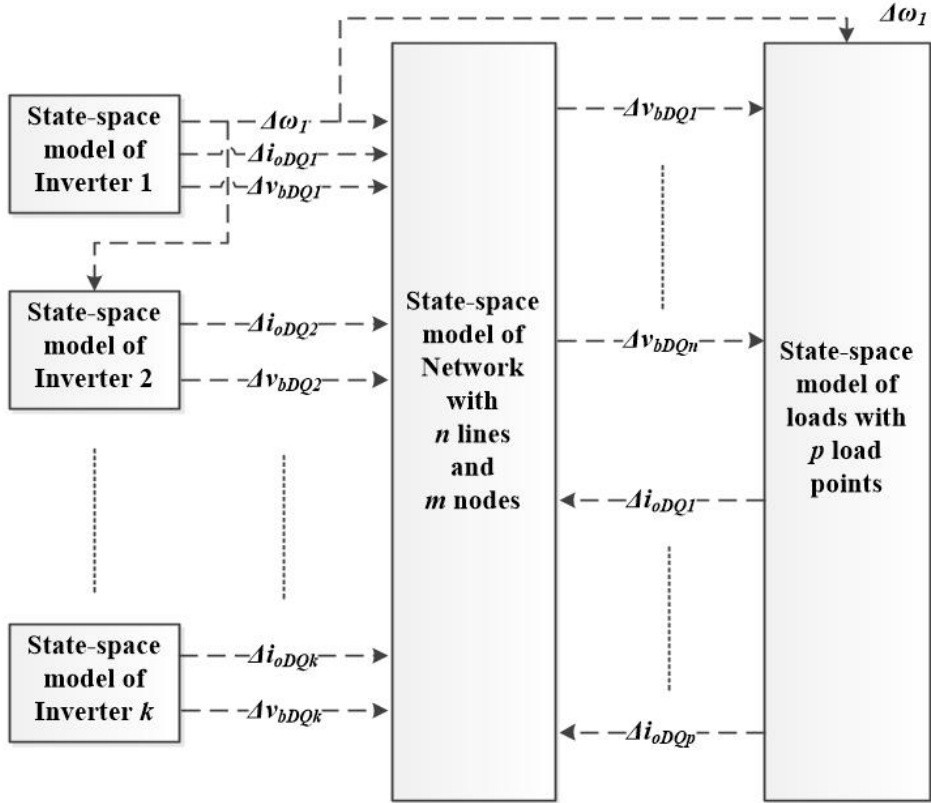


Fig A. 1. Block diagram of modeling approach for complete small-signal state-space model of inverter-based islanded microgrid.

A complete state-space model of the inverter-based islanded MG, is established to analyze the small-signal stability for the proposed and conventional schemes. As shown in Fig. A. 1, the state-space modeling is achieved by dividing the entire MG into three modules: i.e., the inverter of IDERs, the loads, and the network lines. In particular, each inverter of IDER is modeled to operate on an individual dq -reference frame with the frequency value set by its proposed local controller. The DQ-axis of inverter 1 assumed to be a common reference frame rotating at an angular frequency

ω_{com} . The state-space model of network and the loads are expressed on the DQ-reference frame (common reference frame) of inverter 1.

Note that apart from the proposed I_{dq} controller, the state-space model is implemented mainly based on [13] and [71]. For example, the dq -axis variables Δx_d and Δx_q are aggregated as $\Delta x_{dq} = [\Delta x_d, \Delta x_q]^T$ for simple representation. The combination of the state variables of the system is simply represented as $[\Delta x] = [\Delta x_1, \Delta x_2, \dots, \Delta x_n]^T$.

the input and output variables in the individual reference frame have been transformed to those in the common reference frame, using the transformation technique in [A3], are represented by the subscript of DQ as:

$$\begin{bmatrix} \Delta i_{oDQi} \end{bmatrix} = \begin{bmatrix} T_{Si} \end{bmatrix} \begin{bmatrix} \Delta i_{odqi} \end{bmatrix} + \begin{bmatrix} T_{Ci} \end{bmatrix} \begin{bmatrix} \Delta \delta_i \end{bmatrix}, \quad (\text{A1})$$

$$\begin{bmatrix} \Delta v_{bdqi} \end{bmatrix} = \begin{bmatrix} T_{Si}^{-1} \end{bmatrix} \begin{bmatrix} \Delta v_{bDQi} \end{bmatrix} + \begin{bmatrix} T_{Vi}^{-1} \end{bmatrix} \begin{bmatrix} \Delta \delta_i \end{bmatrix}, \quad (\text{A2})$$

The transformation matrices for axis shift matrices $[T_{Si}]$, $[T_{Ci}]$, and $[T_{Vi}]$ can be expressed as:

$$\mathbf{T}_{Si} = \begin{bmatrix} \cos \delta_i & -\sin \delta_i \\ \sin \delta_i & \cos \delta_i \end{bmatrix} \quad (\text{A3})$$

$$\mathbf{T}_{Ci} = \begin{bmatrix} -i_{odi} \sin \delta_i & -i_{oqi} \cos \delta_i \\ i_{odi} \cos \delta_i & i_{oqi} \sin \delta_i \end{bmatrix} \quad (\text{A4})$$

$$\mathbf{T}_{Vi}^{-1} = \begin{bmatrix} -v_{bDi} \sin \delta_i + v_{bQi} \cos \delta_i \\ v_{bDi} \cos \delta_i - v_{bQi} \sin \delta_i \end{bmatrix} \quad (\text{A5})$$

where the δ_i is the reference frame angle of i -th inverter with respect to the common DQ-reference frame of the inverter 1. Note that the three-phase currents and voltages are expressed as vectors with the subscript of dq, rotating in individual dq -frame. On the other hand, the other variables such as angle, filtered I_d and I_q are represented as scalars.

A.1 State-space modeling of IDERs with proposed controllers

A.1.1 State-space model of I_{dq} controller

The proposed I_{dq} controller for an individual inverter model, rotating on individual dq -reference frame, shown in Fig. 4.2, can be expressed considering the additional I_d - V feedback loop as:

$$\begin{aligned} \begin{bmatrix} \dot{\Delta\delta} \\ \Delta I_{od} \\ \Delta I_{oq} \end{bmatrix} &= \underbrace{\begin{bmatrix} 0 & -m_{Id} & 0 \\ 0 & -\omega_c & 0 \\ 0 & 0 & -\omega_c \end{bmatrix}}_{\mathbf{A}_P} \begin{bmatrix} \Delta\delta \\ \Delta I_{od} \\ \Delta I_{oq} \end{bmatrix} + \underbrace{\begin{bmatrix} -1 \\ 0 \\ 0 \end{bmatrix}}_{\mathbf{B}_{P\omega}} \Delta\omega_{com} \\ &+ \underbrace{\begin{bmatrix} 0 & 0 & 0 & 0 & 0 & 0 \\ 0 & 0 & 0 & 0 & \omega_c & 0 \\ 0 & 0 & 0 & 0 & 0 & \omega_c \end{bmatrix}}_{\mathbf{B}_P} \begin{bmatrix} \Delta i_{ldq} \\ \Delta v_{odq} \\ \Delta i_{odq} \end{bmatrix} \end{aligned} \quad (\text{A6})$$

$$\begin{aligned} \begin{bmatrix} \Delta\omega^* \\ \Delta v_{od}^* \\ \Delta v_{oq}^* \end{bmatrix} &= \underbrace{\begin{bmatrix} 0 & -m_{Id} & 0 \\ 0 & -n_{Id} & n_{Iq} \\ 0 & 0 & 0 \end{bmatrix}}_{\mathbf{C}_{P\omega}} \begin{bmatrix} \Delta\delta \\ \Delta I_{od} \\ \Delta I_{oq} \end{bmatrix} = \mathbf{C}_P \begin{bmatrix} \Delta\delta \\ \Delta I_{od} \\ \Delta I_{oq} \end{bmatrix} \end{aligned} \quad (\text{A7})$$

where $\Delta\omega_{com}$ represents the deviation for angular frequency of the common reference frame, δ represents the angle difference between the common reference frame and the reference frame of an individual inverter, both of which rotate at the speed of ω_{com} . Note that I_{od} and I_{oq} are the low-pass-filtered values of i_{od} and i_{oq} , respectively, used for the proposed ACVR in the proposed I_{dq} controller, as shown in Fig. 4.2.

A.1.2 State-space model of voltage controller

The voltage controller, which is shown in Fig 2. 11, consists of feed-back and feed-forward loops. The reference voltage is controlled by standard PI controller. state variables for voltage controller is selected to the variable that can be easily differentiated, and the corresponding equations for state variables are as:

$$\phi_d = \int (v_{od}^* - v_d) dt \quad (A8)$$

$$\phi_q = \int (v_{oq}^* - v_q) dt \quad (A9)$$

$$\frac{d\phi_d}{dt} = v_{od}^* - v_{od} \quad (A10)$$

$$\frac{d\phi_q}{dt} = v_{oq}^* - v_{oq}, \quad (A11)$$

where ϕ_d and ϕ_q are the state variables for the voltage controller. (2.3) and (2.4) can be represented by the state variables as:

$$i_{ld}^* = K_{pv} \frac{d\phi_d}{dt} + K_{iv} \phi_d - \omega C_f^* v_{oq} + F^* i_{od} \quad (A12)$$

$$i_{lq}^* = K_{pv} \frac{d\phi_q}{dt} + K_{iv} \phi_q - \omega C_f^* v_{od} + F^* i_{oq} \quad (A13)$$

Based on (A12) and (A13), the small-signal state-space model of voltage controller is shown as:

$$\begin{bmatrix} \dot{\Delta\phi_{dq}} \end{bmatrix} = \begin{bmatrix} \mathbf{0} \end{bmatrix} \begin{bmatrix} \Delta\phi_{dq} \end{bmatrix} + \mathbf{B}_{v1} \begin{bmatrix} \Delta v_{odq}^* \end{bmatrix} + \mathbf{B}_{v2} \begin{bmatrix} \Delta i_{ldq} \\ \Delta v_{odq} \\ \Delta i_{odq} \end{bmatrix} \quad (A14)$$

$$\begin{bmatrix} \Delta i_{ldq}^* \end{bmatrix} = \mathbf{C}_v \begin{bmatrix} \Delta\phi_{dq} \end{bmatrix} + \mathbf{D}_{v1} \begin{bmatrix} \Delta v_{odq}^* \end{bmatrix} + \mathbf{D}_{v2} \begin{bmatrix} \Delta i_{ldq} \\ \Delta v_{odq} \\ \Delta i_{odq} \end{bmatrix} \quad (A15)$$

where the submatrices for the state-space equation \mathbf{B}_{V1} , \mathbf{B}_{V2} , \mathbf{C}_V , \mathbf{D}_{V1} , and \mathbf{D}_{V2} are expressed as:

$$\mathbf{B}_{V1} = \begin{bmatrix} 1 & 0 \\ 0 & 1 \end{bmatrix} \quad (\text{A16})$$

$$\mathbf{B}_{V2} = \begin{bmatrix} 0 & 0 & -1 & 0 & 0 & 0 \\ 0 & 0 & 0 & -1 & 0 & 0 \end{bmatrix} \quad (\text{A17})$$

$$\mathbf{C}_V = \begin{bmatrix} K_{iv} & 0 \\ 0 & K_{iv} \end{bmatrix} \quad (\text{A18})$$

$$\mathbf{D}_{V1} = \begin{bmatrix} K_{pv} & 0 \\ 0 & K_{pv} \end{bmatrix} \quad (\text{A19})$$

$$\mathbf{D}_{V2} = \begin{bmatrix} 0 & 0 & -K_{pv} & -\omega_n C_f & F & 0 \\ 0 & 0 & \omega_n C_f & -K_{pv} & 0 & F \end{bmatrix} \quad (\text{A20})$$

A.1.3 State-space model of current controller

The voltage controller, which is illustrated in Fig 2. 12, includes feed-back and feed-forward loops. The reference current is controlled by standard PI controller. state variables for current controller is set to the variable that can be easily differentiated in the same way to A.1.2, and the corresponding equations for state variables are as:

$$\gamma_d = \int (i_{ld}^* - i_{ld}) dt \quad (\text{A21})$$

$$\gamma_q = \int (i_{lq}^* - i_{lq}) dt \quad (\text{A22})$$

$$\frac{d\gamma_d}{dt} = i_{ld}^* - i_{ld} \quad (\text{A23})$$

$$\frac{d\gamma_q}{dt} = i_{lq}^* - i_{lq} \quad (\text{A24})$$

where γ_d and γ_q are the state values for the current controller. (2.5) and (2.6) can be expressed by the state variables as:

$$v_{od}^* = K_{pi} \frac{d\gamma_d}{dt} + K_{ii} \gamma_q - \omega L_f^* i_{oq} \quad (\text{A25})$$

$$v_{oq}^* = K_{pi} \frac{d\gamma_q}{dt} + K_{ii} \gamma_d - \omega L_f^* i_{od} \quad (\text{A26})$$

By using (A25) and (A26), the small-signal state-space model of current controller can be expressed as:

$$\begin{bmatrix} \dot{\Delta\gamma_{dq}} \end{bmatrix} = \begin{bmatrix} \mathbf{0} \end{bmatrix} \begin{bmatrix} \Delta\gamma_{dq} \end{bmatrix} + \mathbf{B}_{C1} \begin{bmatrix} \Delta i_{ldq}^* \end{bmatrix} + \mathbf{B}_{C2} \begin{bmatrix} \Delta v_{odq} \\ \Delta i_{odq} \end{bmatrix} \quad (\text{A27})$$

$$\begin{bmatrix} \Delta v_{idq}^* \end{bmatrix} = \mathbf{C}_C \begin{bmatrix} \Delta\gamma_{dq} \end{bmatrix} + \mathbf{D}_{C1} \begin{bmatrix} \Delta i_{ldq}^* \end{bmatrix} + \mathbf{D}_{C2} \begin{bmatrix} \Delta i_{ldq} \\ \Delta v_{odq} \\ \Delta i_{odq} \end{bmatrix} \quad (\text{A28})$$

where the submatrices for the small-signal state-space model of current controller \mathbf{B}_{C1} , \mathbf{B}_{C2} , \mathbf{C}_C , \mathbf{D}_{C1} , and \mathbf{D}_{C2} are expressed by PI gain and filter values as follows:

$$\mathbf{B}_{C1} = \begin{bmatrix} 1 & 0 \\ 0 & 1 \end{bmatrix} \quad (\text{A29})$$

$$\mathbf{B}_{C2} = \begin{bmatrix} -1 & 0 & 0 & 0 & 0 & 0 \\ 0 & -1 & 0 & 0 & 0 & 0 \end{bmatrix} \quad (\text{A30})$$

$$\mathbf{C}_C = \begin{bmatrix} K_{ic} & 0 \\ 0 & K_{ic} \end{bmatrix} \quad (\text{A31})$$

$$\mathbf{D}_{C1} = \begin{bmatrix} K_{pc} & 0 \\ 0 & K_{pc} \end{bmatrix} \quad (\text{A32})$$

$$\mathbf{D}_{C2} = \begin{bmatrix} -K_{pc} & -\omega_n L_f & 0 & 0 & 0 & 0 \\ \omega_n L_f & -K_{pc} & 0 & 0 & 0 & 0 \end{bmatrix} \quad (\text{A33})$$

A.1.4 State-space model of output LC filter and coupling inductance

The assumption about the state-space modelling of the output LC filter and coupling inductance is that the inverter voltage of IDER maintains their reference voltage (i.e., $v_i = v_i^*$) The output filter and grid coupling impedance can be derived by the following state equations as:

$$\frac{di_{ld}}{dt} = \frac{-r_f}{L_f} i_{ld} + \omega i_{lq} + \frac{1}{L_f} v_{id} - \frac{1}{L_f} v_{od}, \quad (\text{A34})$$

$$\frac{di_{lq}}{dt} = \frac{-r_f}{L_f} i_{lq} - \omega i_{ld} + \frac{1}{L_f} v_{iq} - \frac{1}{L_f} v_{oq}, \quad (\text{A35})$$

$$\frac{dv_{od}}{dt} = \omega v_{oq} + \frac{1}{C_f} i_{ld} - \frac{1}{C_f} i_{od}, \quad (\text{A36})$$

$$\frac{dv_{oq}}{dt} = -\omega v_{od} + \frac{1}{C_f} i_{lq} - \frac{1}{C_f} i_{oq}, \quad (\text{A37})$$

$$\frac{di_{od}}{dt} = \frac{-r_c}{L_c} i_{od} + \omega i_{oq} + \frac{1}{L_c} v_{od} - \frac{1}{L_c} v_{bd}, \quad (\text{A38})$$

$$\frac{di_{oq}}{dt} = \frac{-r_c}{L_c} i_{oq} + \omega i_{od} + \frac{1}{L_c} v_{oq} - \frac{1}{L_c} v_{bq}. \quad (\text{A39})$$

(A34) to (A39) is the linearized small-signal state-space equation of the filter and coupling inductance of individual IDER, which is shown in Fig. 2.10. the state-space model can be expressed as:

$$\begin{aligned} \begin{bmatrix} \dot{\Delta i}_{ldq} \\ \Delta v_{odq} \\ \Delta i_{odq} \end{bmatrix} &= \mathbf{A}_{\text{LCL}} \begin{bmatrix} \Delta i_{ldq} \\ \Delta v_{odq} \\ \Delta i_{odq} \end{bmatrix} + \mathbf{B}_{\text{LCL1}} \left[\Delta v_{idq} \right] \\ &\quad \mathbf{B}_{\text{LCL2}} \left[\Delta v_{bdq} \right] + \mathbf{B}_{\text{LCL3}} \left[\Delta \omega \right] \end{aligned} \quad (\text{A40})$$

where the submatrices for the small-signal state-space model of current controller \mathbf{A}_{LCL} , \mathbf{B}_{LCL1} , \mathbf{B}_{LCL2} , and \mathbf{B}_{LCL3} are expressed by the resistance, capacitance and inductance values as follows:

$$\mathbf{A}_{LCL} = \begin{bmatrix} \frac{-r_{L_f}}{L_f} & \omega_0 & -\frac{1}{L_f} & 0 & 0 & 0 \\ -\omega_0 & \frac{-r_{L_f}}{L_f} & 0 & -\frac{1}{L_f} & 0 & 0 \\ \frac{1}{C_f} & 0 & 0 & \omega_0 & -\frac{1}{C_f} & 0 \\ 0 & \frac{1}{C_f} & -\omega_0 & 0 & 0 & -\frac{1}{C_f} \\ 0 & 0 & \frac{1}{L_C} & 0 & \frac{-r_{L_c}}{L_C} & \omega_0 \\ 0 & 0 & 0 & \frac{1}{L_C} & -\omega_0 & \frac{-r_{L_c}}{L_C} \end{bmatrix} \quad (\text{A41})$$

$$\mathbf{B}_{LCL1} = \begin{bmatrix} \frac{1}{L_f} & 0 \\ 0 & \frac{1}{L_f} \\ 0 & 0 \\ 0 & 0 \\ 0 & 0 \\ 0 & 0 \end{bmatrix} \quad (\text{A42})$$

$$\mathbf{B}_{LCL2} = \begin{bmatrix} 0 & 0 \\ 0 & 0 \\ 0 & 0 \\ 0 & 0 \\ -\frac{1}{L_C} & 0 \\ 0 & -\frac{1}{L_C} \end{bmatrix} \quad (\text{A43})$$

$$\mathbf{B}_{LCL3} = \begin{bmatrix} I_{lq} & -I_{ld} & V_{oq} & -V_{od} & I_{oq} & -I_{od} \end{bmatrix}^T \quad (\text{A44})$$

A.1.5 State-space model of individual inverter model

In addition, (A6) and (A7) are integrated with the state-space models of the voltage and current controllers, the output RLC filter, and the coupling inductance to establish the state-space model of an individual IDER.

$$\left[\dot{\Delta x}_{INVi} \right] = \mathbf{A}_{INVi} \left[\Delta x_{INVi} \right] + \mathbf{B}_{INVi} \left[\Delta v_{bDQi} \right] + \mathbf{B}_{INV\omega i} \Delta \omega_{com}, \quad (\text{A45})$$

$$\begin{bmatrix} \Delta \omega_i \\ \Delta i_{oDQi} \end{bmatrix} = \begin{bmatrix} \mathbf{C}_{INV\omega i} \\ \mathbf{C}_{INVci} \end{bmatrix} \left[\Delta x_{INVi} \right], \quad (\text{A46})$$

where

$$\left[\Delta x_{INVi} \right] = \left[\Delta \delta_i \ \Delta I_{odi} \ \Delta I_{oqi} \ \Delta \varphi_{dqi} \ \Delta \gamma_{dqi} \ \Delta i_{ldqi} \ \Delta v_{odqi} \ \Delta i_{odqi} \right]^T. \quad (\text{A47})$$

The coefficient matrices \mathbf{A}_{INVi} , \mathbf{B}_{INVi} , $\mathbf{B}_{INV\omega i}$, $\mathbf{C}_{INV\omega i}$, and \mathbf{C}_{INVci} in (A45) and (A46) can be represented as:

$$\mathbf{A}_{INVi} = \begin{bmatrix} \mathbf{A}_{Pi} & \mathbf{0} & \mathbf{0} & \mathbf{B}_{Pi} \\ \mathbf{B}_{VHi} \mathbf{C}_{Pvi} & \mathbf{0} & \mathbf{0} & \mathbf{B}_{V2i} \\ \mathbf{B}_{VHi} \mathbf{D}_{VHi} \mathbf{C}_{Pvi} & \mathbf{B}_{CHi} \mathbf{C}_{Vi} & \mathbf{0} & \mathbf{B}_{CHi} \mathbf{D}_{V2i} + \mathbf{B}_{C2i} \\ \mathbf{B}_{LCLi} \mathbf{D}_{CHi} \mathbf{D}_{VHi} \mathbf{C}_{Pvi} & & & \mathbf{A}_{LCLi} + \\ + \mathbf{B}_{LCL2i} \begin{bmatrix} \mathbf{T}_{Vi}^{-1} & \mathbf{0} \end{bmatrix} & \mathbf{B}_{LCLi} \mathbf{D}_{CHi} \mathbf{C}_{Vi} & \mathbf{B}_{LCLi} \mathbf{C}_{Ci} & \mathbf{B}_{LCLi} \begin{pmatrix} \mathbf{D}_{CHi} \mathbf{D}_{V2i} \\ + \mathbf{D}_{C2i} \end{pmatrix} \\ + \mathbf{B}_{LCL3i} \mathbf{C}_{Poi} & & & \end{bmatrix}_{13 \times 13} \quad (\text{A48})$$

$$\mathbf{B}_{INVi} = \begin{bmatrix} \mathbf{0} \\ \mathbf{B}_{LCL2i} \mathbf{T}_{Si}^{-1} \end{bmatrix}_{13 \times 2} \quad (\text{A49})$$

$$\mathbf{B}_{INV\omega i} = \begin{bmatrix} \mathbf{B}_{P\omega} \\ \mathbf{0} \end{bmatrix}_{13 \times 1} \quad (\text{A50})$$

$$\mathbf{C}_{\text{INV}oi} = \begin{cases} [\mathbf{C}_{\text{P}oi} \ \vdots \ \mathbf{0}]_{1 \times 13} & i = 1 \\ [\mathbf{0}]_{1 \times 13} & i \neq 1 \end{cases} \quad (\text{A51})$$

$$\mathbf{C}_{\text{INV}ci} = [\mathbf{T}_{\text{Ci}} \ \vdots \ \mathbf{0} \ \vdots \ \mathbf{T}_{\text{Si}}]_{2 \times 13} \quad (\text{A52})$$

A.1.6 State-space model of combined inverter model

Let us consider the “ k ” number of IDERs is in the MG system. The transformation enables combining the small-signal state-space models of all the IDERs together, represent by submatrices \mathbf{A}_{INV} , \mathbf{B}_{INV} , and $\mathbf{C}_{\text{INV}c}$ as:

$$[\dot{\Delta x}_{\text{INV}}] = \mathbf{A}_{\text{INV}} [\Delta x_{\text{INV}}] + \mathbf{B}_{\text{INV}} [\Delta v_{bDQ}], \quad (\text{A53})$$

$$[\dot{\Delta i}_{oDQ}] = \mathbf{C}_{\text{INV}c} [\Delta x_{\text{INV}}], \quad (\text{A54})$$

$$\mathbf{A}_{\text{INV}} = \begin{bmatrix} \mathbf{A}_{\text{INV}1} + \mathbf{X}_{m_p} & \mathbf{0} & \mathbf{0} & \cdots & \mathbf{0} \\ \mathbf{X}_{m_p} & \mathbf{A}_{\text{INV}2} & \mathbf{0} & \cdots & \mathbf{0} \\ \mathbf{X}_{m_p} & \mathbf{0} & \ddots & \ddots & \vdots \\ \vdots & \vdots & \ddots & \ddots & \mathbf{0} \\ \mathbf{X}_{m_p} & \mathbf{0} & \cdots & \mathbf{0} & \mathbf{A}_{\text{INV}k} \end{bmatrix}_{13k \times 13k} \quad (\text{A55})$$

$$\mathbf{B}_{\text{INV}} = \text{diag}([\mathbf{B}_{\text{INV}1}, \mathbf{B}_{\text{INV}2}, \cdots, \mathbf{B}_{\text{INV}k}])_{13k \times 2m} \quad (\text{A56})$$

$$\mathbf{C}_{\text{INV}} = \text{diag}([\mathbf{C}_{\text{INV}c1}, \mathbf{C}_{\text{INV}c2}, \cdots, \mathbf{C}_{\text{INV}ck}])_{2k \times 13k} \quad (\text{A57})$$

where $\text{diag}()$ is used to show the elements of a diagonal term.

A. 2 State-space modeling of network and loads

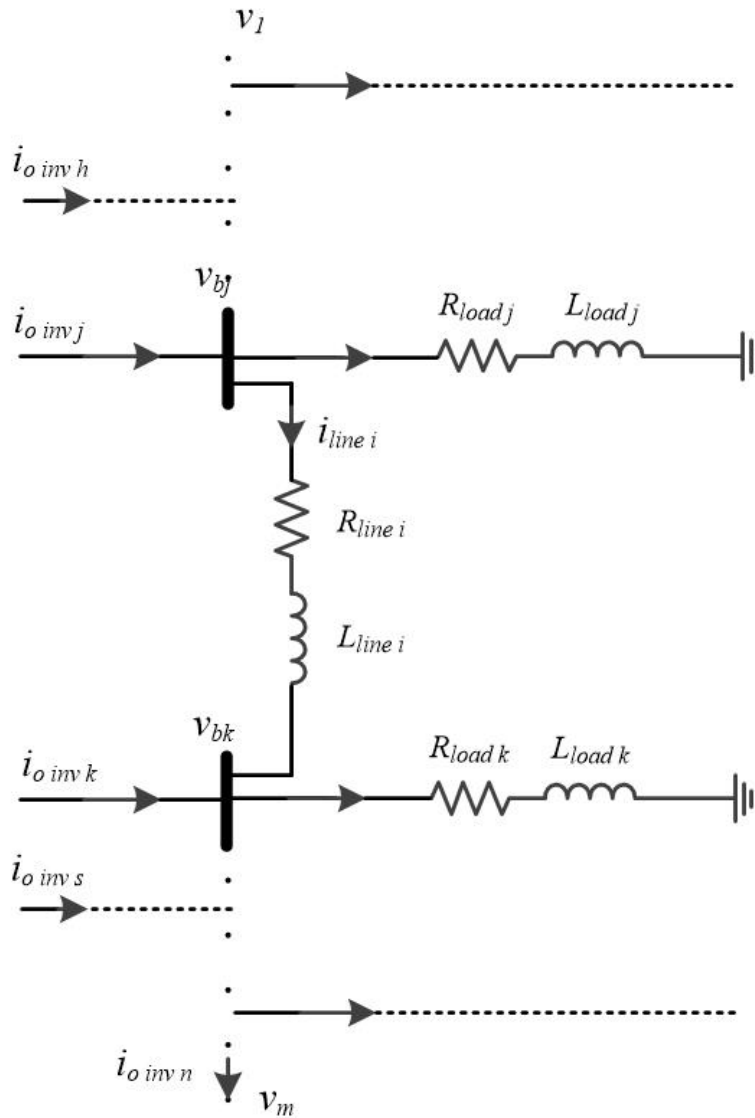


Fig. A.2. Network and load representation.

for small-signal state-space modelling of network and load, let us consider the “ k ” number of IDERs, “ n ” lines, and “ p ” load points at are at “ m ” nodes in the MG system, as shown in Fig. A.2.

A.2.1 State-space model of network

In DQ-reference frame, the state equations for line current flowing i -th line, which is connected between nodes j and k can be expressed as:

$$\frac{di_{lineDi}}{dt} = \frac{-r_{linei}}{L_{linei}} i_{lineDi} + \omega i_{lineQi} + \frac{1}{L_{linei}} v_{bDj} - \frac{1}{L_{linei}} v_{bDk}, \quad (A58)$$

$$\frac{di_{lineQi}}{dt} = \frac{-r_{linei}}{L_{linei}} i_{lineQi} - \omega i_{lineDi} + \frac{1}{L_{linei}} v_{bQj} - \frac{1}{L_{linei}} v_{bQk}, \quad (A59)$$

Using (A58) and (A59), the small-signal state-space model of network can be represented as:

$$\begin{bmatrix} \Delta i_{lineDQ} \end{bmatrix} = \mathbf{A}_{NET} \begin{bmatrix} \Delta i_{lineDQ} \end{bmatrix} + \mathbf{B}_{1NET} \begin{bmatrix} \Delta v_{bDQ} \end{bmatrix} + \mathbf{B}_{2NET} \Delta \omega_{com} \quad (A60)$$

Where the submatrices for representation of state-space model of network, \mathbf{A}_{NET} , \mathbf{B}_{1NET} , and \mathbf{B}_{2NET} are derived as:

$$\mathbf{A}_{NET} = \begin{bmatrix} \mathbf{A}_{NET1} & 0 & \dots & 0 \\ 0 & \mathbf{A}_{NET2} & \ddots & \vdots \\ \vdots & \ddots & \ddots & 0 \\ 0 & \dots & 0 & \mathbf{A}_{NETn} \end{bmatrix}_{2n \times 2n} \quad (A61)$$

Where \mathbf{A}_{NETi} is shown as:

$$\mathbf{A}_{NETi} = \begin{bmatrix} \frac{-r_{linei}}{L_{linei}} & \omega_0 \\ -\omega_0 & \frac{-r_{linei}}{L_{linei}} \end{bmatrix} \quad (A62)$$

$$\mathbf{B}_{1\text{NET}} = \begin{bmatrix} \mathbf{B}_{1\text{NET}1} \\ \mathbf{B}_{1\text{NET}2} \\ \vdots \\ \mathbf{B}_{1\text{NET}n} \end{bmatrix}_{2n \times 2m} \quad (\text{A63})$$

where $\mathbf{B}_{1\text{NET}i}$ is shown as:

$$\mathbf{B}_{1\text{NET}i} = \begin{bmatrix} \dots & \frac{1}{L_{\text{line}i}} & 0 & \dots & -\frac{1}{L_{\text{line}i}} & 0 & \dots \\ \dots & 0 & \frac{1}{L_{\text{line}i}} & \dots & 0 & -\frac{1}{L_{\text{line}i}} & \dots \end{bmatrix} \quad (\text{A64})$$

$$\mathbf{B}_{2\text{NET}i} = \begin{bmatrix} I_{\text{line}Qi} \\ -I_{\text{line}Di} \end{bmatrix} \quad (\text{A65})$$

where $\mathbf{B}_{2\text{NET}i}$ is shown as:

$$\mathbf{B}_{2\text{NET}} = \begin{bmatrix} \mathbf{B}_{2\text{NET}1} \\ \mathbf{B}_{2\text{NET}2} \\ \vdots \\ \mathbf{B}_{2\text{NET}n} \end{bmatrix}_{2n \times 1} \quad (\text{A66})$$

A.2.1 State-space model of loads

In this dissertation, General RL load is considered to derive a small-signal state-space model of loads. The state-space equation can be derived by the circuit analysis technique for i -th load as:

$$\frac{di_{\text{load}Di}}{dt} = \frac{-R_{\text{load}i}}{L_{\text{load}i}} i_{\text{load}Di} + \omega i_{\text{load}Qi} + \frac{1}{L_{\text{load}i}} v_{bDi}, \quad (\text{A67})$$

$$\frac{di_{loadQi}}{dt} = \frac{-R_{loadi}}{L_{loadi}} i_{loadQi} - \omega i_{loadDi} + \frac{1}{L_{loadi}} v_{bQi} \quad (A68)$$

$$\left[\dot{\Delta i_{loadDQ}} \right] = \mathbf{A}_{LOAD} \left[\Delta i_{loadDQ} \right] + \mathbf{B}_{1LOAD} \left[\Delta v_{bDQ} \right] + \mathbf{B}_{2LOAD} \Delta \omega_{com} \quad (A69)$$

$$\mathbf{A}_{LOAD} = \begin{bmatrix} \mathbf{A}_{LOAD1} & 0 & \cdots & 0 \\ 0 & \mathbf{A}_{LOAD2} & \ddots & \vdots \\ \vdots & \ddots & \ddots & 0 \\ 0 & \cdots & 0 & \mathbf{A}_{LOADp} \end{bmatrix}_{2p \times 2p} \quad (A70)$$

where \mathbf{A}_{LOADi} is shown as:

$$\mathbf{A}_{LOADi} = \begin{bmatrix} \frac{-R_{loadi}}{L_{loadi}} & \omega_0 \\ -\omega_0 & \frac{-R_{loadi}}{L_{loadi}} \end{bmatrix} \quad (A71)$$

$$\mathbf{B}_{1LOAD} = \begin{bmatrix} \mathbf{B}_{1LOAD1} \\ \mathbf{B}_{1LOAD2} \\ \vdots \\ \mathbf{B}_{1LOADp} \end{bmatrix}_{2p \times 2m} \quad (A72)$$

where \mathbf{B}_{1LOADi} is shown as:

$$\mathbf{B}_{1LOADi} = \begin{bmatrix} \cdots & \frac{1}{L_{loadi}} & 0 & \cdots & -\frac{1}{L_{loadi}} & 0 & \cdots \\ \cdots & 0 & \frac{1}{L_{loadi}} & \cdots & 0 & -\frac{1}{L_{loadi}} & \cdots \end{bmatrix}_{2 \times 2m} \quad (A73)$$

$$\mathbf{B}_{2\text{LOAD}} = \begin{bmatrix} \mathbf{B}_{2\text{LOAD}1} \\ \mathbf{B}_{2\text{LOAD}2} \\ \vdots \\ \mathbf{B}_{2\text{LOAD}p} \end{bmatrix}_{2p \times 1} \quad (\text{A74})$$

where $\mathbf{B}_{2\text{LOAD}i}$ is shown as:

$$\mathbf{B}_{2\text{LOAD}i} = \begin{bmatrix} I_{\text{load}Qi} \\ -I_{\text{load}Di} \end{bmatrix} \quad (\text{A75})$$

A. 3 Complete state-space model for Microgrid

In (A53)–(A54), (A66), and (A69), the DQ-axis bus voltages $[\Delta v_{bDQ}]$ are treated as the common inputs of the state-space models of the IDERs, lines, and loads. The bus voltages can be well defined by assuming a large virtual resistor r_N between each bus and ground, resulting in the expression for the DQ-axis currents of the IDERs, lines, and loads as:

$$\begin{bmatrix} \Delta v_{bDQ} \end{bmatrix} = \mathbf{R}_N \left(\mathbf{M}_{\text{INV}} \begin{bmatrix} \Delta i_{oDQ} \end{bmatrix} + \mathbf{M}_{\text{NET}} \begin{bmatrix} \Delta i_{\text{lineDQ}} \end{bmatrix} + \mathbf{M}_{\text{LOAD}} \begin{bmatrix} \Delta i_{\text{loadDQ}} \end{bmatrix} \right), \quad (\text{A76})$$

For inverter-based islanded microgrid, which has m nodes with k inverters, n network branches, and p loads, where \mathbf{R}_N is the $2m \times 2m$ diagonal matrix whose non-zero elements are equal to r_N .

\mathbf{M}_{INV} is $2m \times 2k$ matrix which maps the connection node of inverter onto network. (i.e. for i -th inverter node connected at j -th network node, the element of $M_{\text{INV}}(2*i-1, 2*j-1)$ and $M_{\text{INV}}(2*j, 2*i)$ is 1 and other elements in those rows are set to be 0.

\mathbf{M}_{NET} is $2m \times 2m$ sized matrix mapping the branches in the MG system onto the network nodes from i -th to the j -th node, which is determined by line current direction. For example, for branches having line current from i -th to the j -th node, the element of $M_{\text{NET}}(2*i-1, 2*i-1)$ and $M_{\text{NET}}(2*i, 2*i)$ are set to 1, while the element of $M_{\text{NET}}(2*j-1, 2*j-1)$ and $M_{\text{NET}}(2*j, 2*j)$ are set to -1, with other elements in those rows are 0.

\mathbf{M}_{LOAD} is $2m \times 2p$ matrix, which maps the points of p -th load connection onto the m -th network nodes of the inverter-based MG system, which refer to $M_{\text{LOAD}}(2*m-1, 2*p-1)$ and $M_{\text{LOAD}}(2*m, 2*p)$ elements, with -1. Using (A76), the state-space models (A53), (A54), (A66), and (A69) can be integrated into the complete state-space model of the MG as:

$$\begin{bmatrix} \dot{\Delta x}_{INV} \\ \Delta i_{lineDQ} \\ \Delta i_{loadDQ} \end{bmatrix} = \mathbf{A}_{MG} \begin{bmatrix} \Delta x_{INV} \\ \Delta i_{lineDQ} \\ \Delta i_{loadDQ} \end{bmatrix} \quad (\text{A77})$$

where \mathbf{A}_{MG} can be represented as:

$$\mathbf{A}_{MG} = \left[\mathbf{A}_{MG1} \mid \mathbf{A}_{MG2} \mid \mathbf{A}_{MG3} \right]_{(13k+2n+2p) \times (13k+2n+2p)} \quad (\text{A78})$$

where the submatrices \mathbf{A}_{MG1} , \mathbf{A}_{MG2} , and \mathbf{A}_{MG3} are:

$$\mathbf{A}_{MG1} = \begin{bmatrix} \mathbf{A}_{INV} + \mathbf{B}_{INV} \mathbf{R}_N \mathbf{M}_{INV} \mathbf{C}_{INV} \\ \hline \mathbf{B}_{INET} \mathbf{R}_N \mathbf{M}_{INV} \mathbf{C}_{INVc} + \mathbf{B}_{2NET} \mathbf{C}_{INV\omega} \\ \hline \mathbf{B}_{ILOAD} \mathbf{R}_N \mathbf{M}_{INV} \mathbf{C}_{INVc} + \mathbf{B}_{2LOAD} \mathbf{C}_{INV\omega} \end{bmatrix}_{(13k+2n+2p) \times 13k} \quad (\text{A79})$$

$$\mathbf{A}_{MG2} = \begin{bmatrix} \mathbf{B}_{INV} \mathbf{R}_N \mathbf{M}_{NET} \\ \hline \mathbf{A}_{NET} + \mathbf{B}_{INET} \mathbf{R}_N \mathbf{M}_{NET} \\ \hline \mathbf{B}_{ILOAD} \mathbf{R}_N \mathbf{M}_{NET} \end{bmatrix}_{(13k+2n+2p) \times 2n} \quad (\text{A80})$$

$$\mathbf{A}_{MG3} = \begin{bmatrix} \mathbf{B}_{INV} \mathbf{R}_N \mathbf{M}_{LOAD} \\ \hline \mathbf{B}_{INET} \mathbf{R}_N \mathbf{M}_{LOAD} \\ \hline \mathbf{A}_{LOAD} + \mathbf{B}_{ILOAD} \mathbf{R}_N \mathbf{M}_{LOAD} \end{bmatrix}_{(13k+2n+2p) \times 2p} \quad (\text{A81})$$

the system matrix \mathbf{A}_{MG} for inverter-based islanded microgrid, which has m nodes with k inverters, n network branches, and p loads, is used for the small-signal analysis.

A. 4 Verification of small-signal state-space model

In this dissertation, as in [71], the small-signal state-space model of MG system is developed following the procedure in [13]. The system parameters and initial conditions for small-signal analysis in Chapter 4.3 is also the same as in [13], [71], as discussed in Appendix A. 1. The small-signal state-space model in [13] has been verified with experimental testing [13]. The modeling approach in [13] is revised and improved in [71]:

- i) Consideration of inductance in RL loads (L_{LOAD1} and L_{LOAD2} are set to be 10 nH);
- ii) Small change of the values of line reactance (X_{LINE1} is changed from 0.1 to 0.995, X_{LINE2} is changed from 0.58 to 0.565);
- iii) Reversed q-axis elements, that is, q-axis element z_q in [13] is changed by $-z_q$ in [71];
- iv) Fixing some formula errors for the sub-matrices (for example, \mathbf{A}_{INV} , \mathbf{B}_{INV} , and \mathbf{C}_{INVc})

On the other hand, there seems to be an error in process for initial value assignment in [71]. It is presumed that V_{bq} ([-6 -6 -5] in [13] and [6 6 5] in [71]) was assigned incorrectly to V_{oq} ([0 0 0]).

Since the root loci for conventional droop control by [71] and the small-signal model used in this dissertation, which is represented by blue X, are the same as shown in Figs A.2 and A.3. the modeling can be considered to have been performed properly.

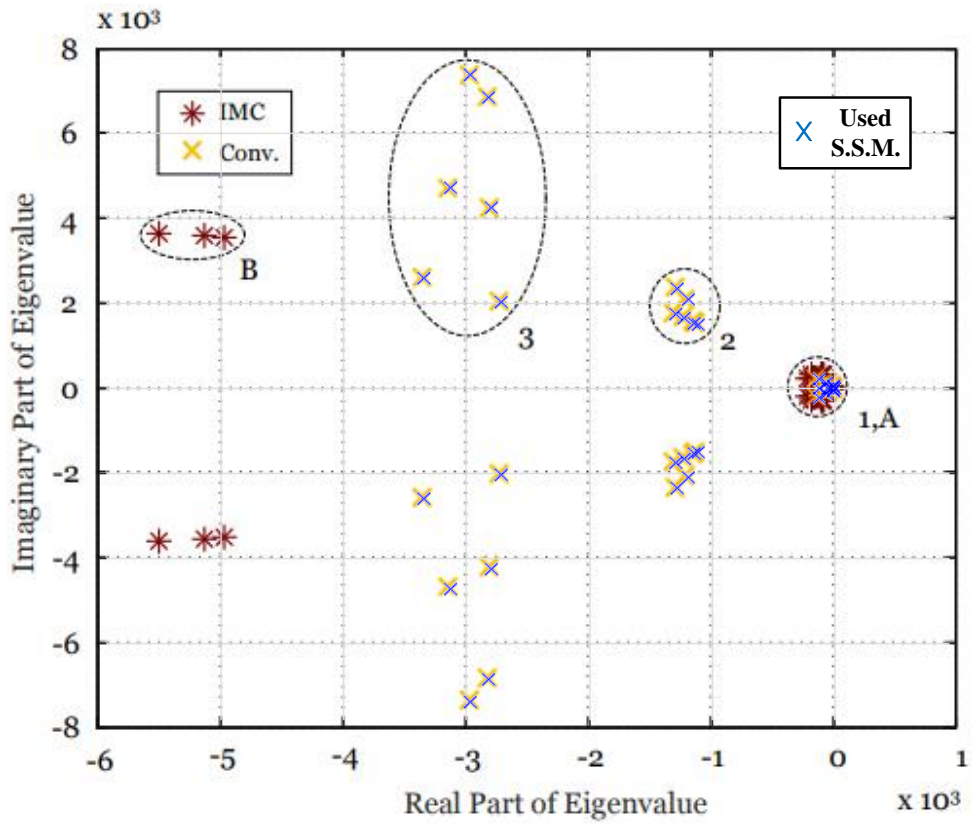


Fig. A.3. Comparison of root loci of the study MG in [71] and the used small-signal model for Chapter 4 [71].

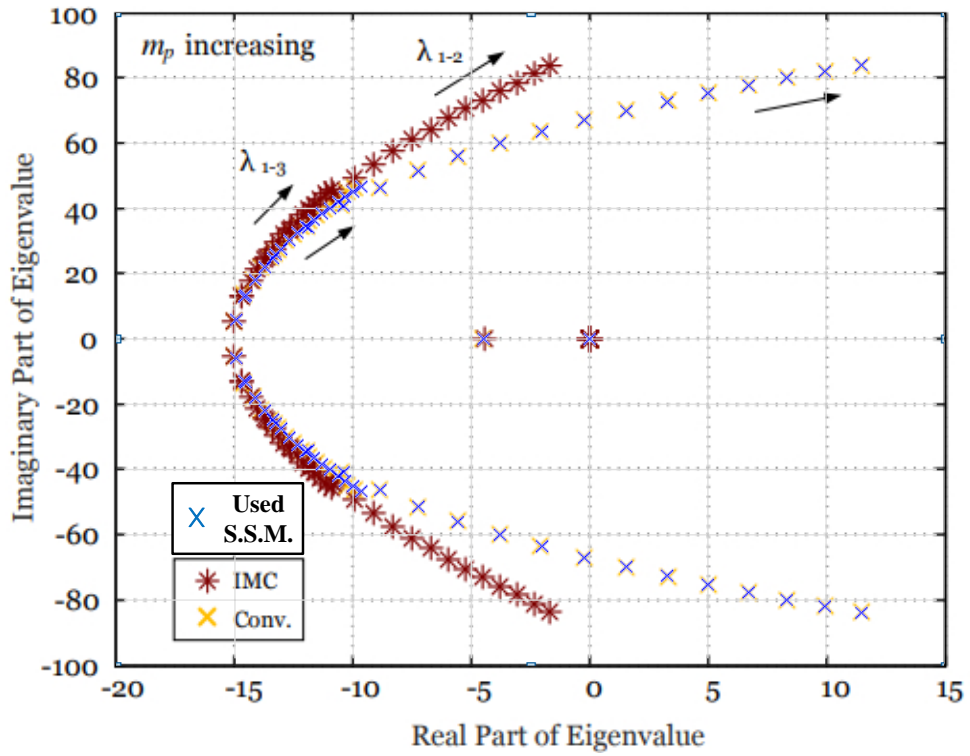


Fig. A.4. Comparison of root loci as a function of real power droop gain in [71] and the used small signal model for Chapter 4 [71].

초 록

내부 자원만으로 전력의 자급자족이 가능한 통합형 플랫폼 기술인 마이크로그리드(Microgrid, MG)는 분산에너지자원(Distributed Energy Resource, DER)을 활용하여 전력 수급과 전압/주파수 제어를 수행할 수 있다. 이외에도 다양한 제어 가능한 자원들을 활용하여 신재생에너지의 간헐적 특성 등으로 인한 시스템의 불확실성에 대응함으로써 계통의 신뢰도와 안정도를 향상시킬 수 있다. 특히 독립형 MG 기술은 기존 배전 계통 내 부하의 단독운전은 물론, 도서 지역, 외곽의 농촌 지역, 군사 지역 등 다양한 지역의 고립된 수용가와 더불어 전기 선박, 비행기 등 소규모 전력 시스템에 전력을 효과적으로 공급하기 위해 도입되고 있는 추세이다.

아울러, 에너지저장장치, 연료전지 등 출력 제어가 자유로운 다양한 인버터 연계형 분산에너지자원(Inverter-interfaced DER, IDER)들은 계통의 동적 변화에 빠르게 대응할 수 있어 긍정적 영향을 줄 수 있으므로 최근 상당한 관심을 받고 있다. 특히, IDER이 마스터 역할을 하여 전압과 주파수가 결정되도록 운영하는 인버터 기반 독립형 MG의 연구와 실증이 활발히 진행되고 있으며. 이는 단일-마스터 운영(Single Master Operation, SMO) 과 다중-마스터 운영(Multi-master Operation, MMO) 두 종류로 분류할 수 있다. 또한, MG의 운영을 위한 자율 제어 전략은 지역적 정보만을 기반으로 동작하여 통신으로 인해 발생할 수 있는 문제를 최소화함으로써 독립형 MG의 신뢰도 향상과 구축비용 절감에 도움이 될 수 있다.

본 논문에서는 인버터 기반 독립형 MG에서 SMO와 MMO 구조 각각에 대하여 부하의 전압 의존도를 고려한 자율적 전력 관리 전략을

제안한다. 비통신 기반의 자율적 방식으로 동작하기 위해 마스터 역할을 수행하는 IDER이 생성하는 주파수 신호를 활용하였다. 마스터 IDER에 의해 생성된 주파수는 계통 내 다른 DER 및 제어 가능한 설비에서 측정이 가능한 전역적인 신호로서 사용된다. 제안한 방법은 SMO와 MMO 구조 하에서 전력계통의 예비력을 추가적으로 확보하여 신뢰도를 향상시키기 위해 작동한다. 이를 위해 단순한 구조의 제어기를 도입하여 기존의 제어 방식과 쉽게 호환될 수 있는 자율적 전력 관리 전략을 각각 제시하였다.

SMO 구조에서는 주로 하나의 마스터 IDER이 정전압-정주파수 (Constant-Voltage Constant-Frequency, CVCF) 운전을 통해 전력계통의 전압, 주파수 생성은 물론 실시간 전력수급을 모두 담당하도록 제어되어 왔다. 이는 하나의 분산전원의 응답속도가 빠르고 용량이 전체 계통의 큰 부분을 차지할 때 적합할 수 있다. 그러나 발전기 탈락, 급격한 기상 변화 등 심각한 사고나 갑작스러운 부하 증가로 인해 전력 계통의 수요와 공급이 크게 차이가 날 경우 하나의 마스터 IDER만으로는 감당하기 어려운 상황이 될 수 있다. 이같은 문제를 해결하기 위해 본 논문에서는 전압-주파수 비례제어기 (Voltage-Frequency Proportional Controller, VFPC)를 제안하여 일반적인 상황에서는 CVCF 운전으로 계통의 주파수, 전압을 일정하게 유지하되, 전력 수급이 깨지는 상황을 마스터 IDER이 연계된 모선의 전압의 하락을 통해 감지하여 계통 주파수를 낮춘다. 그러면 계통 내 다른 발전기가 f - P 드롭 제어를 통해 전력 공급을 하도록 유도하여 순시 예비력을 추가적으로 확보하여 마스터 유닛의 운영 부담을 덜어줄 수 있다.

MMO 구조에서는 여러 대의 IDER과 제어가 가능한 다른 자원들을 협조 제어하기 위해 P - f , Q - V 드롭 제어 방법이 폭넓게 이용되어 왔다. 하지만 이러한 제어 방식은 P , Q 측정을 위한 시지연이 존재하여 인버터

기반 분산전원의 능력을 최대한으로 활용하지 못한다는 문제가 있다. 한편 부하로부터 가상의 예비력을 확보하기 위해 계통의 신뢰도 향상을 목적으로 기존의 전력 계통에서 오래전부터 쓰인 성숙된 기술인 Conservation voltage reduction (CVR)이 기존과는 다른 형태로 MG에 적용이 되고 있는 추세이다. 본 논문에서는 전력 분배를 위한 I_d-f , I_q-V 제어기와 주파수 기반의 자율적 CVR을 수행하기 위한 I_d-V 제어기를 포함하는 I_{dq} 제어기를 도입하여 전력 계통의 과도 응답을 향상시키면서 부하 증가의 감쇠를 유도하여 인버터 기반 독립형 MG의 신뢰성 있는 운영을 도모한다.

제안한 두 가지의 자율적 전력 관리 전략은 각각 다른 계통을 대상으로 한 MATLAB/SIMULINK 환경에서의 사례연구를 통해 그 효과가 검증되었다. 먼저 SMO 구조에서 제안한 전략의 경우, 한국전력으로부터 제공받은 실제 계통 정보를 바탕으로 한 거차도 MG 모델을 사용하였으며, MMO 구조에서는 3 대의 IDER이 연계된 3 모선 계통을 활용하였다. 먼저 3 모선 계통에서 제안한 제어기의 효과를 기존 제어기와 비교 검증하기 위해 소신호 분석을 수행하였다. 이를 위해 해당 계통의 상태 공간 모델을 수립하였으며, 제안한 제어기와 기존 제어기에서의 근-궤적 분석을 비교하여 분석함으로써 제안한 제어기가 시스템의 안정도, 동특성, 드롭 계수 변동에 대한 견고성이 향상됨을 확인하였다. 사례 연구에서는 동적 모의 실험을 통하여 부하가 계단식으로 증가할 때 제안한 제어기의 효과와 제어 성능이 어떻게 변화하는지를 알아보았으며, 부하의 전압 의존도와 역률에 따라 제안한 CVR 기법의 효과가 어떻게 달라지는 지에 대해서도 분석을 수행하였다.

주요어 : 독립형 마이크로그리드, 드롭 제어, 자율 제어, 분산전원, 소신호분석, 에너지저장시스템, 전력계통 신뢰도, 주파수 제어

학 번 : 2012-20766